UNIVERSITY OF OKLAHOMA

GRADUATE COLLEGE

PROPERTIES OF NOBLE METAL NANOPARTICLES: MOLECULAR DYNAMICS AND DENSITY FUNCTIONAL THEORY STUDIES

A DISSERTATION

SUBMITTED TO THE GRADUATE FACULTY

in partial fulfillment of the requirements for the

Degree of

DOCTOR OF PHILOSOPHY

By

BRIAN H. MORROW
Norman, Oklahoma
2010

PROPERTIES OF NOBLE METAL NANOPARTICLES: MOLECULAR DYNAMICS AND DENSITY FUNCTIONAL THEORY STUDIES

A DISSERTATION APPROVED FOR THE
SCHOOL OF CHEMICAL, BIOLOGICAL AND MATERIALS ENGINEERING

BY

Dr. Alberto Striolo, Chair

Dr. Friederike C. Jentoft

Dr. Dimitrios V. Papavassiliou

Dr. Daniel E. Resasco

Dr. Jana K. Shen

Acknowledgements

I have greatly enjoyed my time as a graduate student at the University of Oklahoma. I would like to thank my advisor, Dr. Alberto Striolo, for all of his guidance over the course of my studies. His advice and encouragement have been a tremendous help.

I am also grateful for my committee members: Dr. Friederike Jentoft, Dr. Dimitrios Papavassiliou, Dr. Daniel Resasco, and Dr. Jana Shen. I learned much in their classes, and they have offered helpful input for my dissertation. I am also grateful for Dr. Henry Neeman and the rest of the staff at the OU Supercomputing Center for Education and Research, for their work in teaching about high-performance computing, and for their tireless efforts to keep OSCER resources available and to offer support to users such as myself. I would also like to acknowledge computing time from the National Energy Research Scientific Computing Center (NERSC) at Lawrence Berkeley National Laboratory. Funding for my research was provided by the Carbon Nanotube Technology Center (CANTEC) at the University of Oklahoma, through the U.S. Department of Energy.

I would like to thank Rajesh Tummala, Dimitrios Argyris, and the rest of Dr. Striolo's students. I've enjoyed having them as coworkers and as friends.

Finally I would like to thank my family for all their love and support over the years. This would not have been possible without them.

Table of Contents

List of Tables

List of Figures

Abstract

Supported metal nanoparticles play an important role in heterogeneous catalysis. In recent years, carbon nanotubes, because of their unique properties, have drawn interest as supports. The structural and dynamic properties of the supported metal nanoparticles can have a large effect on their catalytic properties. Towards understanding how the geometry of the support affects the properties of the metal nanoparticles, we performed molecular dynamics simulations of platinum and platinum-gold nanoparticles on graphite and bundles of carbon nanotubes of various diameters. Our results indicate that diffusion of the nanoparticle center of mass is one order of magnitude slower for Pt nanoparticles supported by carbon nanotube bundles than for Pt nanoparticles supported by graphite. Density profiles, radial distribution functions, and coordination numbers were used to characterize the morphology of the Pt nanoparticles. We found that carbon nanotube-supported nanoparticles exhibit a more disordered structure than graphite-supported nanoparticles. Simulations of nanoparticles containing 130, 249, and 498 atoms were conducted to assess how nanoparticle size affects nanoparticle morphology and mobility. It was found that increasing the nanoparticle size decreased its diffusion coefficient and increased its melting temperature. The size of the nanoparticle appears to affect the nanoparticle structure less than the geometry of the support. The effect of the metal-carbon interaction strength on the structure of the supported nanoparticles was studied, and our results indicated that there are not dramatic differences in the nanoparticle structure when different interaction parameters are used. Bimetallic Pt-Au nanoparticles were simulated in an effort to determine how the support and nanoparticle composition affect the distribution of atoms within and on

the surface of the nanoparticles. We found that, regardless of the support, Au atoms tended to segregate to the exterior of the nanoparticles. However, different supports lead to different arrangements of surface atoms in the nanoparticle, which has an effect on the nanoparticles catalytic activity. We also performed density functional theory calculations for CO adsorption on 13-atom Pt-Au clusters. We found that changing the environment around the metal atom on which CO adsorbs changes the adsorption energy and C-O vibrational frequency. Electronic structure properties of the clusters, such as charges on relevant atoms and densities of states, were discussed to explain the observed results.

1. Introduction

Metals on supports are utilized as catalysts in many industrially important reactions, such as hydrogenation of organic compounds and the Fischer-Tropsch process.[1] One possible material for use as a catalyst support is carbon nanotubes. Carbon nanotubes (CNTs) have many properties which make them attractive as supports for heterogeneous catalysis. They have high surface areas[2] of 300-400 m^2/g,[3-4] with samples of up to 790 m^2/g reported.[5] Nanotubes can be synthesized to be metallic or semiconducting; the band gap in semiconducting CNTs inversely depends on the diameter.[6-7] Because of their one-dimensional structure, electron transport in metallic CNTs occurs ballistically (without scattering), meaning they can carry high currents with little to no heating.[8-9] Simulations have shown H_2 and CH_4 transport rates through CNTs are orders of magnitude faster than in zeolites with similar pore sizes.[10] Experimental data has shown that CNT-supported platinum nanoparticles have higher catalytic activity than Pt supported on other forms of carbon for many reactions, including oxygen reduction[11-17] and methanol oxidation.[13, 18-21] The use of CNT-supported Pt in proton exchange membrane fuel cells has also been investigated.[22-23] Supported Pt nanoparticles also retain their electrochemical surface area better on CNTs compared to carbon black.[24-25] Although CNT-supported platinum is a promising catalyst, both platinum and carbon nanotubes are expensive, so in order to reduce cost these catalysts must be as active and selective as possible in order to utilize less of these materials.

Many factors must be considered when designing efficient catalysts. The size and shape of the metal nanoparticles are important, as they influence such characteristics as the coordination numbers of metal surface atoms and the crystallographic planes on the nanoparticle surface, both of which affect the catalytic activity and selectivity. For example, for the aromatization of n-hexane, Pt(111) terraces are 3-7 times more active than Pt(100) terraces.[26] Bratlie et al.[27] showed that in benzene hydrogenation, both cyclohexane and cyclohexene were formed on cuboctahedral Pt nanoparticles, while only cyclohexane was formed on cubic Pt nanoparticles. The rate at which the nanoparticle moves on the support also plays a role, as higher mobility will lead to sintering, which increases particle size. However, properties such as the coordination number of surface atoms and the mobility of the nanoparticles on the support are difficult to measure experimentally, especially at the relatively high temperatures and pressures that are used in practical catalytic applications.

In order to further understanding of supported metal nanoparticles, and to aid in the design of efficient catalysts, molecular dynamics simulations can be utilized. Molecular dynamics (MD) is a simulation technique that involves integrating the classical equations of motion to follow the time evolution of atoms and molecules, and can be used to study metal nanoparticles in atomistic detail, and do so at conditions which are difficult to study experimentally. MD has previously been used to study nanoparticles supported by graphite. The diffusion of Au[28-31] and Pt[32-33] nanoparticles supported by graphite has been investigated, and among the predicted results are a high diffusion coefficient of the nanoparticle center of mass, on the order of 10^{-5} cm^2/s. It has been found that defects in graphite supports do not significantly affect the diffusion

coefficient, but the nanoparticles are attracted to ascending steps and repelled by descending steps and vacancies.[34-35] In Chapters 2 and 3 we utilize molecular dynamics simulations to study Pt nanoparticles of three different sizes on graphite, and compare the properties of graphite-supported Pt to carbon-nanotube supported Pt. We find that the support alters both structural and dynamic properties of the nanoparticles, which could help explain the experimentally observed high catalytic activity and stability of CNT-based catalysts. Molecular dynamics simulations are only as accurate as the potentials utilized. Therefore, in Chapter 4 we examine the effect of the Pt-C interaction used in our simulations on the structure of the supported nanoparticles.

One way to further increase the efficiency of catalysts is to utilize bimetallic nanoparticles, which have a high chemical versatility, as their catalytic activity and selectivity can be tuned by changing their composition and size.[36] For example, Pt-Au catalysts have been shown to have higher catalytic activity than Pt for reactions such as oxidation of methanol[37-39] and formic acid,[40-42] and reduction of oxygen.[43-44] Multiwalled CNT-supported Pt-Au shows good electrocatalytic activity for methanol oxidation.[45] In Chapter 5 we study Pt-Au nanoparticles using molecular dynamics, concentrating on how the support and the nanoparticle composition alter the distribution of atoms within the nanoparticles, and the arrangement of atoms on the nanoparticle surface.

While molecular dynamics simulations are extremely useful in elucidating the structure and dynamics of metal nanoparticles, they are limited in that they are classical simulations, and electronic effects are not considered. *Ab initio* density functional theory (DFT) is a relatively computationally inexpensive way to calculate the electronic

structures of materials. DFT can be used to obtain adsorption energies of molecules such as CO on metal surfaces, such as Pt(111),[46-49] and metal clusters and nanoparticles of various sizes, such as Pd_{55} and Pd_{146},[50] and Pt clusters with 2-4 atoms,[51] up to 7 atoms,[52] or up to 28 atoms.[53] CO is a useful probe molecule, as its adsorption energy and C-O stretching frequency depend on the adsorption site and can be determined experimentally via methods such as Fourier transform infrared spectroscopy. Adsorption of CO also plays an important role in reactions such as CO oxidation and the Fischer-Tropsch process. DFT calculations can be used to aid in the development of new catalysts. Linic *et al.*[54] used DFT to formulate a Cu/Ag alloy that has higher selectivity for ethylene epoxidation compared to the traditional Ag catalyst. Studt *et al.*,[55] by performing DFT calculations of hydrocarbon heats of adsorption, identified Ni-Zn alloys as an alternative to the Pd catalysts most commonly used for the selective hydrogenation of acetylene in industry. Both of these predictions were verified experimentally. In Chapter 6 we use DFT calculations to study CO adsorption on Pt-Au clusters containing 13 atoms. We investigate how the local environment of a metal atom changes the properties of CO adsorbed on that atom. These calculations will aid in the understanding of the properties of small metal clusters, and help link our previous MD simulations to experiment.

2. Morphology and Diffusion Mechanism of Platinum Nanoparticles on Carbon Nanotube Bundles

The material presented below was published in 2007 in volume 111, issue 48 of the Journal of Physical Chemistry C.

2.1. Abstract

Molecular dynamics simulations have been used to investigate the mobility and morphology of platinum nanoparticles supported on carbonaceous materials. The embedded-atom method was used to model Pt-Pt interactions. The Pt-C interactions were modeled using the Lennard-Jones potential. The positions of carbon atoms were fixed. The supports considered include a single graphite layer as well as carbon nanotubes, regarded as bundles. The goal of our work is to assess the effect of the substrate morphology on the properties of the metal nanoparticles. The properties of interest include the mobility and morphology of the supported nanoparticles. Our results show that the diffusion coefficients of Pt nanoparticles on carbon nanotube bundles are one order of magnitude lower than those of Pt nanoparticles supported by graphite. Density profiles, radial distribution functions, and average coordination numbers were calculated to study the structure of the supported nanoparticles. Pt nanoparticles deposited on carbon nanotubes differ structurally from those deposited on graphite. In particular, they are characterized by a lower average coordination number than those supported by graphite. These results indicate that the catalytic properties of supported Pt nanoparticles can be tuned by changing the substrate and may provide partial explanation of recent experimental studies according to which metal nanoparticles deposited on carbon nanotubes make effective catalysts.

2.2. Introduction

Supported metal nanoparticles are used in fields such as nanoelectronics, optoelectronics, and catalysis. Recently the use of metals supported on carbon nanotubes as electrocatalysts for fuel cells has been investigated, as the unique properties of carbon nanotubes (e.g. their high surface area and electrical conductivity,[7] high gas transport rate,[10] and tunable diameter) render them promising candidates for catalyst supports. The reported data indicate that platinum-carbon nanotube composites exhibit high catalytic activity for oxygen reduction and methanol oxidation,[12-13, 18] have very high electrochemically active surface areas,[13] and are more stable under operating conditions than platinum supported by carbon black.[24-25] However, because of the high cost of both carbon nanotubes and platinum, it is necessary to optimize these novel catalysts. To achieve such a goal it must be remembered that both the size and the morphology of the metal nanoparticles affect a given chemical reaction, as the rates of structure-sensitive reactions depend on factors such as the coordination numbers and crystallographic arrangement of the exposed metal atoms. The mobility of the metal nanoparticles on the support is a concern with respect to the lifetime of a catalyst, as over time small nanoparticles could migrate and agglomerate into larger ones, thus decreasing the catalytic activity. All of these factors are important to consider in order to develop economically viable catalysts. Unfortunately, however, the mobility and precise structure of supported metal nanoparticles can be difficult to measure experimentally, especially under operating conditions. Under such restraints, molecular dynamics simulations can be performed to understand the thermodynamic and transport properties of supported metal nanoparticles. Such calculations allow us not only to

examine space and time scales that would be inaccessible experimentally, but also to study supported metal clusters in atomistic detail.

Molecular dynamics simulations have been used previously to examine the properties of metal nanoparticles supported by graphite. Diffusion of gold[28-31] and platinum[32-33] nanoparticles on graphite has been investigated, and high diffusion coefficients, on the order of 10^{-5} cm^2/s, have been predicted. In order to consider systems of experimental relevance, metal nanoparticles have also been simulated on defective graphite surfaces, and the calculations predict diffusion coefficients similar to those obtained on perfect graphite.[34-35] As expected, it has been observed that the cluster size increases as loading (i.e., the amount of metal per unit surface area) increases,[56] and that the rate of diffusion depends on cluster size.[33] It has been found that supported platinum nanoparticles containing ~260 atoms melt at ~1000-1020 K,[57] a temperature much lower than that at which bulk platinum melts (2028 K).[58] It has also been predicted that supported and unsupported metal nanoparticles of similar sizes melt at different temperatures. [59]

The goal of the present manuscript is to investigate whether the morphology of the support (i.e., carbon nanotube bundles versus graphite) influences the properties (e.g., mobility and structure) of the supported metal nanoparticles. We hypothesize that when the surface roughness typical of a bundle of carbon nanotubes becomes comparable to the size of one supported metal nanoparticle, both the morphology and the mobility of the supported nanoparticle are significantly affected, and this may be responsible for the enhanced catalytic performance observed experimentally. To test our hypothesis, we employ canonical molecular dynamics simulations to examine the

morphology and mobility of platinum nanoparticles on large bundles of carbon nanotubes. By changing the diameter of the carbon nanotubes we can easily alter the roughness of the supporting bundle. The results are then compared to those found for the same nanoparticles on graphite.

2.3. Computational Details

Molecular dynamics simulations are performed using the Large-scale Atomic/Molecular Massively Parallel Simulator (LAMMPS).[60] The embedded-atom method (EAM)[61] is used to model Pt-Pt interactions. The total potential energy in the EAM model is given by

$$E = \sum_i F_i\left(\sum_{j\neq i} \rho_j\left(r_{ij}\right)\right) + \frac{1}{2}\sum_i \sum_{j\neq i} \phi_{ij}\left(r_{ij}\right) \quad (1)$$

where $F_i(\rho)$ is the energy required to embed atom *i* into the background electron density, ρ_j is the electron density due to atom *j*, and $\phi_{ij}(r_{ij})$ is the repulsion between the cores of atoms *i* and *j* separated by a distance r_{ij}. The functions $F_i(\rho)$ and $\phi_{ij}(r_{ij})$ are determined empirically by fitting to experimental data for sublimation energy, equilibrium lattice constant, elastic constants, and vacancy-formation energies of pure metals, and heats of solution of binary alloys. The validity of the functions was then assessed by computing properties such as migration energy of vacancies and surface energy and geometries of low-index surfaces.[61] The EAM has been used to calculate properties such as thermal expansion coefficients,[62] the melting point of Cu, Ag, Au, Ni,

Pd, and Pt,[63] and grain boundary structure,[64] with results that agree with experiment. The force field parameters used to model platinum are those developed by Foiles and Baskes[61] as included in the ptu3.eam potential file in the LAMMPS package. The cutoff distance for Pt-Pt interactions is set to 5.3 Å.

Following others[57] we employ a 12-6 Lennard-Jones potential[65] to describe metal-carbon interactions:

$$E\left(r_{ij}\right) = 4\varepsilon_{ij}\left[\left(\frac{\sigma_{ij}}{r_{ij}}\right)^{12} - \left(\frac{\sigma_{ij}}{r_{ij}}\right)^{6}\right] \qquad (2)$$

The parameter ε_{ij} has units of energy and indicates how strongly atoms *i* and *j* are attracted, while σ_{ij} has units of length and is related to the size of atoms *i* and *j*. The Lennard-Jones parameters used here are σ = 2.95 Å and ε = 0.02206 eV.[57] These are derived[66] by fitting the Lennard-Jones potential to simulation data for platinum obtained using a many-body potential (the Sutton-Chen potential[67]) to obtain Pt-Pt parameters, then using Lorentz-Berthelot mixing rules[65] to determine Pt-C parameters. The cutoff distance for the Pt-C interactions is set to 9.0 Å.

As a first approximation the carbon atoms in the substrate (either graphite or carbon nanotubes) are held fixed. Lewis et al.[31] simulated gold clusters on graphite with both static and dynamic substrates, and found that in both cases simulations yield qualitatively similar results. Given the uncertainty involved in the metal-carbon interaction, we do not consider it necessary at this time to improve upon the assumption of fixed carbon atoms. However, we point out that this approximation is expected to become less accurate as the diameter of the carbon nanotubes increases.

Simulations were performed in the canonical ensemble[65] (constant number of atoms, simulation box volume, and system temperature), using the velocity-Verlet algorithm[65] to integrate the equations of motion, with a timestep of 2.5 fs. Each simulation ran for 30 million time steps, for a total of 75 ns. The first 1 ns of simulation data were discarded, and the final configuration was used to initiate a subsequent simulation. The results reported here are sub-block averages obtained from at least 5 subsequent simulations. Such long simulations are necessary to ensure reliable results.

Several substrates were employed, and these are shown in Figure 1. Substrate (a) is a single graphite sheet containing 1560 atoms. The simulation box is 63.96 Å x 63.90 Å. Graphite does not naturally occur as a single layer of carbon atoms. To assess whether or not including layers deeper than the first affects the results presented here we conducted test simulations for one nanoparticle of 249 Pt atoms at 700 K modeling graphite as three layers of carbon atoms. The results for both diffusion coefficient and structural properties were not distinguishable from those reported in this manuscript. Thus, for economy of computing time all subsequent simulations were conducted by considering only one layer of carbon atoms, as shown in Figure 1. Substrate (b) consists of four (4,4) single-walled carbon nanotubes (CNTs), each containing 320 atoms. The spacing between atoms of adjacent CNTs is set to 3.4 Å, which is approximately the distance between basal planes of graphite. The axis of each nanotube is parallel to the y-axis, which is 49.188 Å long. The CNTs are arranged along the *x*-axis, which is 35.296 Å long. Substrate (c) consists of four (10,10) CNTs, arranged in a manner similar to substrate (b). The *x* and *y* dimensions are 67.840 Å and 49.188Å respectively. Substrate (d) consists of alternating (10,10) and (4,4) nanotubes, arranged similarly to substrates

(b) and (c). The *x* and *y* dimensions are 68.528 Å and 49.188 Å respectively. In all cases periodic boundary conditions are implemented only along the *x* and *y* directions. The z dimension of the simulation box (perpendicular to the substrate) equals 70 Å in all cases considered. Because no periodic boundary condition is considered in the z direction, the results obtained here should be considered as for supported clusters in vacuum. The (4,4) and (10,10) nanotubes have diameters of 0.5424 nm and 1.356 nm, respectively. One platinum nanoparticle of 249 atoms (Pt_{249}) is placed on these substrates. This nanoparticle has a diameter of 1.7-2.0 nm, similar to the size of Pt clusters experimentally deposited on carbon nanotubes.[68-69] From Figure 1b it can be seen that the diameter of Pt_{249} is only slightly smaller than the *x*-dimension of the simulation box when (4,4) CNTs are considered as support. To ensure that the results presented below are not dependent on the size of the simulation box we conducted additional simulations with eight (4,4) CNTs as substrate. The resultant simulation box measured 70.592 Å in the *x*-direction. The results obtained for Pt_{249} at 900 K were indistinguishable from those reported below. The simulation protocol is as follows. Spherical metal nanoparticles are carved out of a perfect FCC lattice. These nanoparticles are then annealed for 1 ns at 700 K in vacuum, then the annealed particles are placed on the substrates. To ensure that the simulation results do not depend on the initial configuration, the deposited nanoparticles are further annealed for 1 ns at 700 K. The final configuration is used as the initial configuration for all simulations at all temperatures. The temperatures of interest are within the 400 to 1100 K range. The system is equilibrated for an additional 1 ns, and after this equilibration period a

production run lasting 74 ns is performed. The final configuration of a run is used as the initial configuration for the next simulation at the same temperature.

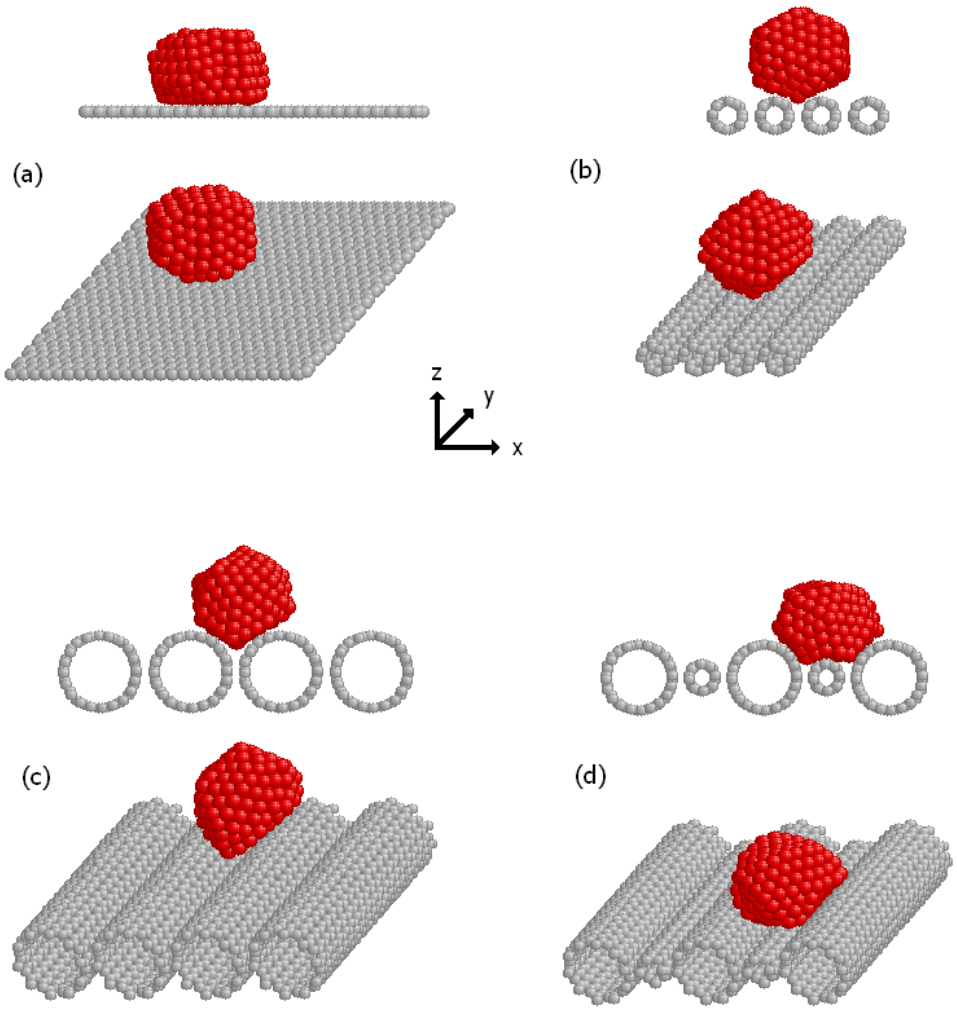

Figure 1: Snapshots of the 4 different substrates used in the simulations: (a) single graphite sheet, (b) four (4,4) nanotubes, (c) four (10,10) nanotubes, (d) alternating (10,10) and (4,4) nanotubes. In each case the Pt cluster, which contains 249 atoms, is shown in red, and the carbon atoms are shown in grey. Temperature is 500 K. For visualization purposes we provide two views, one along the *y*-axis (top in each panel), and the second from an angle (bottom in each panel).

The diffusion coefficient, *D*, of the cluster center of mass is determined from the mean-squared displacement *Δr(t)* by the equation[65]

$$\lim_{t\to\infty} \Delta r(t) = 2nDt \quad . \tag{3}$$

In Equation (3) *n* is the number of dimensions in which the cluster is undergoing diffusion, which in our case is 2 for clusters on graphite and 1 for clusters on CNTs (see below). Results reported for *D* are the average of 5 simulations, each using the final configuration of one run as the initial configuration for the next simulation. The error in these calculations is taken to be one standard deviation.

An autocorrelation function was used to examine the behavior of the Pt atoms in contact with the substrate. The term $Pt_i(t)$ describes whether or not platinum atom *i* is in contact with any carbon atom. $Pt_i(t)=1$ when platinum atom *i* is in contact with the substrate at time *t*, and $Pt_i(t)=0$ when the atom is not in contact with the substrate. A Pt atom is considered to be in contact with the substrate when the distance between it and any carbon atom is less than twice the distance parameter in the Pt-C Lennard-Jones interaction. The autocorrelation function C(t) is then calculated as

$$C(t) = \left\langle \frac{\sum_{i=1}^{N} Pt_i(t)\,Pt_i(0)}{\sum_{i=1}^{N} Pt_i(0)} \right\rangle \tag{4}$$

where the angular brackets indicate an ensemble average. The autocorrelation function yields a constant value when the same atoms remain in contact with the substrate, and decreases as these atoms change position in the cluster and are no longer in contact with any carbon atoms. Thus by calculating C(t) we can determine if a nanoparticle glides over the substrate or if some other diffusion mechanism, such as rotation, takes place.[70]

2.4. Results and Discussion

2.4.1. Diffusion

In Figure 2 we show plots of the center of mass coordinates of Pt_{249} at 500 K on substrates graphite (top left), (4,4) CNTs (top right), (10,10) CNTs (bottom left), and alternating CNTs (bottom right). For CNT substrates, the center axes of the CNTs are shown as red lines. Solid lines represent the axes of (10,10) CNTs, and dotted lines represent the axes of (4,4) CNTs. The data shown are collected during 18.75 ns of simulation time, and the center of mass coordinates were recorded once every 125 ps. The data indicate that the nanoparticle can move freely in two dimensions on the *xy* plane on graphite, as expected. In contrast, when the nanoparticle is placed on nanotubes it is constrained to diffuse only in the *y*-direction, parallel to the axes of the tubes. This one-dimensional diffusion is similar to the behavior of nanoparticles near an ascending graphite step, where the particles diffuse parallel to the step.[34-35] We observe that the particle settles in the trenches between the nanotubes, as shown by the center of mass coordinates (see also Figure 1 for a visualization). In the case of substrates composed of nanotubes of the same diameter, the trench is located between two neighboring carbon nanotubes. When the substrate is composed of alternating (4,4) and

(10,10) CNTs, the trench is located between two of the larger (10,10) nanotubes, and the center of mass of the nanoparticle is on top of the axis of a smaller (4,4) nanotube (see Figure 2d). Movement from one trench to another was not observed in our simulations when the nanoparticles were supported by (10,10) CNTs or alternating CNTs at any temperature. At temperatures above 600 K, nanoparticles deposited on (4,4) nanotubes appear to be able to hop between trenches. In our simulations these hops were observed 1-2 times over a span of 375 ns at temperatures of 700 K. We expect that hopping will become more frequent as the temperature increases, but current computational limitations prevent us from performing the extremely long simulations required to characterize statistically this diffusion mechanism.

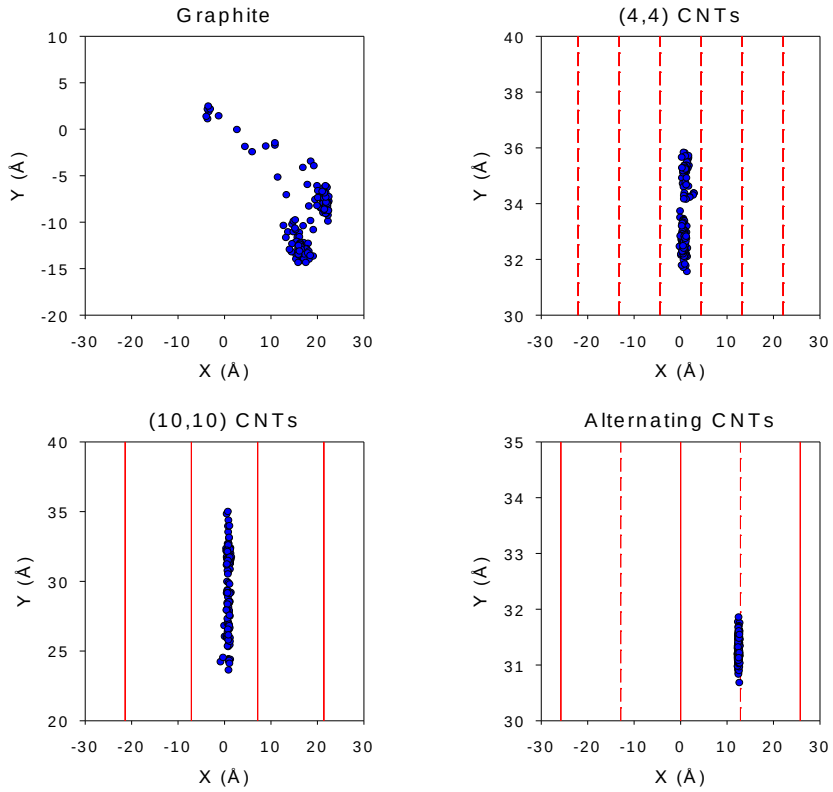

Figure 2: Center of mass coordinates for Pt_{249} at 500 K, on graphite (top left), (4,4) CNTs (top right), (10,10) CNTs (bottom left), and alternating CNTs (bottom right). Red lines represent the center axes of the carbon nanotubes. Solid lines are for (10,10) CNTs, broken lines are for (4,4) CNTs. Note that the y axes have different scales reflecting the mobility of the nanoparticles.

The results presented in Figure 2 suggest that metal nanoparticles deposited on carbon nanotube bundles are able to diffuse primarily along the nanotube axis. This in itself is an interesting result because it implies that the metal nanoparticles deposited on a bundle will not be able to easily coalesce unless they are deposited on the same trench or in trenches that are very close to each other. To quantify the mobility of the metal nanoparticles on the various supports we computed the diffusion coefficient of the nanoparticle center of mass as a function of temperature.

A plot of ln(D) vs 1000/T and D vs T for Pt_{249} on substrates (a), (b), (c), and (d) is given in Figure 3. For platinum on graphite we find a diffusion coefficient of 2.84×10^{-5} cm^2/s at 500 K, which is comparable to previously reported values for similar systems.[32, 34] Interestingly, our results indicate that the substrate has a large effect on the diffusion coefficient. The diffusion coefficients for platinum on CNTs are significantly lower than those for platinum on graphite. At most temperatures the diffusion coefficients on graphite are larger than those on CNTs by one order of magnitude. This result in our opinion is of significant practical relevance. Because of their lower diffusion coefficients, platinum clusters on nanotube bundles would experience less sintering, thus increasing the long-term durability of the electrocatalyst.[24] Further, the type of CNT-based support also affects the diffusion coefficient, as can be seen from Figure 3c. From 800 to 1100 K, the diffusion coefficients are lowest for the metal clusters supported by alternating CNTs, and highest for metal clusters supported by (10,10) CNTs. The fact that the diffusion coefficients computed for the alternating CNTs support are the lowest of all the substrates considered is important because most carbon nanotube bundles are composed of carbon nanotubes of different diameter.[71] Thus, our results suggest that the polydispersity in carbon nanotube diameter can be exploited to achieve practical advantages, since it seems to decrease the surface mobility of supported metal nanoparticles.

At temperatures below 900 K a plot of ln(D) vs 1000/T is nearly linear, and activation energies can be extracted from the Arrhenius formalism.[72] These are reported in Table 1. The results show that nanoparticles on graphite have the lowest activation energy for diffusion, and that nanoparticles on (10,10) CNTs have the highest activation

energy. These differences in activation energy appear to be due to the morphology of the substrate. The perfectly flat graphite surface results in the lowest activation energy, while the deep, narrow trenches formed between the (10,10) CNTs increase the activation energy by almost a factor of two. The wider trenches present in the alternating CNTs support yield a lower activation energy compared to the nanoparticles on pure (10,10) CNTs but larger than that on graphite. The nanoparticles on the support with the least amount of roughness, the (4,4) CNTs, have activation energy only slightly larger than that on graphite. These results suggest that the ratio between the diameters of the metal nanoparticle and the trench size may influence the activation energy for the diffusion.

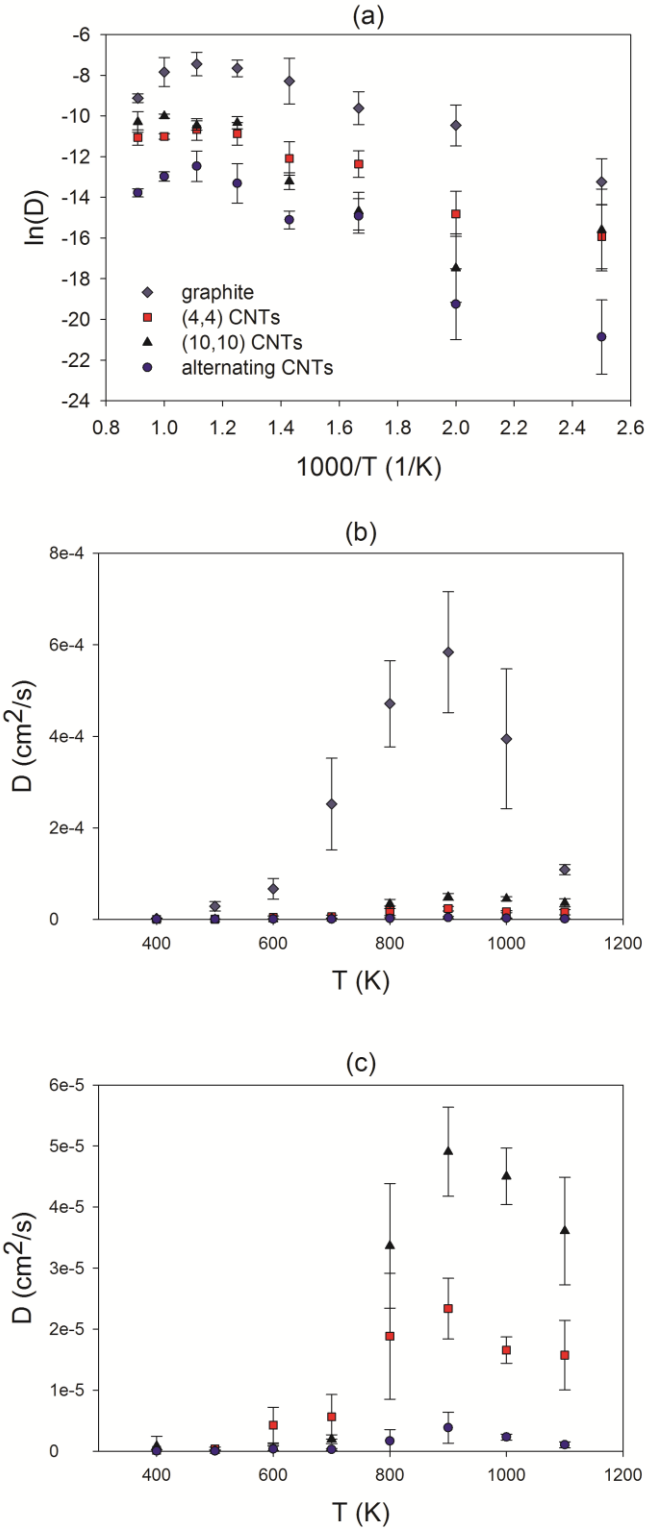

Figure 3: (a) ln(D) vs 1000/T and (b) D vs T for Pt_{249} on graphite (diamonds), four (4,4) CNTs (squares), four (10,10) CNTs (triangles), and alternating CNTs (circles). In panel (c) we report an enlargement plot of D vs T for Pt_{249} supported on the three CNT-based substrates.

Table 1: Activation energy for the diffusion of Pt_{249}

Substrate	Activation energy (kJ/mol)
graphite	36.9
(4,4) CNTs	37.6
(10,10) CNTs	71.9
Alternating CNTs	46.7

We note that the results reported in Table 1 were obtained for temperatures below 900 K. In fact, we observe that on all substrates, the diffusion coefficient increases as the temperature rises, reaches a maximum, and then decreases. This is likely due to the melting of the nanoparticles. To assess our hypothesis (e.g., that melting of the metal nanoparticles causes a decrease in the diffusion coefficient at temperature above 900 K), we seek to determine the melting temperature of the supported nanoparticles. In Figure 4 we report the potential energy as a function of temperature for Pt_{249} on graphite, (4,4) CNTs, (10,10) CNTs, and alternating CNTs. The melting temperature is determined from this plot by observing a change in the slope of the potential energy as a function of temperature. The nanoparticles supported by (4,4) CNTs appear to melt at ~950 K, while the nanoparticles on the other three substrates appear to melt at ~1000. This result agrees with molecular dynamics simulations reported by Huang and Balbuena,[57] which indicate a melting point of 1000-1020 K for a 256-atom cube-shaped Pt cluster and 260-atom ball-shaped Pt cluster on graphite. The slightly lower melting temperature observed in our work could be due to the smaller nanoparticle size, and differences in the potentials used to model Pt-Pt interactions. Other techniques can be used to determine the melting temperature of a metal nanoparticle. For example, we have calculated the radial distribution function g(r) for

those metal atoms that are within 5 Å of the nanoparticle's center of mass. For small, finite systems such as the metal nanoparticles considered here, g(r) can only provide short-range detail, but it can be used qualitatively to determine whether a cluster is solid or liquid. In Figure 5 we report g(r) at temperatures of 800 and 1100 K for platinum nanoparticles supported on all four substrates. At 800 K, g(r) exhibits a large, sharp peak at small separation, and several smaller peaks at intermediate separations, indicating a solid structure. At 1100 K, the peak at small separation decreases, and the weak intermediate peaks disappear. Only three broad peaks are still detected. This liquid-like radial distribution function indicates that the nanoparticle has melted. Thus, our results for g(r) corroborate those obtained from the potential energy as a function of temperature, that the supported nanoparticles melt at 900-1000 K. From the results shown in Figure 3, the maximum of the diffusion coefficient occurs at ~900 K. Since these temperatures roughly correspond to the melting points found for the cluster by examining the potential energy vs temperature and the radial distribution function, this confirms our hypothesis that at temperatures above approximately 900 K, the diffusion coefficient decreases due to the melting of the nanoparticle.

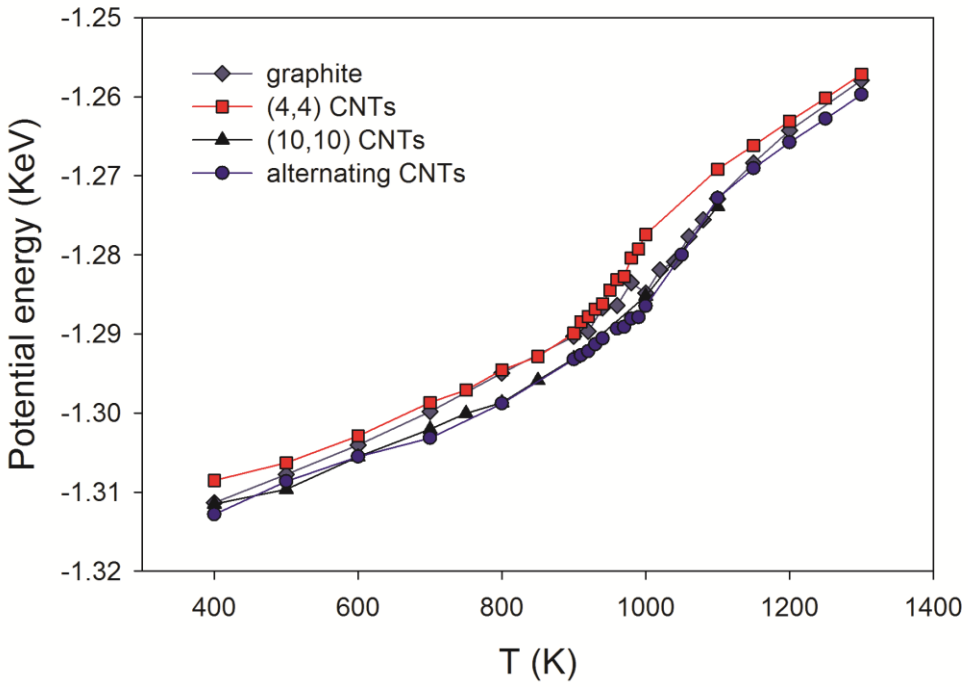

Figure 4: Potential energy vs temperature for Pt_{249} on graphite, (4,4) CNTs, (10,10) CNTs, and alternating CNTs.

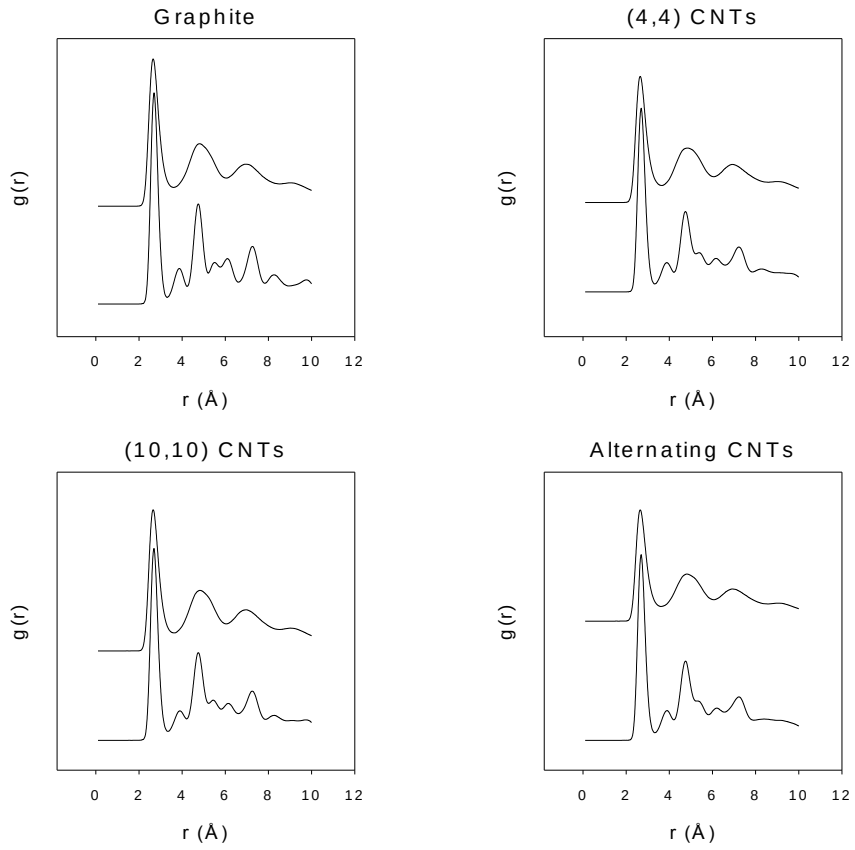

Figure 5: Radial distribution functions g(r) for Pt_{249} on (a) graphite, (b) (4,4) CNTs, (c) (10,10) CNTs, and (d) alternating CNTs, at 800 K (bottom) and 1100 K (top).

2.4.2. Diffusion Mechanism

The results shown so far indicate that the morphology of the substrate has a significant effect on the diffusion of supported metal nanoparticles of 249 Pt atoms. It should be pointed out that the size of such clusters is comparable to the diameter of the carbon nanotubes considered in our simulations. Our results cannot at present be extrapolated to systems in which the size of the nanoparticle is much smaller, or much larger, than the diameter of the carbon nanotubes. We now attempt to characterize the diffusion mechanism for the supported metal nanoparticles. In particular, we would like to determine whether the supported nanoparticles glide, rotate, or move following some

other diffusion mechanism. This information is important because the mechanism of diffusion could affect the sintering and final structure, and thus the catalytic properties, of supported metal nanoparticles.

An autocorrelation function, see section 2.3, was used to examine the behavior of the platinum atoms in contact with the substrate. An autocorrelation function constant with time indicates that as the nanoparticle diffuses the same Pt atoms remain in contact with the substrate; as these Pt atoms move away from the carbon substrate, the autocorrelation function decreases. A slowly decreasing C(t) would suggest a gliding type of motion, while a more rapidly decreasing C(t) could indicate rotation or a similar type of diffusion mechanism. The autocorrelation functions were calculated from a single simulation, using 10 time origins spaced 5 ns apart. Results were reproducible for different simulations. Our results for Pt_{249} on the four substrates are given in Figure 6.

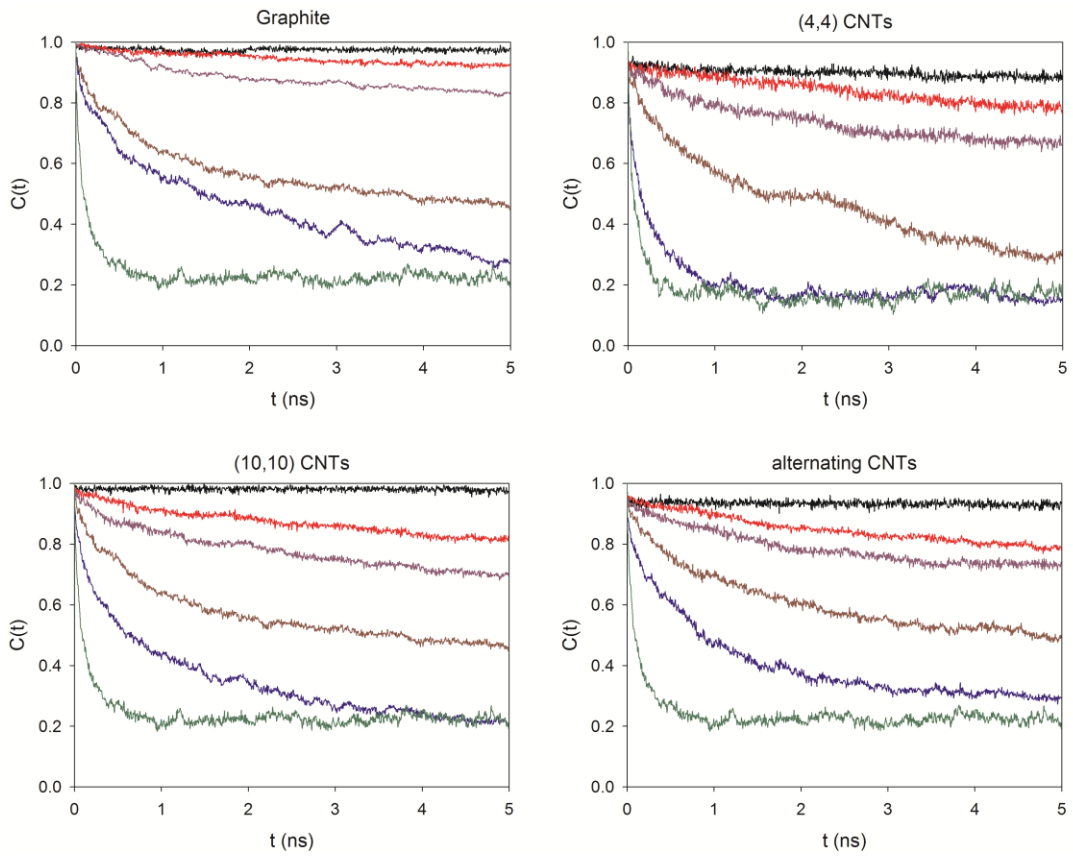

Figure 6: Autocorrelation functions for Pt_{249} on graphite (top left), (4,4) CNTs (top right), (10,10) CNTs (bottom left), and alternating CNTs (bottom right). In each panel temperatures, from top to bottom, are 600, 700, 800, 900, 1000, and 1100 K.

The behavior of C(t) for the platinum nanoparticle on graphite, (10,10) CNTs, and alternating CNTs is similar. For the nanoparticles supported by (4,4) CNTs, the behavior of C(t) at 1000 K differs from that observed on the other substrates. At this temperature for the nanoparticle supported by (4,4) CNTs, C(t) exhibits a rapid decrease, reaching a value of 0.2 in ~1 ns. In contrast, C(t) at 1000 K for (10,10) CNTs supported nanoparticles takes ~4.5 ns to reach a value of 0.2, and C(t) at 1000 K for nanoparticles supported by the other two substrates doesn't reach a value of 0.2 in the 5 ns considered. This is likely due to the fact that the nanoparticles on (4,4) CNTs have a lower melting temperature than they do on the other substrates. Based on the results

shown in Figure 4, we expect that the nanoparticles supported by (4,4) CNTs melt at ~950 K, while the melting temperature of the nanoparticles on the other substrates was ~1000 K. It is possible that at 1000 K the nanoparticles supported by graphite, (10,10) CNTs, and alternating CNTs are not completely melted, and thus C(t) behaves differently. This hypothesis is supported by the behavior of C(t) at 1100 K, above the predicted melting temperature of all the nanoparticles. At 1100 K, C(t) for the Pt nanoparticles supported on all four substrates decreases rapidly, matching the behavior at 1000 K for the nanoparticles supported on (4,4) CNTs.

The autocorrelation function indicates that at low temperatures, those platinum atoms that are in contact with the substrate at the beginning of the simulation remain that way for long periods of time, suggesting a gliding motion. At higher temperatures, however, platinum atoms in contact with the substrate move away from it as the simulation proceeds, and other atoms come into contact with the substrate, as indicated by the decrease in the autocorrelation function. At first sight this result may seem to indicate that the diffusion mechanism is gliding at low temperatures, and becomes rotational at higher temperatures. Visual inspection of sequences of simulation snapshots does not support such interpretation. To better understand the diffusion mechanism at high temperatures, we highlighted the metal atoms in contact with carbon atoms at the beginning of a simulation (red atoms in Figure 7), and examined their position after 7.5 ns of simulation time. This is visualized in Figure 7 where we represent the initial (Figure 7a) configuration and final (Figure 7b and Figure 7c) configurations after 7.5 ns of simulations at 2 different temperatures. At 600 K (Figure 7b), the metal atoms initially in contact with the substrate remain that way as expected

from results for the autocorrelation function. At 1000 K (Figure 7c), the Pt atoms initially in contact with the substrate are scattered throughout the nanoparticle. If diffusion was occurring via a rotational mechanism, we would expect that the initial contact atoms would remain grouped together. Thus, these results suggest that neither gliding nor rotation are occurring at high temperatures. Our results indicate that when the nanoparticle melts a disordered motion occurs, although the metal atoms remain aggregated at the temperatures considered here. Comparing the final snapshot obtained after 7.5 ns of simulation at 1000 K (Figure 7c) we note that the red Pt atoms are somewhat more dispersed when the substrate is composed of (4,4) CNTs than when it is composed of alternating CNTs. This is in agreement with the fact that C(t) at 1000 K decays more rapidly for nanoparticles supported by (4,4) CNTs that for nanoparticles supported by alternating CNTs (see Figure 6).

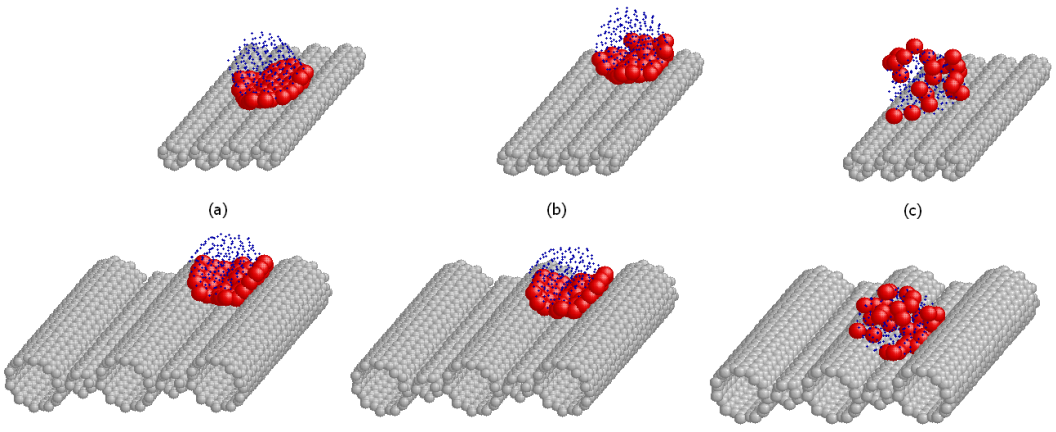

Figure 7: Pt_{249} on (4,4) CNTs (top) and alternating CNTs (bottom). a) Initial configuration, b) after 7.5 ns at 600 K, c) after 7.5 ns at 1000 K. Platinum atoms initially in contact with a carbon atom are colored red, all other platinum atoms are shrunk and colored blue.

2.4.3. Morphology

The structure of metal nanoparticles has a large effect on their chemical reactivity. As discussed in Chapter 1, there are structure-sensitive reactions whose kinetics are strong functions of crystallographic plane, coordination number of exposed atoms, etc. We have investigated the structure of the supported metal nanoparticles in order to determine if the type of substrate affects the morphology of the supported nanoparticles. Simulation snapshots at 500 K are shown in Figure 1, and suggest that the type of substrate affects the morphology of the supported metal nanoparticle. The results discussed above have shown that the metal nanoparticles below 900 K are solid. For comparison purposes, we report in Figure 8 simulation snapshots at 1100 K, at which temperature the nanoparticles are melted. A visual inspection reveals obvious differences in structures of the nanoparticles on carbon nanotubes compared to that of the nanoparticle on graphite, differences that we quantify below.

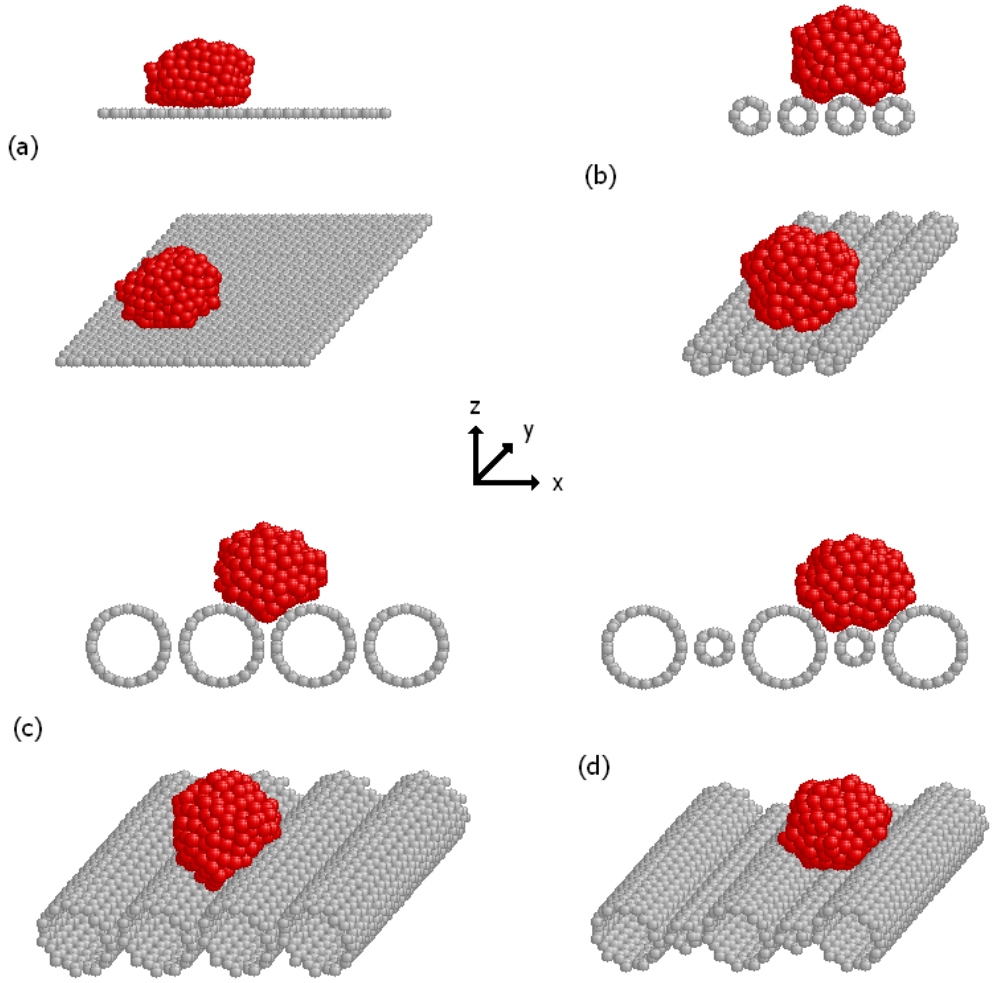

Figure 8: Same as Figure 1, but the simulation snapshots are obtained at 1100 K.

We first calculate the density of Pt atoms along the *z*-axis (perpendicular to the support). The z-density profiles for Pt_{249} are given in Figure 9 at various temperatures. At low temperatures, the profile for Pt on graphite exhibits sharp, regular peaks, indicating an ordered structure, which is similar to the face-centered cubic structure of bulk platinum. The profiles for Pt on nanotubes have a larger number of smaller, less-defined peaks, indicating a higher degree of disorder, and a different structure compared to the graphite-supported nanoparticles. The curved shape of the nanotube support

likely causes this effect, as the substrate distorts the face-centered cubic structure of the platinum. Note the changes in the density profiles at temperatures below the melting point of the nanoparticles, such as for the nanoparticles deposited on (4,4) CNTs at 600 K and 800 K, and on the nanoparticles deposited on (10,10) CNTs at 800 K. These changes occur as the temperature increases, giving the Pt atoms sufficient energy to rearrange themselves into a more energetically favorable position. Such rearrangements have been observed in previous molecular dynamics studies of Pt nanoparticles,[57] and are attributed to an increase in self-diffusion of Pt atoms within the nanoparticle, and to surface melting. In our case, the geometry of the substrate clearly affects the morphology of the supported metal nanoparticles, as can be seen visually in Figure 1 and Figure 8. To better appreciate the effect of substrate on the morphology of the 249 Pt atom nanoparticle, we report in Figure 10 the density profiles away from the surface obtained at 700 K. These results indicate that while the cluster structure on graphite is characterized by regular peaks, those on the (4,4) and on the (10,10) CNTs show several small peaks that apparently do not suggest any specific order for the metal atoms within the cluster. The density profile obtained on the alternating CNTs (light blue in Figure 10) is more interesting. In fact, the density profile is characterized by small and irregular peaks near the carbon surface, and by intense and regular peaks at large z. Interestingly, the spacing between two consecutive intense peaks at $z > 10$ Å is similar to that observed for the Pt cluster on graphite, indicating that, away from the CNTs, the 249 Pt atom cluster supported on the alternating CNTs resembles that supported on graphite. At short separations, however, the substrate surface roughness affects the cluster morphology significantly.

The disorder indicated by the density profiles could result in more steps, corners, etc. on the surface of the nanoparticles supported by nanotubes. This expectation is supported by the average coordination number of the nanoparticles, shown in Figure 11, which is calculated as a function of the simulation temperature. Bulk platinum has a coordination number of 12, while platinum nanoparticles have smaller average coordination numbers. For Pt atoms not in the bulk structure, the coordination number depends on the atom position. For example, in a perfect truncated octahedron FCC nanoparticle, atoms on a (111) surface, (100) surface, on an edge, and on a vertex have coordination numbers of 9, 8, 7, and 6, respectively. At all temperatures considered here, the platinum nanoparticles on graphite have a higher average coordination number than those observed on CNT-based substrates. This indicates that clusters on nanotubes have more low-coordination-number atoms compared to clusters on graphite, which means nanotube-supported clusters could exhibit more catalytic activity for specific chemical reactions. It should be noted that one specific chemical reaction may be sped up by Pt atoms of coordination number, say, 5, while another might be sped up by coordination number 7. Thus for the purpose of obtaining the optimum catalyst for a given application it is crucial to understand how to maximize the amount of metal atoms with a specific coordination number. To further understand how the choice of substrate can affect the catalytic activity of a platinum nanoparticle, we calculated the coordination number of all the atoms in the nanoparticle. In Figure 12 we report the number of atoms having coordination number of 6, 7, 8 and 9. The type of substrate does not appear to have a significant effect on the number of atoms with coordination number 6 or 7, as these coordination numbers exhibit the same trends as a function of

temperature on all four substrates. The number of atoms with coordination number 6 increases as the temperature increases, while the number of atoms with coordination number 7 increases from 400 to 600 K, then reaches a plateau. More interestingly, the number of atoms having coordination number 8 and 9 appears to be affected by the substrate. Our results indicate that at temperatures from 500 K to 700 K, the nanoparticles supported by carbon nanotubes have a higher number of atoms with coordination number 8 compared to those supported on graphite. Also, the carbon nanotube-supported nanoparticles have fewer atoms with a coordination number of 9 from 500 K to 900 K compared to those supported on graphite. Thus, based on the reaction of interest, simulations such as those reported here could allow one to select the substrate that maximizes the number of metal atoms with a specific coordination number.

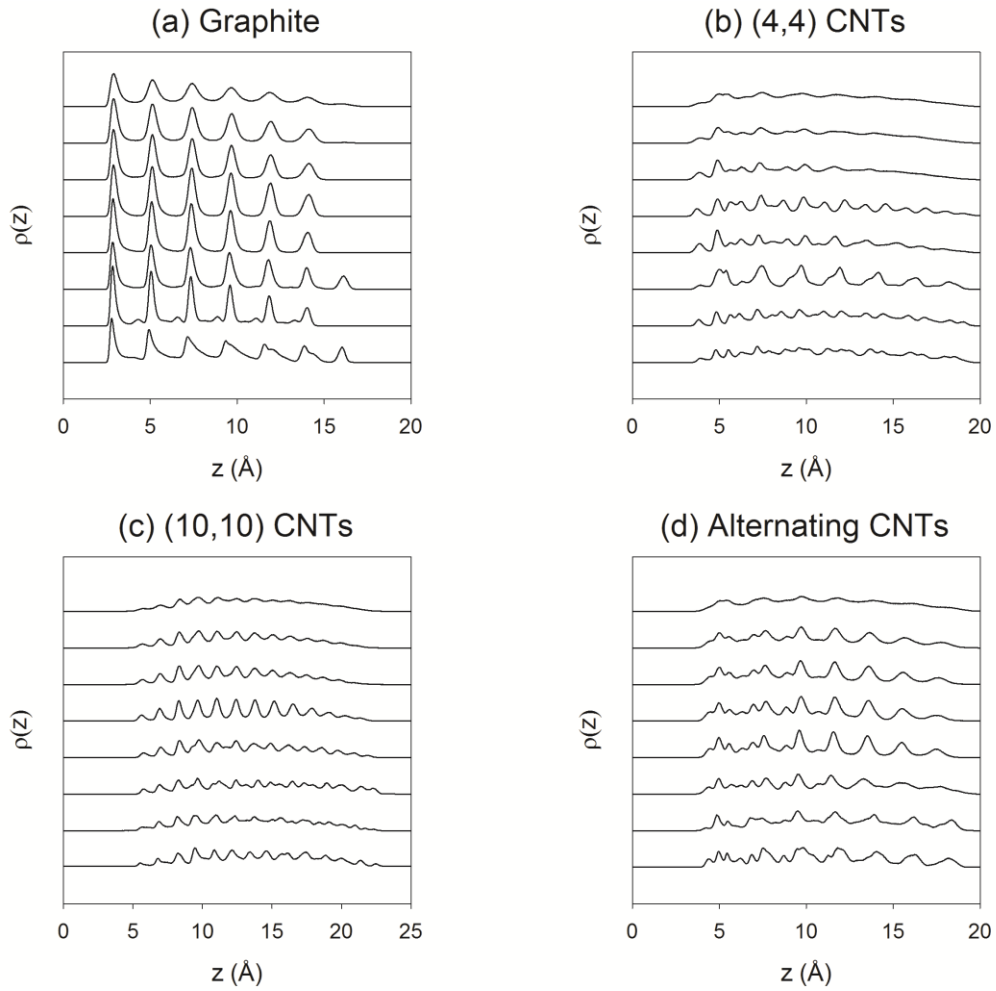

Figure 9: Density profiles for Pt_{249} on (a) graphite, (b) (4,4) CNTs, (c) (10,10) CNTs, and (d) alternating CNTs. Temperatures from bottom to top are 400, 500, 600, 700, 800, 900, 1000, and 1100 K.

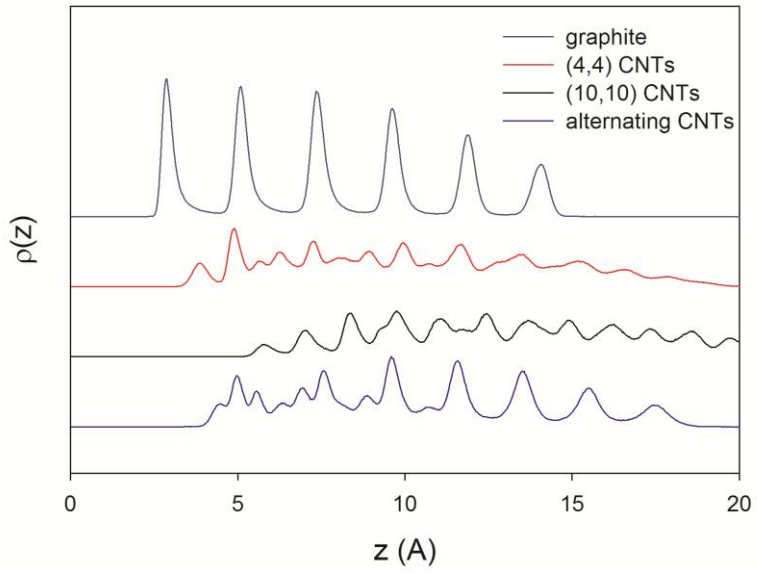

Figure 10: Comparison of density profiles of Pt_{249} supported by, from top to bottom, graphite, (4,4) CNTs, (10,10) CNTs, and alternating CNTs. Temperature is 700 K.

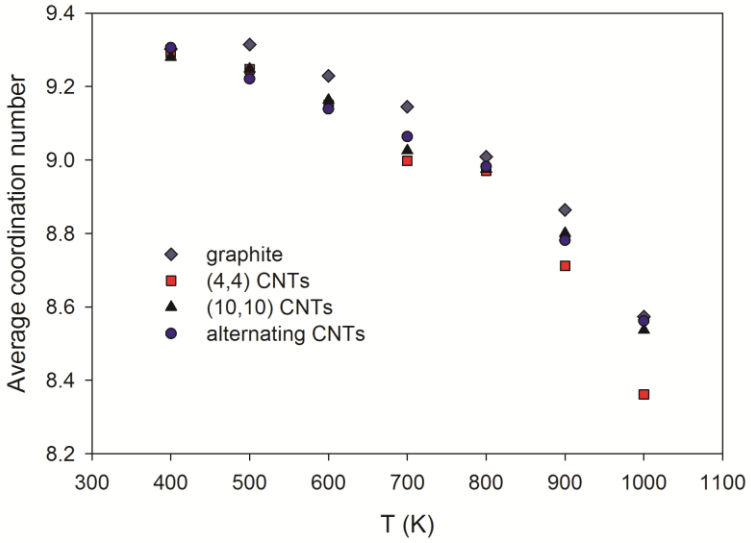

Figure 11: Average coordination numbers of Pt_{249} on graphite (diamonds), (4,4) CNTs (squares), (10,10) CNTs (triangles), and alternating CNTs (circles).

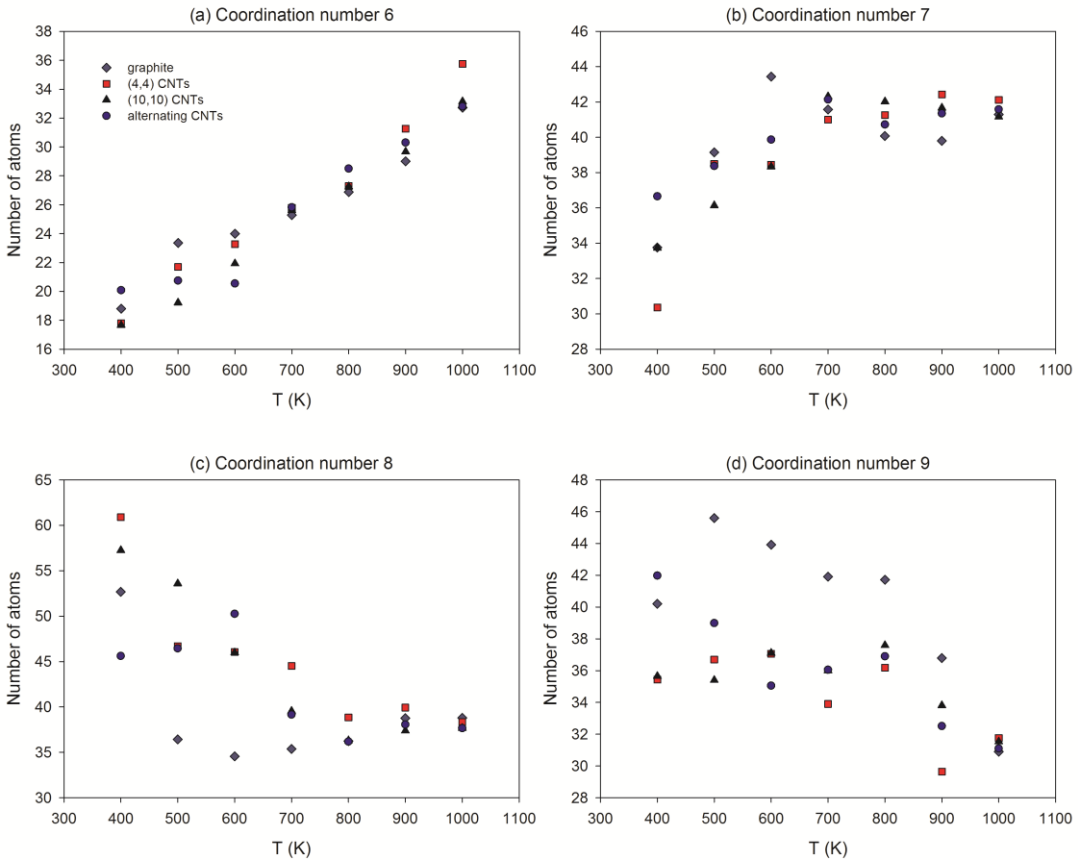

Figure 12: Number of atoms having coordination number (a) 6, (b) 7, (c) 8, and (d) 9 as a function of temperature. Different symbols represent results obtained on the four different substrates. Diamonds are for graphite, squares are for (4,4) CNTs, triangles are for (10,10) CNTs, and circles are for alternating CNTs.

2.5. Conclusions

We presented molecular dynamics simulation results for the morphology and the diffusion mechanism of platinum nanoparticles of 249 atoms supported on carbon materials. We consider supports with different geometry. Graphite was chosen for a flat substrate, and carbon nanotubes of different diameter were chosen to alter the surface roughness. Our results show that it is possible to alter the morphology and mobility of metal nanoparticles by changing their support. When deposited on carbon nanotubes,

platinum particles diffuse at a slower rate than on graphite, which should lead to increased long-term performance in catalytic applications. The lowest diffusion coefficient occurs on the substrate expected to most closely resemble experimentally produced carbon nanotube bundles, that composed of alternating (4,4) and (10,10) CNTs. The melting temperatures of the supported nanoparticles was determined by calculating the potential energy as a function of temperature and by examining the radial distribution function for those atoms near the center of mass of the nanoparticle. On all substrates examined here the diffusion coefficients reach a maximum at a temperature near the melting temperature of the metal nanoparticle. At lower temperatures the Pt nanoparticles glide over the substrates and the diffusion coefficient increases as the temperature increases, while at higher temperatures a different diffusion mechanism occurs and the predicted diffusion coefficient decreases. The results for the diffusion coefficients at T lower than the melting temperature of the supported nanoparticles were used to assess the activation energy for the nanoparticle diffusion. We found that the activation energy strongly depends on the support geometry, and is lowest on graphite and the highest on (10,10) CNTs. We also found that the nanoparticles supported by carbon nanotubes have a lower average coordination number, which could affect their catalytic behavior. These findings suggest that it is possible to tailor the behavior of metal nanoparticles by changing their support.

3. Platinum Nanoparticles on carbonaceous materials: the effect of support geometry on nanoparticle mobility, morphology, and melting

The material presented below was published in 2008 in volume 19, issue 19 of Nanotechnology.

3.1. Abstract

Molecular dynamics simulations have been used to investigate the morphology and mobility of platinum nanoparticles of various sizes supported by carbon materials. The embedded-atom method was used to model Pt-Pt interactions, and the Lennard-Jones potential was used to model the Pt-C interactions. The C atoms in the supports were held fixed during the simulations. The supports considered were a single graphite sheet and three bundles of carbon nanotubes. Three sizes of Pt nanoparticles were considered: 130 atoms, 249 atoms, and 498 atoms (Pt_{130}, Pt_{249}, and Pt_{498} respectively). It was found that for all three sizes, diffusion coefficients were approximately one order of magnitude higher for graphite-supported nanoparticles than for carbon nanotube-supported nanoparticles. In addition, increasing the size of the nanoparticle decreased its diffusion coefficient, with Pt_{130} having the highest and Pt_{498} the lowest diffusion coefficients. More interestingly, we found that for the Pt nanoparticles of all three sizes the diffusion coefficient increases as temperature increase, reaches a maximum at the melting temperature of the nanoparticle, and then decreases. The melting temperature was found to be strongly dependent on the particle size, but only slightly dependent on the features of the supports. While the size of the nanoparticle was seen to affect the particles' mobility, it did not significantly affect their structure. The nanoparticles supported by graphite have density profiles that indicate a highly-ordered, fcc-like

structure, while the particles supported by carbon nanotubes have a more disordered structure. An order parameter confirms that the nanoparticles structure depends on the support morphology.

3.2. Introduction

Metal nanoparticles supported by solid materials are widely used in catalysis. Carbon materials are often used as supports in electrocatalytic and fuel cell[73] applications because of their high electrical conductivity. Recently carbon nanotubes (CNTs) have been investigated as possible support materials for such applications. Several CNTs properties, such as their high electrical conductivity and mechanical strength, high gas transport rate, and tunable diameter, make them promising candidates for fuel cell supports. Indeed, experiments have shown that platinum-carbon nanotube composites exhibit high catalytic activity for oxygen reduction and methanol oxidation,[12-13, 18] have very high electrochemically active surface areas,[13] and are more stable under operating conditions than platinum supported by carbon black.[24] We have previously used molecular dynamics simulations to study the morphology and diffusion mechanism of 249 atom platinum nanoparticles supported on four carbon substrates.[74] Our simulations have shown that a 249 atom Pt nanoparticle deposited on graphite has a diffusion coefficient one order of magnitude higher than an identical particle deposited on carbon nanotubes. We have also found that the structure of the nanoparticle is altered by the morphology of the support. These results suggest that for this particle size, both the morphology and mobility of the nanoparticle can be tailored by appropriate choice of the support. However, even the best experimental methods produce nanoparticles

with a distribution of sizes, and the size of a nanoparticle can affect its structure and mobility, which in turn play a role in the nanoparticle's catalytic activity.[75] In this work we report our most recent results obtained, as an extension of our previous simulations, to include platinum nanoparticles of 130 atoms and 498 atoms to investigate the effect of nanoparticle size on structure and diffusion. We also employ an order parameter to more precisely pinpoint the melting temperature of the supported nanoparticles, as well as to better understand the process of melting.

3.3. Computational Details

Calculations are performed using the Large-scale Atomic/Molecular Massively Parallel Simulator (LAMMPS).[60] To model the Pt-Pt interactions we employ the embedded-atom method (EAM),[61] which was discussed in Section 2.3. We again employ a 12-6 Lennard-Jones potential[65] to model the Pt-C interactions. The Lennard-Jones parameters used here are σ = 2.95 Å and ε = 0.02206 eV. These are derived[66] by fitting the Lennard-Jones potential to simulation data for platinum obtained using a many-body potential (the Sutton-Chen potential[67]) to obtain Pt-Pt parameters, then using Lorentz-Berthelot mixing rules[65] to determine Pt-C parameters. The cutoff distance for the Pt-C interactions is set to 9.0 Å.

The carbon atoms in all substrates are fixed in place during the simulations. Lewis et al.[31] simulated gold nanoparticles on graphite with both static and dynamic substrates, and found that in both cases simulations yield qualitatively similar results. Density functional studies of a single Pt atom on a carbon nanotube[76] have indicated that the interaction between Pt and CNTs is weak, which could mean that little

deformation of the CNTs occurs and that our assumption of static substrates is sufficient. However, DFT studies of 37-atom Pt and Pt-Ru nanoparticles on graphite[77-78] have shown that adsorption of the nanoparticles causes a small deformation of the graphite sheets. Preliminary simulations we have conducted using the Tersoff potential[79] to model the C-C interactions have indicated that with the Pt-C Lennard-Jones parameters used here CNTs of large diameter only deform slightly, and that the strength of the Pt-C interaction has a significant effect on this deformation. Given the uncertainty in the Pt-C interactions, the assumption of fixed carbon atoms is expected to provide a reasonably accurate first approximation.

Our simulations were performed in the canonical ensemble[65] (constant number of atoms N, simulation box volume V, and system temperature T), using the velocity-Verlet algorithm[65] to integrate the equations of motion, with a timestep of 2.5 fs. Each simulation ran for 30 million time steps, for a total of 75 ns. The final configuration of a simulation run was used as initial configuration for the next simulation at the same temperature. Simulations were repeated at least 5 times to ensure reliable results, for a total of at least 375 ns of simulation time per system investigated.

Four substrates and three different particle sizes were used. The substrates are shown in Figure 13, and consist of (a) a single graphite sheet, (b) a bundle of (4,4) CNTs, (c) a bundle of (10,10) CNTs, and (d) alternating (4,4) and (10,10) CNTs. Platinum nanoparticles of 130, 249, and 498 atoms, with diameters of ~1.2-2.5 nm (designated as Pt_{130}, Pt_{249}, and Pt_{498} in what follows) were placed on these substrates. The nanoparticles were constructed by carving out spherical particles from bulk face-centered cubic platinum. These spheres were then annealed for 1 ns at 700 K. These

nanoparticles are shown in Figure 14. The annealed particles are placed on the substrates, and annealed for an additional 1 ns at 700 K. The final configuration of this annealing process is used as the initial configuration for subsequent simulations at temperatures of 400-1300 K. This procedure is expected to mimic the mass-selected soft-landing process with which it is possible to deposit clusters of tens and hundreds of metal atoms on solid surfaces.[80]

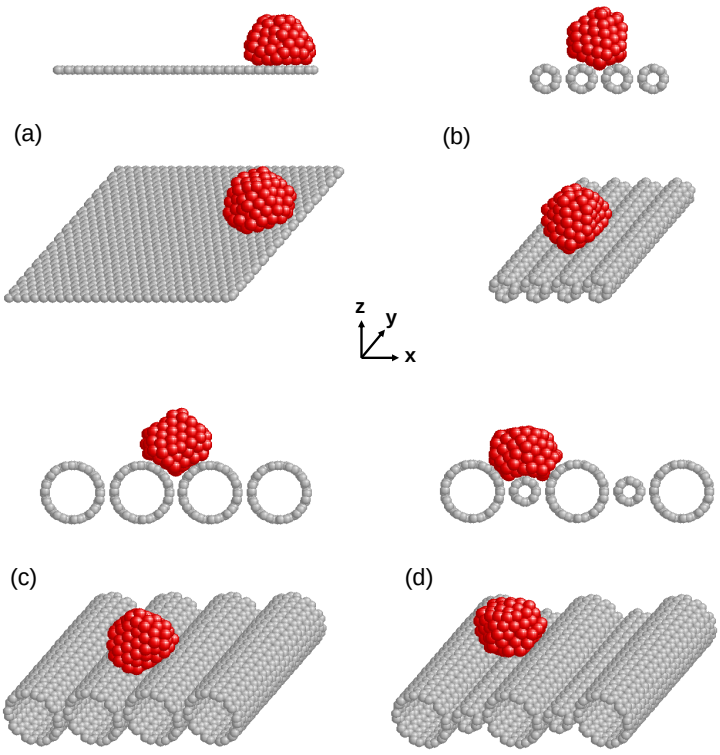

Figure 13: Snapshots of the 4 different substrates used in our simulations. (a) single graphite sheet, (b) four (4,4) nanotubes, (c) four (10,10) nanotubes, (d) alternating (10,10) and (4,4) nanotubes. In each case a Pt nanoparticle, which contains 130 atoms, is shown in red, and the carbon atoms are shown in grey. Temperature is 700 K. For visualization purposes we provide two views, one along the y-axis (top in each panel), and the second from an angle (bottom in each panel).

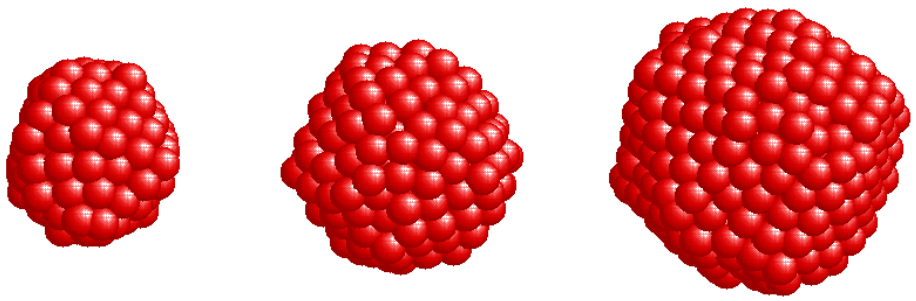

Figure 14 : Snapshots of the three platinum nanoparticles used in our simulations. Snapshots shown are from the final configuration after initial annealing at 700 K. (a) 130 atom nanoparticle (Pt130), (b) 249 atom nanoparticle (Pt249), and (c) 498 atom nanoparticle (Pt498).

The diffusion coefficient, *D*, of the cluster center of mass is determined from the mean-squared displacement $\Delta r(t)$ by the equation[65]

$$\lim_{t \to \infty} \Delta r(t) = 2nDt \quad . \tag{1}$$

In Eq (1) *n* is the number of dimensions in which the cluster is undergoing diffusion, which in our case is 2 for clusters on graphite and 1 for clusters on CNTs (see below). Results reported for *D* are the average of 5 simulations, each using the final configuration of one run as the initial configuration for the next simulation. The error in these calculations is taken to be one standard deviation.

Radial distribution functions[65] were calculated for atoms within a 5 Å radius of the nanoparticle center of mass by:

$$g(r) = \frac{V}{N^2} \left\langle \sum_i \sum_{j \neq i} \delta(r - r_{ij}) \right\rangle \quad . \tag{2}$$

In Eq (2) V is the volume of the simulation box, N is the number of platinum atoms, r_{ij} is the distance between atoms i and j, and the brackets indicate an ensemble average.

An autocorrelation function was used to examine the behavior of the Pt atoms in contact with the substrate. The term $Pt_i(t)$ describes whether or not platinum atom i is in contact with any carbon atom. $Pt_i(t)=1$ when platinum atom i is in contact with the substrate at time t, and $Pt_i(t)=0$ when the atom is not in contact with the substrate. A Pt atom is considered to be in contact with the substrate when the distance between it and any carbon atom is less than twice the distance parameter in the Pt-C Lennard-Jones interaction. The autocorrelation function C(t) is then calculated as

$$C(t) = \left\langle \frac{\sum_{i=1}^{N} Pt_i(t) Pt_i(0)}{\sum_{i=1}^{N} Pt_i(0)} \right\rangle \quad , \qquad (3)$$

where the angular brackets indicate an ensemble average. The autocorrelation function yields a constant value when the same atoms remain in contact with the substrate, and decreases as these atoms change position in the cluster and are no longer in contact with any carbon atoms. Thus by calculating C(t) we can determine if a nanoparticle glides over the substrate or if some other diffusion mechanism, such as rotation, takes place.[70]

In order to analyze the structure of the nanoparticles we calculated an order parameter, Q_6.[81-82] We define the neighbors of particle i as all platinum atoms that are within a radius of 3.4 Å from i. We then calculate

$$\overline{q}_{lm}(i) = \frac{1}{N_b(i)} \sum_{j}^{N_b(i)} Y_{lm}(\hat{r}_{ij}) \quad , \tag{4}$$

where $\hat{r}_{ij}$ is the unit vector joining atoms *i* and *j*, $N_b(i)$ is the number of neighbors of atom *i*, and Y_{lm} is a spherical harmonic. The value obtained from Eq. (4) is then averaged over all atoms in one nanoparticle to obtain the orientational order parameter

$$\overline{Q}_{lm} = \frac{\sum_{i=1}^{N} N_b(i)\overline{q}_{lm}(i)}{\sum_{i=1}^{N} N_b(i)} \quad . \tag{5}$$

Since $\overline{Q}_{lm}$ depends on the choice of reference frame,[82] a rotationally invariant order parameter is constructed, and defined as

$$Q_l = \left(\frac{4\pi}{2l+1} \sum_{m=-l}^{l} \left| \overline{Q}_{lm} \right|^2 \right)^{1/2} \quad . \tag{6}$$

The order parameter Q_6 gives values of ~0.5 for most crystalline arrangements of atoms, and equals 0 for a liquid, as described below. In some cases up to 10 independent simulations were necessary to obtain reliable values for the order parameter Q_6.

3.4. Results and Discussion

3.4.1. Diffusion

In our previous simulations[74] involving 249-atom Pt nanoparticles (see Chapter 2) we found that graphite-supported particles diffuse in two dimensions, while CNT-supported particles are constrained to diffuse primarily along the direction parallel to the CNT axis. The nanoparticles settle into the "trenches" formed by two adjacent nanotubes. The 249 atom nanoparticles were observed to hop to neighboring trenches very rarely (1-2 times in 375 ns) on (4,4) CNTs, and never on (10,10) and alternating CNTs. Similar behavior was observed for both Pt_{130} and Pt_{498}. The calculated diffusion coefficients for Pt_{130}, Pt_{249}, and Pt_{498} on each substrate are shown in Figure 15 as a function of temperature T. On each substrate, as T increases the diffusion coefficients increase in a nearly Arrhenius fashion, reach a maximum, and then decrease. In the linear Arrhenius-type region, the smaller nanoparticles have higher diffusion coefficients. At higher temperatures, above the melting temperatures of the nanoparticles, this is not always true. Diffusion coefficients for the graphite-supported nanoparticles are consistently at least one order of magnitude higher than those for the CNT-supported nanoparticles. In Figure 16 we compare diffusion coefficients at 700 K for Pt_{130}, Pt_{249}, and Pt_{498}. On all four substrates, the diffusion coefficient increases as the particle size decreases. A larger nanoparticle having a lower diffusion coefficient is the intuitive result, but Chen and Chan[33] calculated the diffusion coefficients for Pt nanoparticles of various sizes on graphite and found that D in fact did not decrease monotonically with increasing nanoparticle size. They predicted that at 298 K a 300 atom nanoparticle would have $D \approx 5 \times 10^{-9}$ cm^2/s, compared to $D \approx 8 \times 10^{-8}$ cm^2/s for a

500 atom nanoparticle. This variation of D with size was attributed to two competing factors – as nanoparticle size increases, the inertia increases, slowing diffusion, but at the same time the number of metal atoms that are not in the minima of the potential energy surface of the graphite increases. This results in faster diffusion as the nanoparticle attempts to rearrange itself so that more atoms are at the minima. Therefore, according to Chen and Chan, it is not possible to predict the change in diffusion coefficient for different sized clusters, as these size and mismatch effects have differing importance for different particle sizes. Our results indicate that larger nanoparticles consistently have lower diffusion coefficients. However, since we have only investigated three nanoparticle sizes, we cannot extrapolate our data to larger nanoparticles. It is also worth noting that all of the simulations conducted by Chen and Chan were performed at 298 K. Since the lowest temperature used in our simulations is 400 K, it is possible that the higher temperatures considered here affect the size-dependent behavior observed for the supported nanoparticles. Because of the increased atomic motion due to the high temperatures considered here, the size effect could be more important than the mismatch effect, resulting in a diffusion coefficient which always decreases as the nanoparticle size increases.

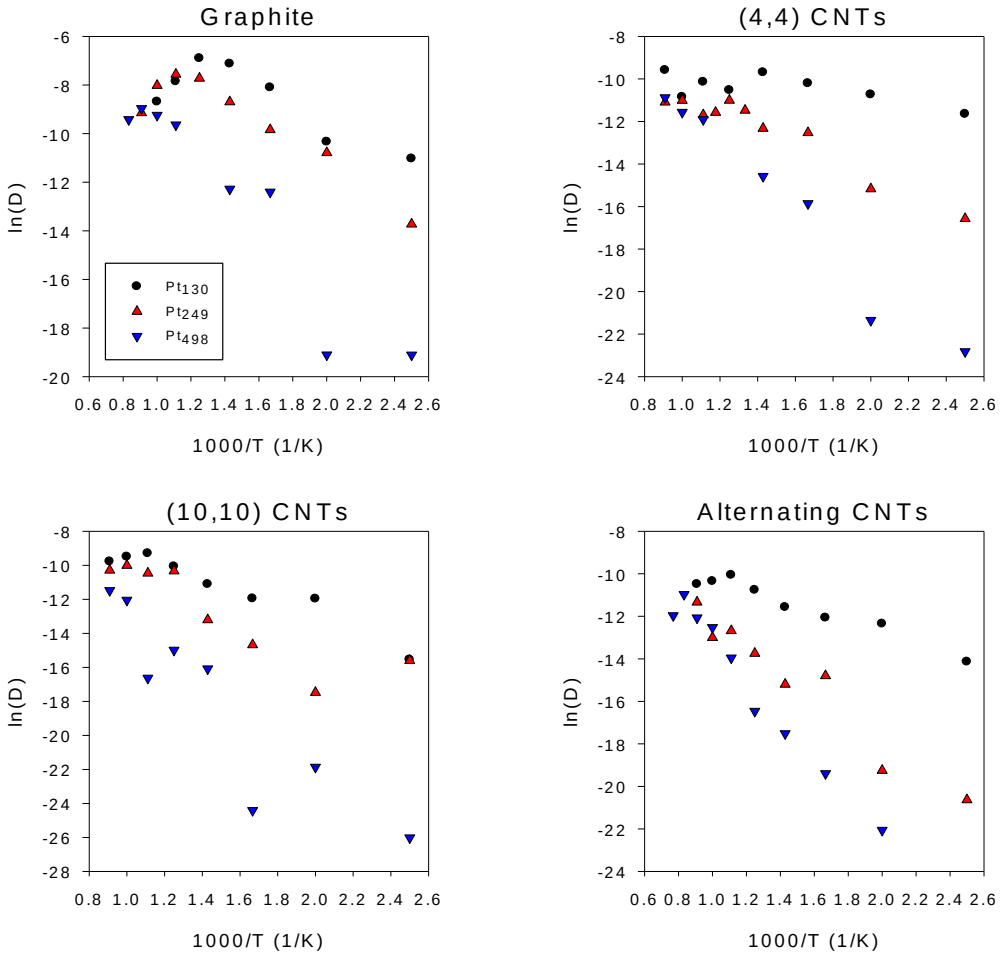

Figure 15: ln(D) vs 1000/T for Pt_{130} (black circles), Pt_{249} (red up triangles), and Pt_{498} (blue down triangles) on graphite (upper left), (4,4) CNTs (upper right), (10,10) CNTs (lower left), and alternating CNTs (lower right).

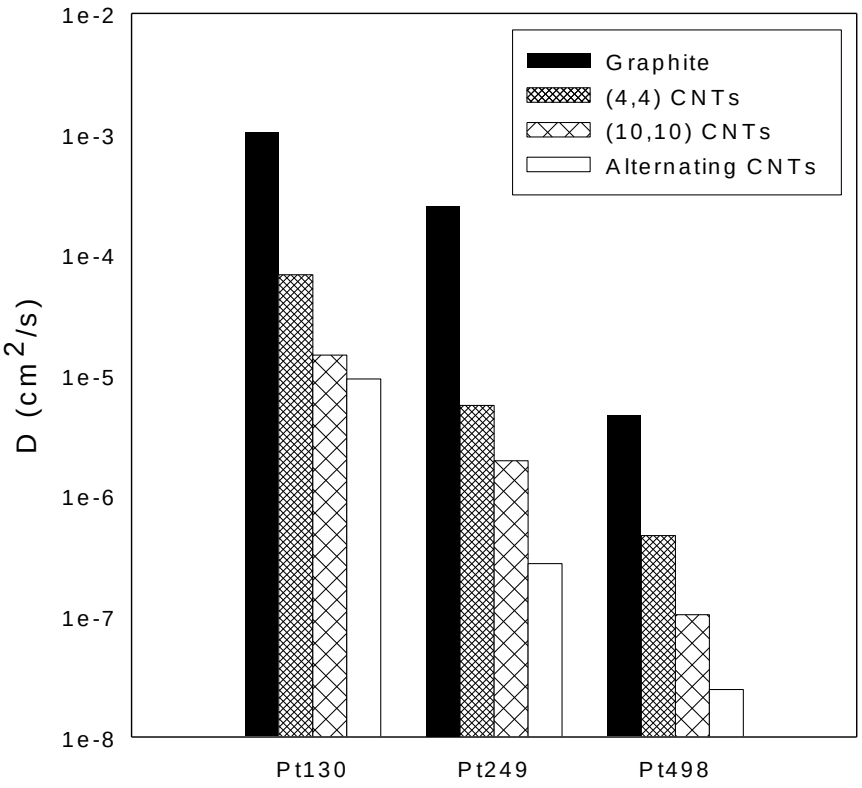

Figure 16: Diffusion coefficient at 700 K for the three Pt nanoparticles (Pt_{130}, Pt_{249}, and Pt_{498}) simulated on graphite, (4,4) CNTs, (10,10) CNTs, and alternating CNTs.

As observed for Pt_{249}, the diffusion coefficients of Pt_{130} and Pt_{498} increase as the temperature increases from 400 K in a nearly Arrhenius fashion, reach a maximum, and then decrease. We hypothesized[74] that the maximum was a result of the melting of the nanoparticle, as the temperature at which D reaches a maximum for the 249 atom nanoparticle corresponds to the melting point of that nanoparticle. To determine the melting temperatures of Pt_{130} and Pt_{498}, a radial distribution function was calculated for Pt atoms within a 5 Å radius of the nanoparticle center of mass. This radial distribution function can be used to approximately determine the nanoparticle melting temperature, and is shown for Pt_{498} in Figure 17. At 1000 K, the radial distribution function indicates

a solid structure, with sharp, well-defined peaks and several smaller intermediate peaks. The nanoparticles have a very similar structure at 1100 K, but at 1200 K the radial distribution function has only smooth, broad peaks, with the intermediate peaks disappearing completely. This type of radial distribution function is typical of a liquid, and indicates that the nanoparticle has melted. Therefore the melting temperature for Pt_{498} is between 1100 and 1200 K, which agrees very well with the temperature at which the diffusion coefficient reaches a maximum. The radial distribution functions for Pt_{130} on graphite and (4,4) CNTs are shown in Figure 18. These are similar to those for Pt_{498}, except the nanoparticles melt between 700 and 800 K. Again, the melting temperature identified by this method corresponds to the temperature at which the diffusion coefficient reaches a maximum. Interestingly, our results indicate that the melting temperature does not depend significantly on the support, but only on the size of the nanoparticle. We also point out that the determination of the melting temperature via the calculation of the radial distribution functions corroborates the results obtained by plotting the potential energy as a function of temperature for an individual nanoparticle. These results are not reported here for brevity, but sample calculations can be found in Section 2.4.1.

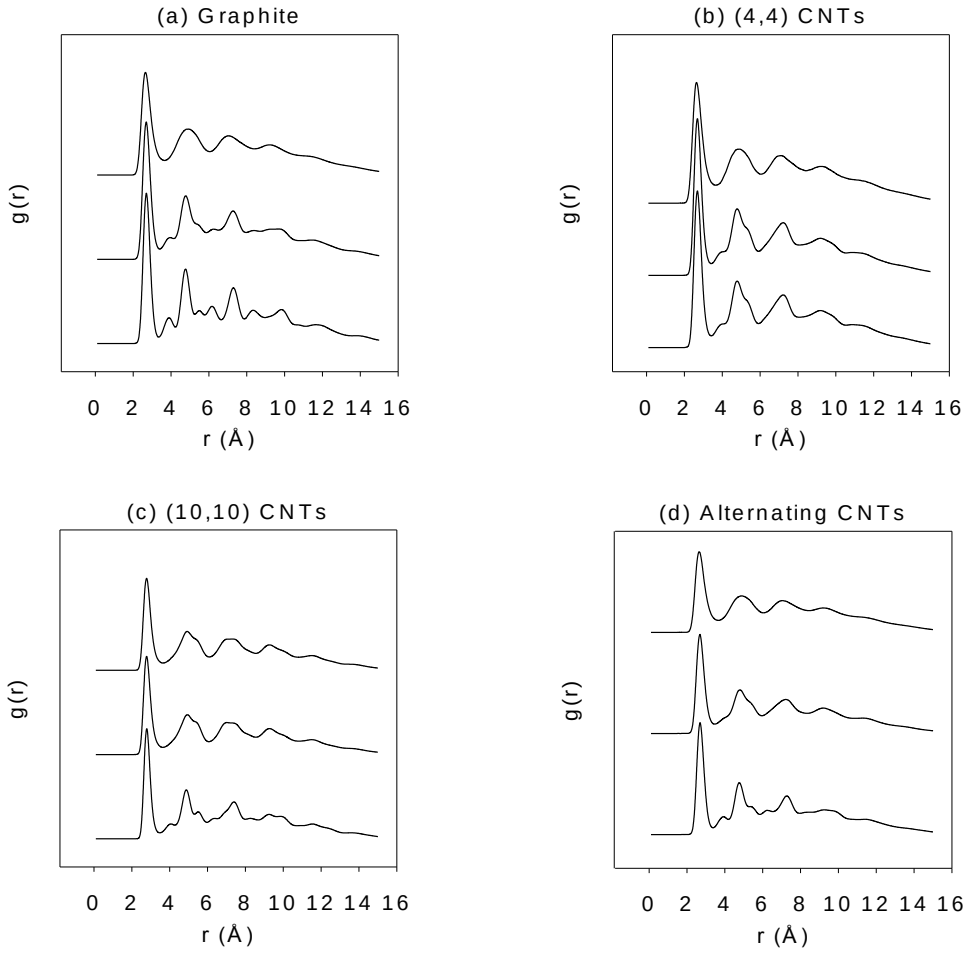

Figure 17: Radial distribution functions for Pt_{498} on (a) graphite, (b) (4,4) CNTs, (c) (10,10) CNTs and (d) alternating CNTs. The RDF is only calculated for Pt atoms within a 5 Å radius of the center of mass. Temperatures, from bottom to top, are 1000, 1100, and 1200 K.

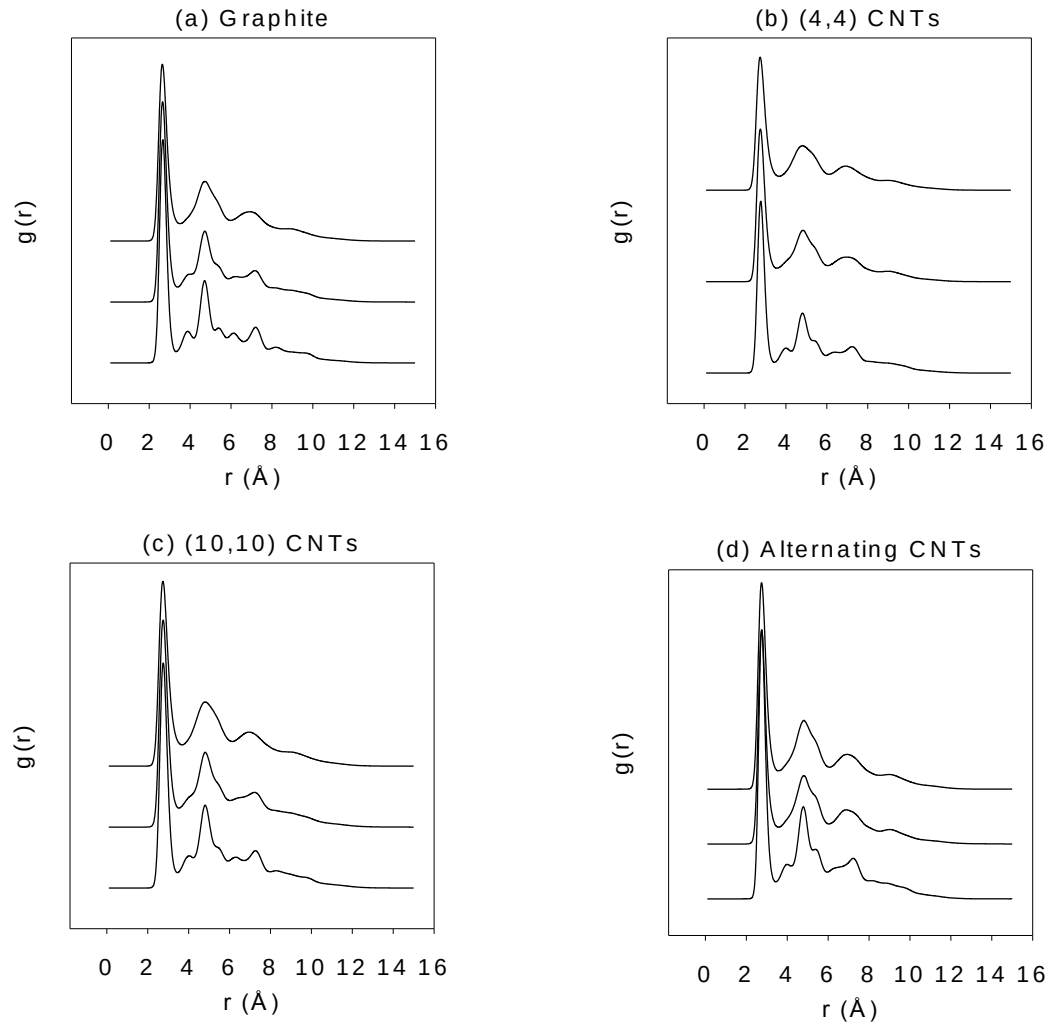

Figure 18: Radial distribution functions for Pt_{130} on (a) graphite and (b) (4,4) CNTs. The RDF is only calculated for Pt atoms within a 5 Å radius of the center of mass. Temperatures, from bottom to top, are 700, 800, and 900 K

In order to further assess the melting of the supported nanoparticles we calculated an order parameter (Q_6)[81] for the nanoparticles of interest here. In a bulk crystal, the order parameter Q_6 depends on the crystallographic arrangement of the metal atoms. In Table 2 we report the values for Q_6 for a variety of ordered crystalline structures. For our purposes, it is important to note that Q_6 equals zero for a liquid.

Table 2: Order parameters for different crystal structures.[82]

Structure	**Q_6**
Face-centered cubic	0.575
Hexagonal close-packed	0.485
Body-centered cubic	0.511
Simple cubic	0.354
Icosahedral	0.663
Liquid	0.000

Since the order parameter equals ~0.5 for regular structures and 0 for liquids, it is possible to use it to analyze the structure and pinpoint the melting temperature of a supported nanoparticle. The order parameter calculated for Pt_{130}, Pt_{249}, and Pt_{498} as a function of temperature is reported in Figure 19. The order parameter for Pt_{130} and Pt_{249} varies widely with temperature, probably because of the low number of atoms used to calculate the average order parameter. The order parameter for Pt_{498} exhibits a sharp drop from 1100 to 1200 K that corresponds to the melting of the nanoparticle. We note that Q_6 for our nanoparticles is never 0, which would correspond to a liquid structure. It is likely that this is due to the presence of the solid substrate, which affects the structure of the adjacent Pt atoms. The temperature at which Q_6 drops abruptly corresponds to the melting temperature estimated via the radial distribution functions shown in Figure 17. It is also interesting to point out that the substrate has a pronounced effect in determining the order parameter for each simulated nanoparticle. For example, Q_6 for

Pt_{498} is ~0.3 at 600K on graphite, but drops to ~0.15 on the alternating carbon nanotubes.

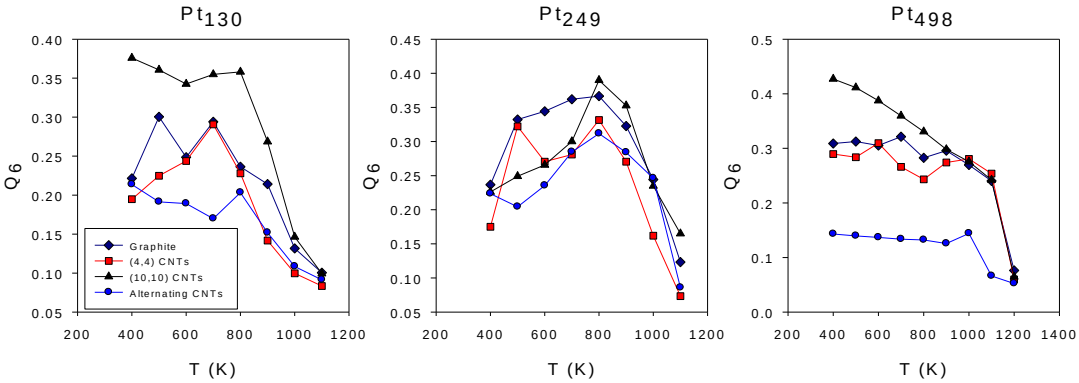

Figure 19: Order parameter for Pt_{130} (left) and Pt_{498} (right) on graphite (diamonds), four (4,4) CNTs (squares), four (10,10) CNTs (triangles), and alternating CNTs (circles).

3.4.2. Diffusion Mechanism

The process by which metal nanoparticles diffuse (gliding, rotating, etc) could affect the final structure of prepared nanoparticles, and could also result in structural changes as the nanoparticles sinter. For this reason we wish to characterize the diffusion mechanism using an autocorrelation function C(t) as described in Eq. 3. In Figure 20 we report C(t) for various temperatures for Pt_{130} and Pt_{498} diffusing on alternating carbon nanotubes. Results for nanoparticles on other substrates are similar and are not shown. We have previously performed these calculations for Pt_{249} (see Section 2.4.2).[74] Our results indicate that at low temperatures (temperatures well below the nanoparticle melting temperature) C(t) remains nearly constant as a function of time, indicating the same platinum atoms remain in contact with the substrate and the nanoparticles glide across the substrate. As the temperature increases, C(t) exhibits a gradual decrease, caused by either self-diffusion of platinum atoms within the nanoparticle, or by the

nanoparticle motion. At temperatures above the melting point C(t) drops to a value of ~0.2 in less than 0.5 ns. Visual observation of sequences of simulation snapshots indicates that such a rapid decrease in C(t) is not caused by a rotational motion of the whole nanoparticle, but rather by a more chaotic diffusion mechanism which involves all the atoms within a nanoparticle.

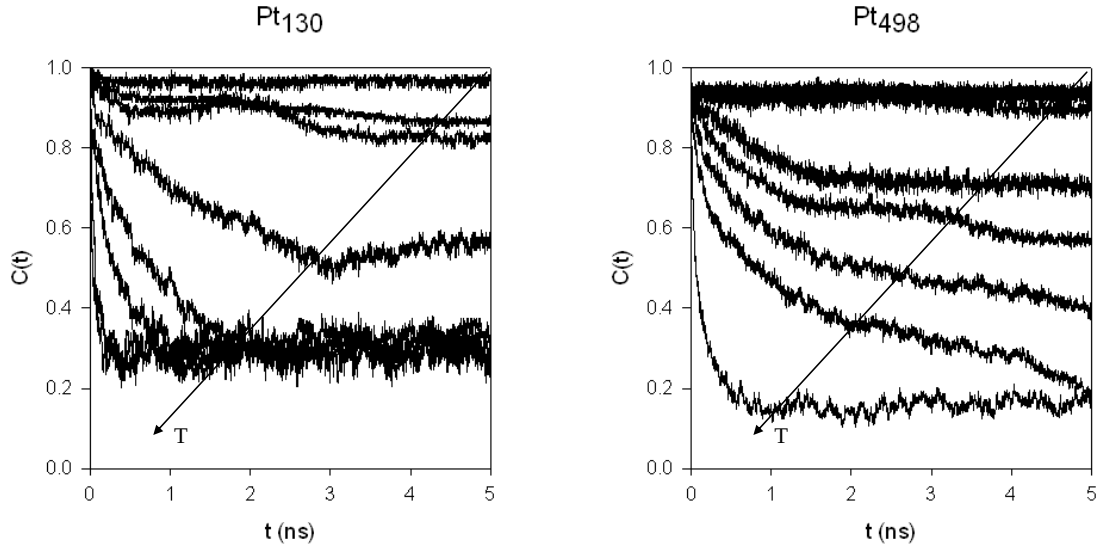

Figure 20: Autocorrelation function for Pt_{130} (left) and Pt_{498} (right) on (4,4) CNTs. Temperatures are, from top to bottom, 400, 500, 600, 700, 800, 900, 1000, 1100, and 1200 K. The arrows in both panels indicate increasing temperatures.

3.4.3. Morphology

The structure of supported metal nanoparticles can affect their catalytic activity and selectivity, so it is important to understand how different substrates affect the structure of the nanoparticles. For this purpose, we calculated the z-density profiles of the nanoparticles, which are reported for Pt_{498} in Figure 21. Density profiles for Pt_{130} and Pt_{249} are qualitatively very similar to those for Pt_{498} and are not reported here for

brevity. On graphite, the profiles have sharp, regular peaks, which indicate a highly ordered structure. The distance between consecutive peaks is commensurate with the distance between (111) planes in the FCC crystal structure of bulk Pt. When the nanoparticles are supported by CNTs, the density profiles show a number of smaller, less-defined peaks. In several of the density profiles there are changes in the structure at temperatures below the melting point of the nanoparticle, such as between 800 and 900 K on the alternating CNTs, and 500 and 600 K on graphite. These were also observed in our simulations of Pt_{249} and in previous molecular dynamics simulations of Pt nanoparticles.[57] They are attributed to an increase in mobility of Pt atoms within the nanoparticle and to surface melting. The density profiles in Figure 21 demonstrate that the CNT-supported nanoparticles have a different structure than nanoparticles supported on graphite, and this could affect both their reactivity and selectivity in catalytic applications.

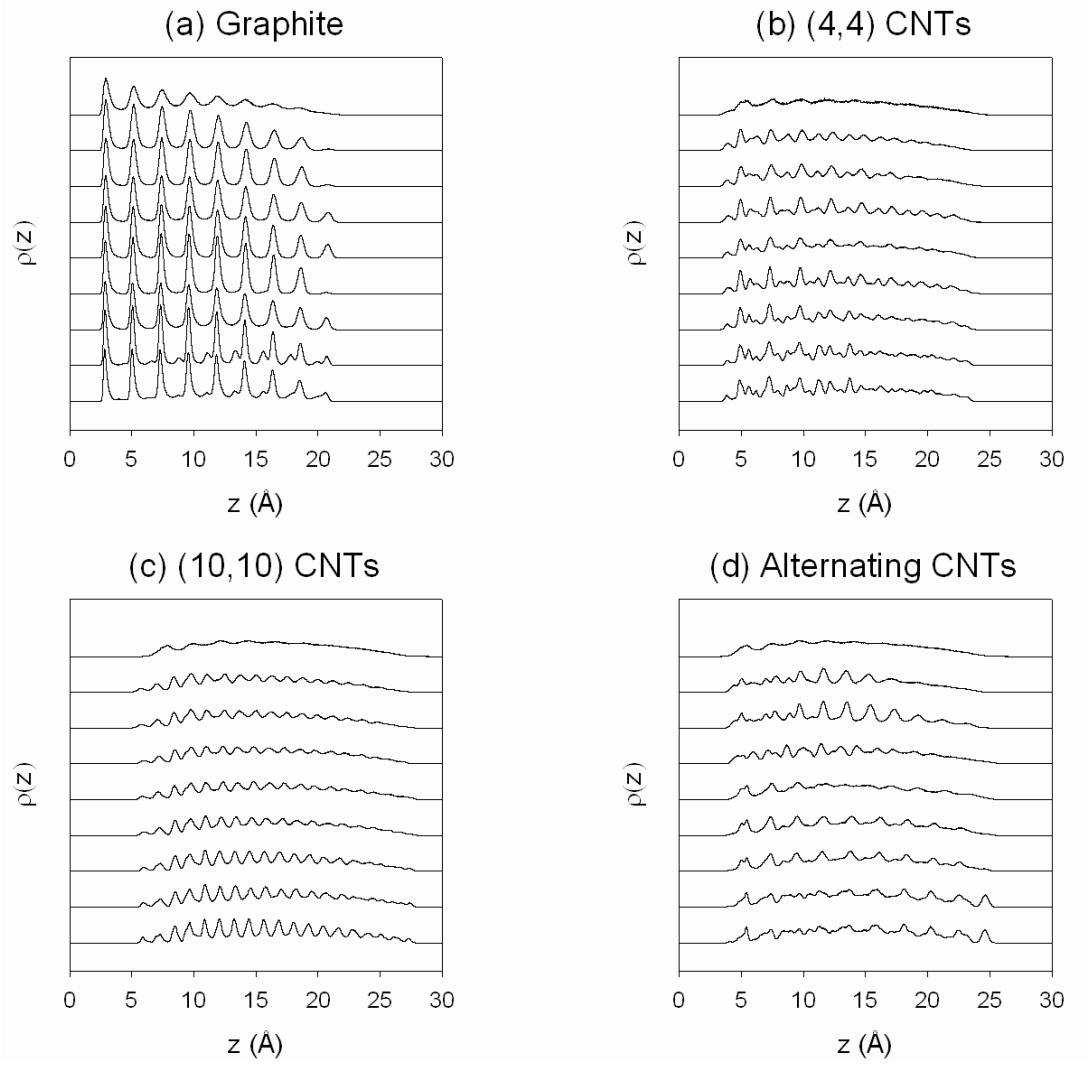

Figure 21: Z density profiles for Pt_{498} on (a) graphite, (b) (4,4) CNTs, (c) (10,10) CNTs, and (d) alternating CNTs. Temperatures, from bottom to top, are 400, 500, 600, 700, 800, 900, 1000, 1100, and 1200 K.

Another method used to characterize the structure of the supported nanoparticles was calculating the coordination numbers of those platinum atoms on the surface of the nanoparticle and not adjacent to any carbon atoms. The results are reported in Figure 22. As expected, as the size of the nanoparticle decreases, the average coordination number at a given temperature also decreases, although only slightly. For a given nanoparticle size, the average coordination numbers for the nanoparticles on all four

different substrates are nearly identical, with the largest difference occurring between Pt_{249} on alternating and (10,10) CNTs.

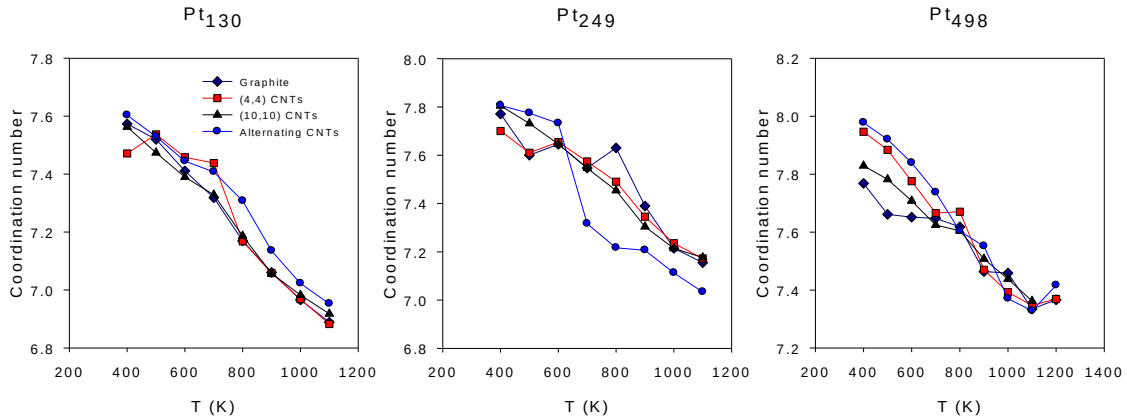

Figure 22: Average coordination number of atoms on the nanoparticle surface for Pt_{130} (left), Pt_{249} (middle), and Pt_{498} (right).

We also calculated the percentage of surface atoms having a particular coordination number. We do not count as 'surface atoms' those metal atoms that are in contact with the carbon supports. In Figure 23 we report the data obtained for coordination numbers of 5 (top), 7 (middle), and 8 (bottom). For all three nanoparticle sizes (Pt_{130}, left, Pt_{249}, center, Pt_{498}, right), the number of atoms with coordination number 5 increases with increasing temperature, and is nearly identical for nanoparticles on different substrates. The substrates have a more interesting effect on the number of atoms with higher coordination numbers. In particular, when the nanoparticle P_{249} is considered, the number of atoms with coordination number 7 increases as the temperature increases from 400 to 700-800 K depending on the substrate, but then decreases. When atoms with coordination number 8 are considered, the results in Figure 23 suggests that increasing temperature has the general effect of

decreasing the availabilily of such atoms on the nanoparticle surfaces (this is particularly true for P_{249}). The results are nevertheless interesting. For example, for Pt_{249} on (10,10) CNTs almost 41% of the surface atoms have coordination number 8 at 500 K, while only 28% of the surface atoms of Pt_{249} on graphite have that coordination number. At temperatures above about 900 K, any significant differences between the substrates disappear. This is probably due to the increased thermal energy of the platinum atoms overcoming any platinum-substrate interactions that were affecting the structure of the nanoparticles. Figure 22 and Figure 23 suggest that while the substrate morphology does not significantly alter the average coordination number of the nanoparticle's surface atoms, the relative proportions of coordination numbers change at temperatures below 900 K, and this could have an effect on the nanoparticles' catalytic activities and selectivities.

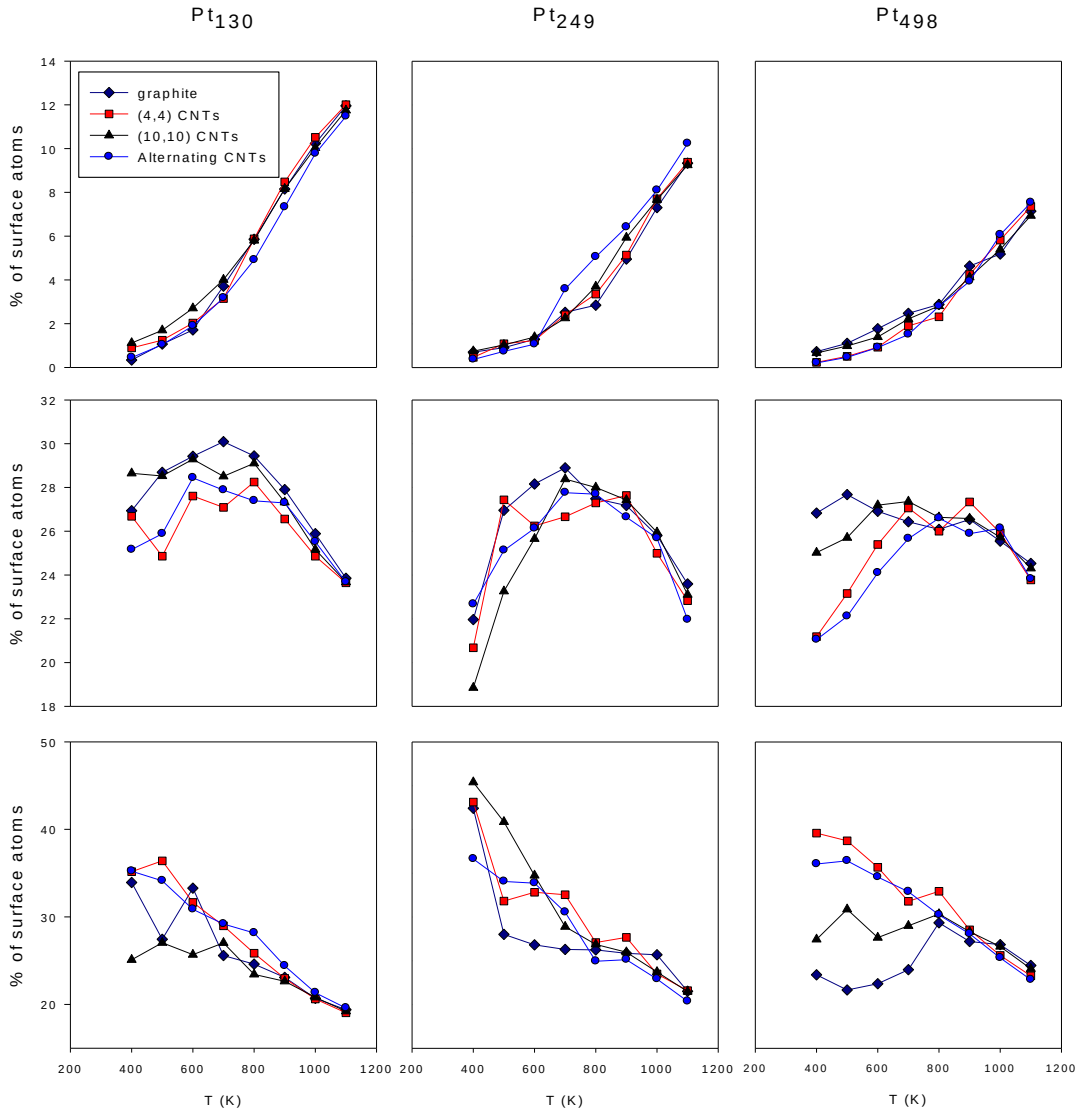

Figure 23: Percentage of surface atoms having a coordination number of 5 (top row), 7 (middle row), and 8 (bottom row) for Pt130 (left column), Pt249 (middle column), and Pt498 (right column).

3.5. Conclusions

We studied the mobility and morphology of three sizes of platinum nanoparticles on carbon supports via all-atom molecular dynamics simulations within the NVT ensemble. Using graphite and three bundles of carbon nanotubes, we

investigated how the roughness of the substrate affects the supported metal nanoparticle. For all three nanoparticle sizes (130, 249, and 498 atoms), the diffusion coefficient increases in a nearly Arrhenius manner as the temperature increases from 400 K, reaches a maximum at the melting temperature of the nanoparticle, and then decreases. Increasing the size of the nanoparticle decreases the diffusion coefficient. Pt_{130} had the highest diffusion coefficients and Pt_{498} the lowest. The predicted diffusion coefficient was the lowest on the carbon nanotube supports for all three particle sizes, which indicates nanotube-supported nanoparticles may undergo less sintering than on graphite. The structure of the nanoparticles is not affected greatly by particle size (within the limits of the current study), but is affected by the substrate. Density profiles for the nanoparticles are qualitatively similar for all three sizes, but are much more ordered for graphite-supported nanoparticles than for those supported by carbon nanotubes. Order-parameter calculations support this observation. More interestingly, the study of the coordination numbers of platinum atoms on the nanoparticles' surface revealed that while the substrate geometry does not significantly affect the average coordination number, the individual coordination numbers are altered at low temperatures. These results suggest that it may be possible to tailor the catalytic properties of supported metal nanoparticles of a wide range of sizes by changing their support.

4. Assessing How Metal-Carbon Interactions Affect the Structure of Supported Platinum Nanoparticles

The material presented below was published in 2009 in volume 35, issue 10/11 of Molecular Simulation.

4.1 Abstract

Towards understanding the effect of solid supports on the catalytic activity of supported metal nanoparticles, all-atom molecular dynamics simulations are often conducted. However, these calculations are hampered by the uncertainty related to describing metal-support interactions (typically described as Lennard-Jones potentials) at the atomic length scale. Ab initio electron-structure calculations are expected to refine such calculations by providing better estimates for the metal-support pair interaction potential. In the case of platinum nanoparticles supported on graphite, recent ab initio results suggest the correct energetic Lennard-Jones parameter should be about four times that used in previous simulation studies from our group, as well as from others. Stimulated by these findings, molecular dynamics simulations have been used here to investigate the effect of the magnitude of the metal-carbon interaction on the structure of supported metal nanoparticles. The Lennard-Jones potential was used to model the metal-carbon interactions, and the embedded-atom method was used to model the metal-metal interactions. The morphology of platinum nanoparticles of 130, 249, and 498 atoms supported on graphite and various bundles of carbon nanotubes was studied. For the larger nanoparticle it was found that, although the details of platinum-carbon interactions are important for correctly capturing the morphological details, the morphology of the support is the primary factor that determines such features. Platinum-carbon interactions affect more significantly the results obtained for metal nanoparticles supported by carbon nanotube bundles. In this case, we found that the deviations become significant for small supported nanoparticles, as well as for nanoparticles of any size supported on carbon nanotubes of small diameter.

4.2. Introduction

Supported metal nanoparticles are used in a wide variety of applications, including nanoelectronics, nanosensing, and catalysis. In catalysis, metal nanoparticles, often platinum, are used in such reactions as selective hydrogenation,[83] oxidation of formic acid and formaldehyde,[84] and, perhaps most notably, in reactions such as oxygen reduction that occur in fuel cells.[85-87] Often these nanoparticles are supported by carbon-based materials such as graphite or carbon nanotubes. The interaction between the metal and the support is important, as it affects the structure and thus the catalytic activity of the metal. Weak interactions may lead to sintering and, consequently, increased nanoparticle size. Density functional theory (DFT) can be used to study such interactions,[77, 88] but these calculations are limited to small systems containing tens of metal atoms, rather than the hundreds to thousands of atoms typically found in catalytic nanoparticles. Ab initio molecular dynamics (AIMD) can be used to study the behavior of these systems over time, although due to computational demands the time scale accessible by these simulations is limited. Molecular dynamics (MD) simulations can be used to study large nanoparticles at any temperature, and can yield dynamic properties. For example, we used MD simulations to study the structure and diffusion of platinum nanoparticles of 130, 249, and 498 atoms supported by graphite and different types of carbon nanotubes (see Chapters 2 and 3).[74, 89] Many other MD studies of supported metal nanoparticles can be found in the literature.[28, 31-35, 57, 59, 90-96] One drawback to these simulations is that there is no well-established potential for modeling the interaction of the metal with the carbon support. A simple Lennard-Jones (LJ) potential

is commonly used, often with parameters obtained from MD simulations of pure compounds (metals and carbon supports) according to the Lorentz-Berthelot mixing rules. Alternatively, the parameters could be obtained from ab initio electronic structure calculations. A recent study by Acharya et al.[97] used DFT to parameterize an LJ potential between carbon atoms in graphite and one platinum atom, obtaining a value for the LJ energy parameter, epsilon, approximately four times higher than those previously used. Other previous DFT studies for Pt adsorption on carbon nanotubes[98] revealed that the adsorption energy increases as the curvature of the support increases, almost according to a linear dependency. This suggests that the epsilon used to describe Pt-C interactions should increase as the carbon nanotube diameter decreases. In this report we have used the potential of Acharya et al., modified to account for the curvature of the support, to study how the Pt-C interactions affect the structure of platinum nanoparticles supported by graphite and carbon nanotubes.

4.3. Computational Details

Calculations were performed using the Large-scale Atomic/Molecular Massively Parallel Simulator (LAMMPS).[60] All simulations were performed in the NVT ensemble (constant number of particles *N*, simulation box volume *V*, and temperature *T*). Because we expect that the results, in terms of qualitative comparison between the morphology of the supported metal nanoparticles obtained by implementing different force fields, will not depend significantly on the simulation temperature, the simulations were conducted at 700 K, a temperature high enough to allow fast atomic mobility, but below the melting temperature of the nanoparticle.

Periodic boundary conditions were used in all simulations. The embedded-atom method (EAM),[61] which has been used to successfully model the properties of both free and supported metal nanoparticles,[99-101] was used to model platinum-platinum interactions. In the EAM model the total potential energy is given by

$$E = \sum_i F_i\left(\sum_{j\neq i} \rho_j\left(r_{ij}\right)\right) + \frac{1}{2}\sum_i \sum_{j\neq i} \phi_{ij}\left(r_{ij}\right) \quad (1)$$

where $F_i(\rho)$ is the energy required to embed atom *i* into the background electron density, ρ_j is the electron density due to atom *j*, and $\phi_{ij}(r_{ij})$ is the repulsion between the cores of atoms *i* and *j* separated by a distance r_{ij}. The force field parameters used to model platinum are those developed by Foiles and Baskes[61] as included in the Pt_u3.eam potential file in the LAMMPS package. The cutoff distance for Pt-Pt interactions is set to 5.3 Å. The simulation procedure is described at length in our previous manuscript.[74] The platinum-carbon interactions were modeled using the 12-6 Lennard-Jones potential:

$$E\left(r_{ij}\right) = 4\varepsilon_{ij}\left[\left(\frac{\sigma_{ij}}{r_{ij}}\right)^{12} - \left(\frac{\sigma_{ij}}{r_{ij}}\right)^{6}\right] \quad (2)$$

The parameter ε_{ij} has units of energy and indicates how strongly atoms *i* and *j* are attracted, while σ_{ij} has units of length and is related to the size of atoms *i* and *j*. We have used three different sets of LJ parameters in our simulations. The first set was used in our previous work[74, 89] and that of others.[34, 57, 102] The parameters were derived[66, 91] by simulating pure platinum using the Sutton-Chen many-body potential,[67] then fitting the

LJ parameters to these results. The Pt-C parameters were then obtained from the Pt-Pt parameters using C-C parameters and the Lorentz-Berthelot mixing rules.[65] These parameters, referred to in the text below as Potential 1, are ε_1= 0.02206 eV and σ_1=2.95 Å. The second set of parameters was obtained by Acharya et al.,[97] who performed DFT calculations to determine the binding energy of one Pt atom at various sites on graphite. The data were used to generate a potential energy surface, which was reproduced by appropriately fit LJ parameters. In order to match the DFT results, ghost atoms with zero mass were introduced in the center of the hexagonal carbon rings in graphite. According to this parameterization, referred to in the text below as Potential 2, the LJ parameters are ε_2=0.09 eV and σ_2=1.60 Å for the carbon atoms and ε_g=0.25 eV and σ_g=2.20 Å for the ghost atoms. In all simulations conducted below for nanoparticles supported on graphite, a single graphene sheet is used. When Potential 2 is used, ghost atoms are inserted in the center of the hexagonal rings.

Bundles of (4,4) and (10,10) carbon nanotubes (CNTs) were also considered as substrates. DFT simulations by Chi et al.[98] have shown that the binding energy of an adsorbed platinum atom increases with the curvature of the graphene substrate. For example, on a flat graphene sheet (curvature of 0 $Å^{-1}$) Chi et al. found a binding energy of 1.45 eV, while on a (10,10) CNT (curvature of ~0.147 $Å^{-1}$) the binding energy increases to ~2.28 eV. Therefore the smaller the nanotube, the higher the binding energy is. We mimic this effect by scaling ε_2 when Pt nanoparticles are supported on CNTs. The ratio of the binding energy of platinum on (10,10) CNTs to platinum on graphite, as calculated by Chi et al., is 1.517, so ε_2 was multiplied by this factor for the simulations on (10,10) CNTs. This potential is referred to in the text as Potential 3. The

(4,4) CNTs, which we have used in previous simulations, were not included in the work of Chi et al. Assuming a linear extrapolation of the binding energy versus curvature graph, we estimated the binding energy of Pt on (4,4) CNTs to be 2.07 times that on graphite and the ε parameter was scaled accordingly. This potential is referred to as Potential 4. We caution that these factors are approximate and are only used to qualitatively study the effect of curvature on the structure of supported metal nanoparticles; in fact DFT-derived force fields are not available for Pt atoms on CNTs. For this latter reason it is not possible to implement the force fields by describing 'ghost' atoms, as was done in the case of graphite. The four sets of Lennard-Jones parameters used here [two for graphite, one for (4,4) CNTs, and one for (10,10) CNTS] are summarized in Table 3.

Table 3: Summary of Lennard-Jones parameters used to describe Pt-C pair interactions

	ε (eV)	σ (Å)
Potential 1	0.02206	2.95
Potential 2	0.09	1.60
Potential 3	0.1365	1.60
Potential 4	0.1863	1.60

4.4. Results

4.4.1. Nanoparticles on Graphite

Sample simulation snapshots for Pt_{130}, Pt_{249}, and Pt_{498} on graphite at 700 K are reported in Figure 24, with the results obtained using Potential 1 on the top and those obtained using Potential 2 on the bottom. The most obvious difference occurs in the

structure of Pt_{130}, in which case Potential 2 causes the nanoparticle to flatten and spread out, while Potential 1 allows the nanoparticle to maintain a more spherical structure. As the particle becomes larger, the change due to the different potentials becomes less pronounced, although the contact angle appears smaller when Potential 2 is used. In the case of both Pt_{249} and Pt_{498}, when Potential 2 is implemented the nanoparticles show a somewhat pyramidal shape. The base is wide and the nanoparticle width decreases, to some extent, farther from the graphite sheet.

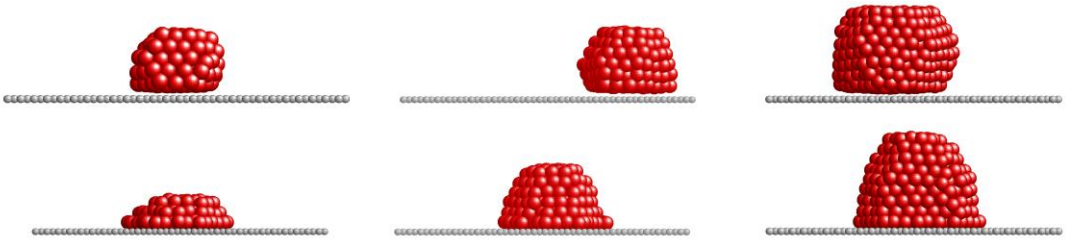

Figure 24: Simulation snapshots obtained at 700 K for Pt_{130} (left), Pt_{249} (center), and Pt_{498} (right). Platinum atoms are red, carbon atoms are gray. Snapshots obtained using Potential 1 are on the top; those obtained using Potential 2 are on the bottom.

These changes in the nanoparticle morphology were quantified by calculating a radial distribution function,[65] *g(r)*, for atoms within 5 Å of the nanoparticle's center of mass, as well as by density profiles along the z-axis (perpendicular to the graphite sheet). These results, averaged over one 1.0 ns simulation run at 700 K, are reported in Figure 25. For all three particle sizes the radial distribution functions obtained with the two potentials are similar, with the large peaks occurring at the same distances from the center. For Pt_{249} and Pt_{498} the radial distribution functions obtained using the two Pt-C potentials are nearly identical, with the positions of the intermediate peaks almost identical. In the case of Pt_{130} there are no intermediate peaks when Potential 2 is used.

To some extent, it appears that implementing Potential 2 yields less structured nanoparticles for Pt_{130}. This observation is corroborated by the snapshots shown in Figure 24, which demonstrate how Pt_{130} undergoes a dramatic change when Potential 1 was switched to Potential 2. The differences in the density profiles away from graphite (Figure 25, bottom panels) reflect the differences in morphology shown in Figure 24 and discussed above. The features of the supported nanoparticles obtained implementing Potential 1 are extensively discussed in our previous publications (see Chapters 2 and 3).[74, 89] In the case of Potential 2, because the nanoparticles assume a pyramidal structure (see Figure 24), the density profiles are consistent with the nanoparticles tapering, with peaks close to the surface enhanced and peaks farther from the surface decreased as compared to the density profile found using Potential 1. The first peak in the density profiles is also shifted closer to the graphite sheet, since σ_2 is smaller than σ_1. The position of the first peak in the density profile, which appears due to the carbon-platinum LJ size parameter, should in principle be accessible from experimental observation. Unfortunately, to the best of our knowledge, such information is not available, presumably because of experimental limitations. However, and most importantly, the distance between subsequent peaks in the density profiles of Figure 25 using both potentials is identical, indicating that the Pt-Pt interactions are strong enough to maintain the crystal structure of the platinum within the nanoparticles despite the increased Pt-C interactions.

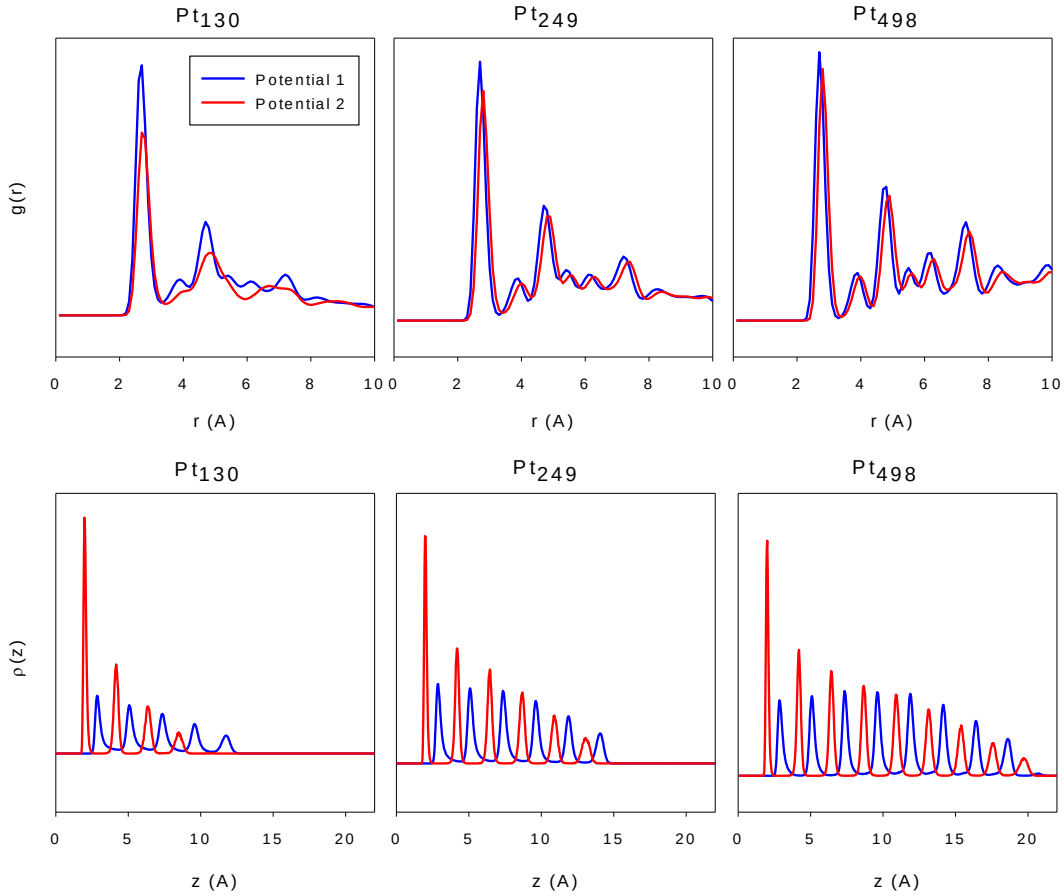

Figure 25: Radial distribution functions (top) and density profiles (bottom) for Pt_{130} (left), Pt_{249} (center), and Pt_{498} (right). Results obtained using Potential 1 are shown in blue; those obtained using Potential 2 are shown in red.

To further characterize the nanoparticles' structure we calculated the coordination numbers of the surface platinum atoms. The coordination number of a given atom is defined as the number of neighbors within 3.4 Å of that atom. The number (top) and percentage (bottom) of surface atoms having a given coordination number are reported in Figure 26. Increasing the strength of the Pt-C interaction causes a decrease in the number of surface atoms. This is a direct consequence of the change in morphology of the supported nanoparticles, and therefore the effect is stronger for the smaller nanoparticles considered. However, the percentage of surface atoms having a given coordination number does not change significantly when different potentials are used to describe Pt-C interactions. The largest difference occurs for surface atoms in

Pt_{130} with a coordination number of 8, which undergoes a decrease of about 10% when Potential 1 is switched to Potential 2.

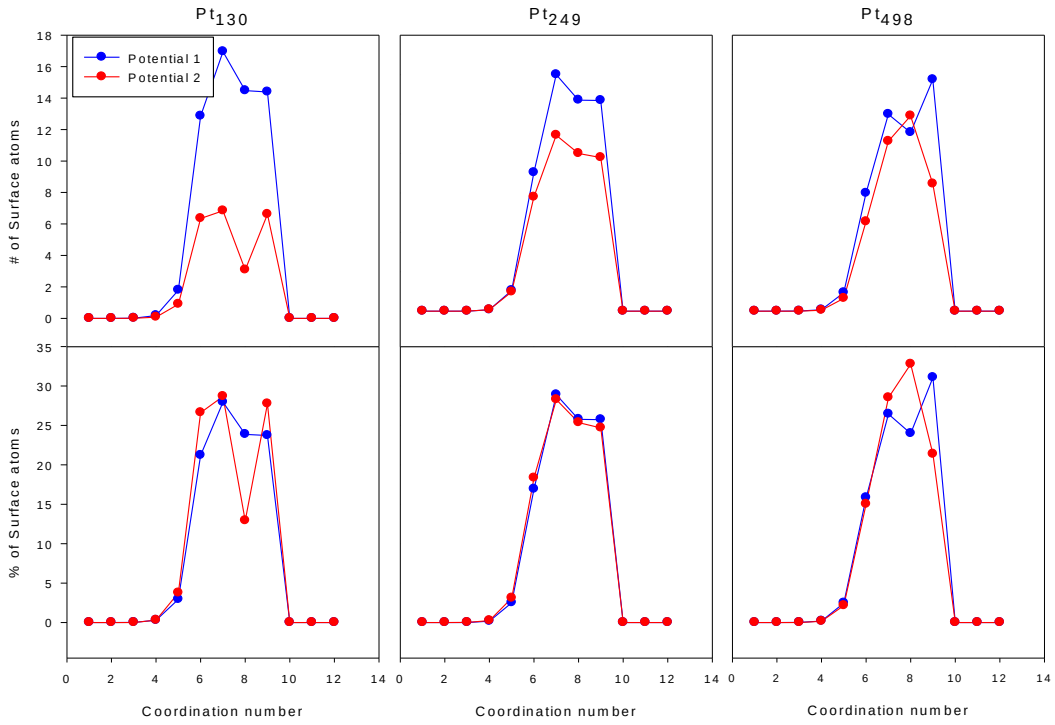

Figure 26: Number of surface atoms (top) and percentage of surface atoms (bottom) with a given coordination number for Pt_{130} (left), Pt_{249} (center), and Pt_{498} (right) on graphite. Results obtained using Potential 1 are shown in blue; those obtained using Potential 2 are shown in red.

4.4.2. Nanoparticles on Carbon Nanotubes

Additional simulations were performed for Pt_{249} supported by (4,4) and (10,10) carbon nanotubes. As described above, three sets of Lennard-Jones potentials were used for the Pt-C interactions: the base-case Potential 1, the DFT-derived Potential 2, and Potentials 3 and 4 which account for the curvature of the carbon nanotubes. Snapshots obtained at 700 K are shown in Figure 27 and Figure 28, with Potential 1 on top, Potential 2 in the middle, and Potentials 3 or 4 on the bottom. To clarify the following comments we point out that the ε parameter increases from Potential 1, to Potential 2, 3, and 4. As observed on graphite, as the LJ ε parameter increases the base of the

nanoparticle near the support becomes wider. In addition, when large ε values are used Pt atoms are pulled between the nanotubes, with this effect becoming more pronounced using Potential 4 (Figure 27, bottom panels), which is the most attractive potential considered here.

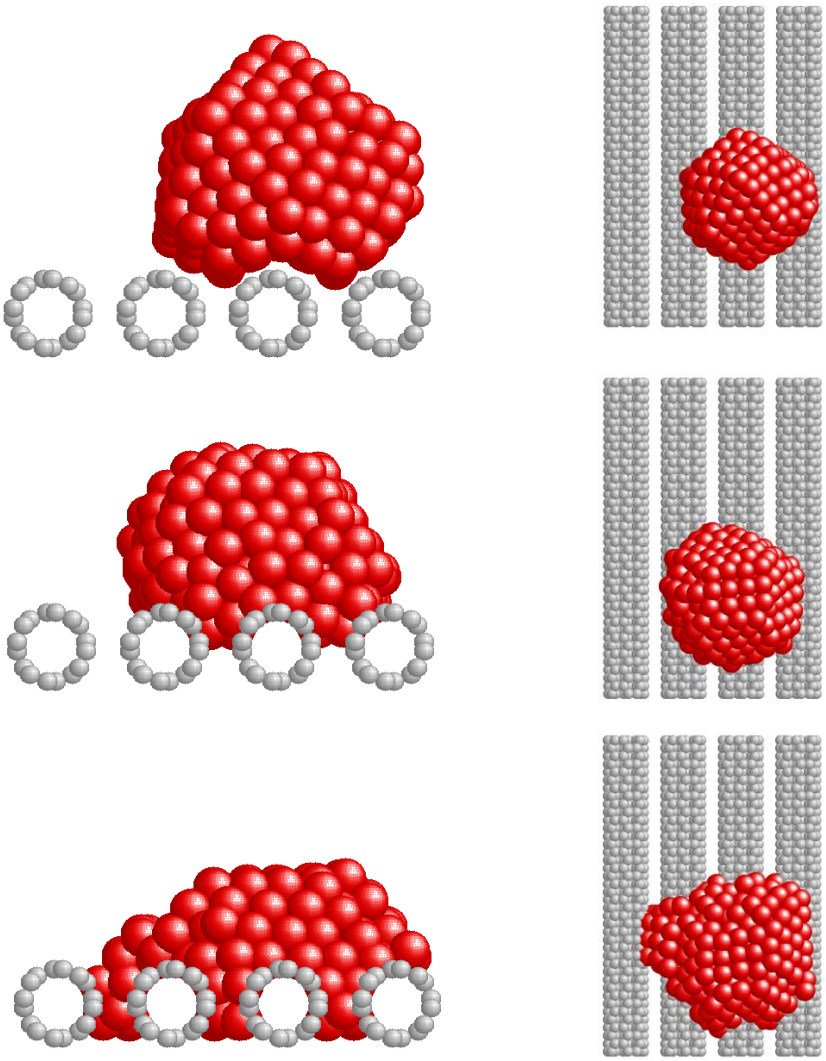

Figure 27: Side view (left) and top view (right) of simulation snapshots obtained at 700 K for Pt_{249} on (4,4) CNTs. Platinum atoms are red, carbon atoms are gray. Snapshots obtained using Potential 1 are on the top, snapshots obtained using Potential 2 are in the middle, and snapshots obtained using Potential 4 are on the bottom.

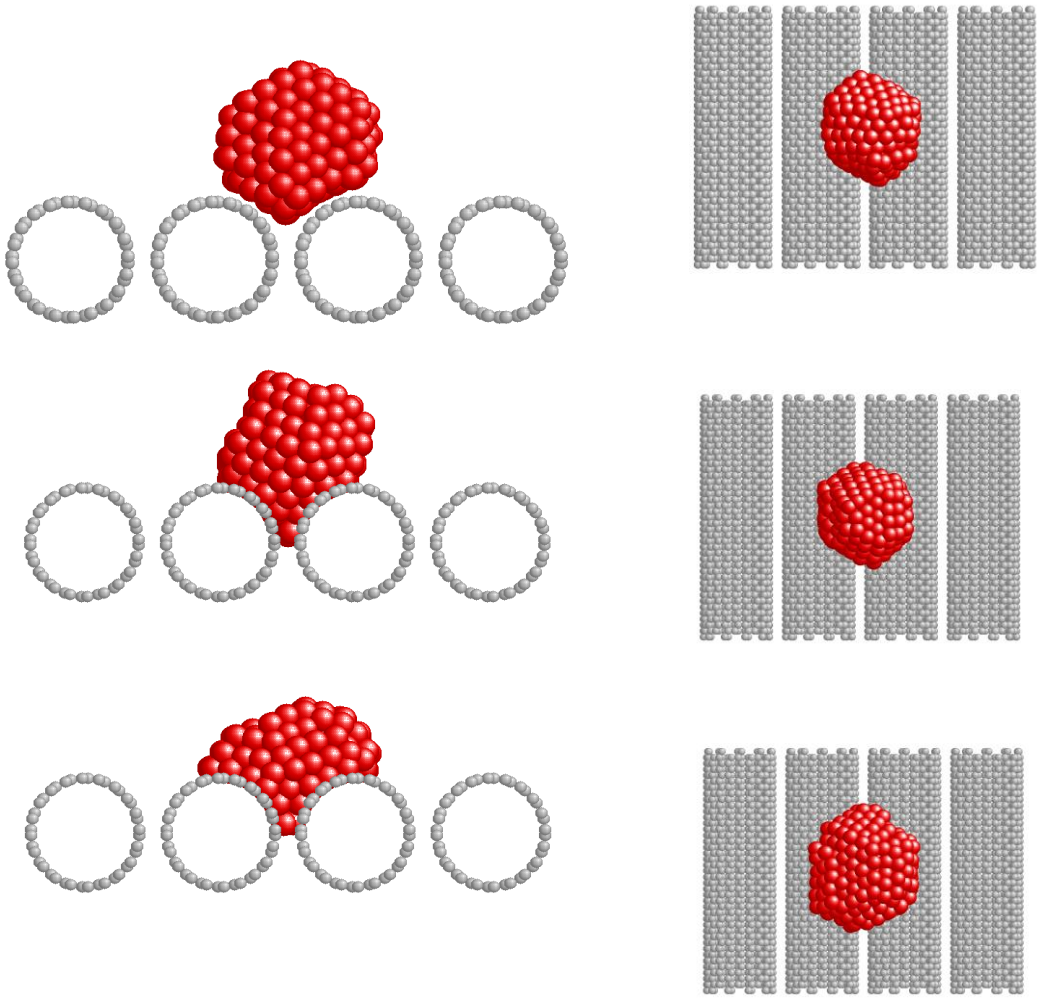

Figure 28: Side view (left) and top view (right) of simulation snapshots obtained at 700 K for Pt_{249} on (10,10) CNTs. Platinum atoms are red, carbon atoms are gray. Snapshots obtained using Potential 1 are on the top, snapshots obtained using Potential 2 are in the middle, and snapshots obtained using Potential 3 are on the bottom.

We quantified the simulation results summarized in Figure 27 and Figure 28 using density profiles perpendicular to the substrate, as reported in Figure 29. For all Pt-C potentials considered the radial distribution functions are similar to those on graphite, and are not shown for brevity. This is quite surprising given the large differences in morphologies discussed above, but is consistent with the fact that Pt-Pt interactions predominantly determine the arrangement of metal atoms near the nanoparticle center of mass.

Differences between the simulation results are more evident when the density profiles are compared. The profiles calculated using Potential 1 and Potential 2 do not exactly match, but the peaks have similar locations and intensities. The profiles calculated using Potential 2 and Potentials 3 or 4 have peaks in the same location at distances below ~10 Å, although the peaks are more intense when Potentials 3 or 4 are used. It appears that the effect of accounting for nanotube curvature within the Pt-C interaction becomes significant for nanoparticles supported on (4,4) CNTs, but is not dramatic for nanoparticles on (10,10) CNTs, although in both cases the nanoparticles are more 'flat' when Potentials 3 or 4 are implemented.

The differences and similarities between the platinum nanoparticles on graphite and on carbon nanotubes should also be examined. For both potentials, Pt on graphite has regular density profiles, with evenly spaced peaks. On carbon nanotubes, the density profiles are much more disordered, with many smaller irregular peaks, because of the structural change caused by the curvature of the nanotube. These disordered density profiles are observed independently of which Pt-C potential is implemented. The differences between the density profiles on graphite and on carbon nanotubes are indicative of a change in the nanoparticle structure due primarily to the geometry of the support. These structural changes are captured by both potentials, indicating that either would be suitable for a qualitative investigation of the structure of supported metal nanoparticles. However, our results suggest that when small nanoparticles are simulated and/or when the nanoparticles are supported on CNTs of small diameter (large curvature) the details of the force fields do affect the simulation results, and therefore,

not surprisingly, the most accurate force fields available should be implemented when all-atom MD simulations are performed.

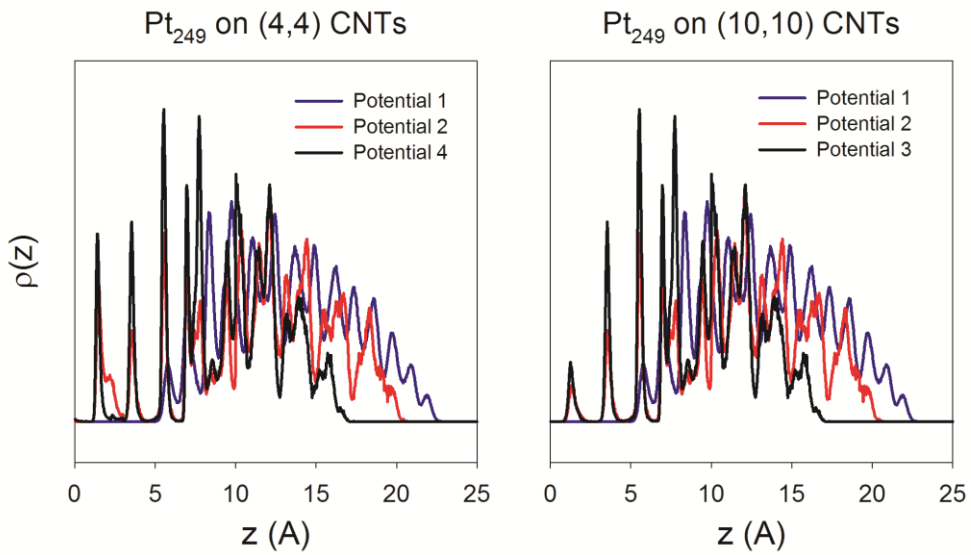

Figure 29: Radial distribution functions (top) and density profiles (bottom) for Pt_{249} on (4,4) CNTs (left) and (10,10) CNTs (right). Results obtained using Potential 1 are shown in blue, results obtained using Potential 2 are shown in red, and results obtained using Potential 3 (right) or 4 (left) are shown in black.

To complete the analysis of our comparative study we calculated the number and percentage of surface atoms with a given coordination number for Pt_{249} on (4,4) and (10,10) CNTs, reported in Figure 30. As was observed for nanoparticles on graphite, increasing the strength of the Pt-C interaction decreases the number of surface atoms, with nanoparticles simulated with Potential 1 having the most surface atoms and those simulated with Potential 3 or 4 having the least. However, the percentage of surface atoms having a given coordination number remains almost identical in all cases considered. In this case the largest difference is about 5% for atoms on the (4,4) CNTs with coordination number 8. It is expected that the differences will become smaller as the nanoparticles size increases. This latter result is encouraging when simulations such as those presented here are conducted within the field of catalysis, in which case the

coordination numbers of the surface metal atoms are expected to strongly affect the catalytic activity of supported metal nanoparticles.

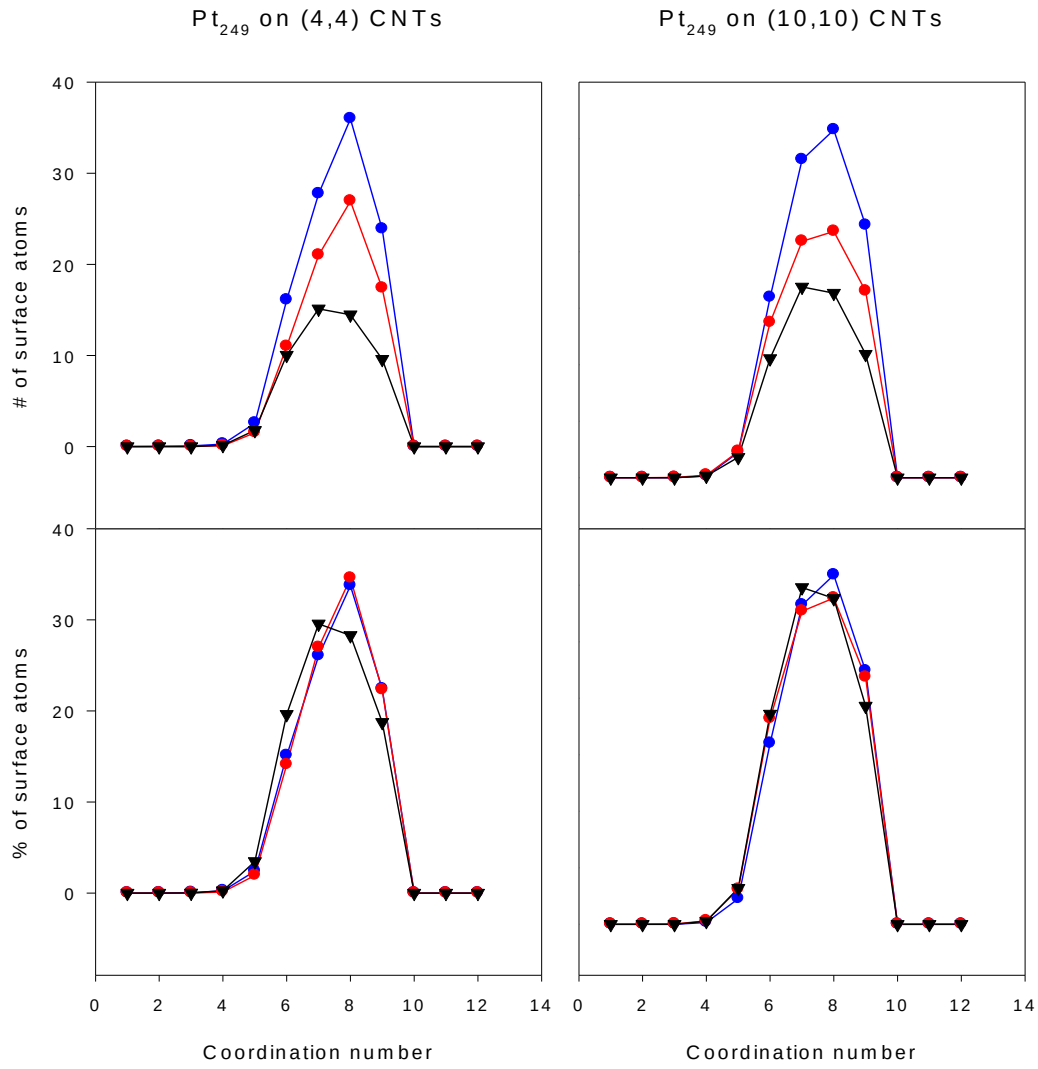

Figure 30: Number of surface atoms (top) and percentage of surface atoms (bottom) having the given coordination number for Pt_{249} on (4,4) CNTs (left) and (10,10) CNTs (right). Results obtained using Potential 1 are shown in blue, results obtained using Potential 2 are shown in red, and results obtained using Potential 3 (right) or 4 (left) are shown in black.

4.5. Conclusions

Molecular dynamics simulations were conducted for platinum nanoparticles supported on carbonaceous materials at 700 K. The results were compared when four sets of parameters were implemented to describe the metal-carbon Lennard-Jones interactions. Potential 1, taken from literature, had been derived using molecular dynamics, while Potential 2 had been derived using density functional theory. Potentials 3 and 4 were obtained by modifying Potential 2 to account for the effect of the curvature of the carbon support. The value of the LJ energetic parameter ε is approximately four times higher in Potential 2 than in Potential 1, which has been used in several previous simulations. The parameter ε further increases in Potentials 3 and 4. As expected, our calculations show that implementing different potentials to describe metal-carbon interactions quantitatively affects the results. Thus, when possible, the most accurate potentials should be used, especially when small (less than ~200 atoms) metal nanoparticles are simulated. However, limited to the conditions considered in this work, our results, expressed in terms of the density profiles of Pt atoms perpendicular to the support, radial distribution function around the metal atoms near the nanoparticles' center of mass, and number and percentage of surface metal atoms on the supported metal nanoparticles with given coordination number, do not show dramatic differences when different force fields are implemented to describe Pt-C interactions. This observation suggests that the geometry of the carbon support (i.e., flat graphite vs. curved nanotubes) is the predominant factor that affects the supported metal nanoparticles morphology, and in particular the coordination number of the metal atoms on their surfaces.

5. Supported Bimetallic Pt-Au Nanoparticles: Structural Features Predicted by Molecular Dynamics Simulations

The following material was published in 2010 in volume 81, issue 15 of Physical Review B.

5.1. Abstract

We have utilized all-atom molecular dynamics simulations to study bimetallic Pt-Au nanoparticles supported by carbonaceous materials at 700 K. Nanoparticles containing 250 atoms with 25, 50, and 75% Pt ($Pt_{62}Au_{188}$, $Pt_{125}Au_{125}$, and $Pt_{188}Au_{62}$, respectively) were considered. A single graphite sheet and bundles of seven (10,10), (13,13), and (20,20) single-walled carbon nanotubes were used as supports. It was found that $Pt_{125}Au_{125}$ forms a well-defined Pt core covered by an Au shell, regardless of the support. $Pt_{62}Au_{188}$ exhibits a mixed Pt-Au core with an Au shell. $Pt_{188}Au_{62}$ has a Pt core with a mixed Pt-Au shell. The support affects the atomic distribution. We investigated the percentage of nanoparticle surface atoms that are Pt. Our results show that for $Pt_{62}Au_{188}$ and $Pt_{125}Pt_{125}$ this percentage is lowest when there is no support and highest when carbon nanotubes are supports. We studied the size of clusters of Pt atoms on the nanoparticle surface, finding that the geometry of the support influences the distribution of cluster sizes. Finally, we found that the coordination states of the atoms on the nanoparticle surface are affected by the support structure. These results suggest that it is possible to tailor the distribution of atoms in Pt-Au nanoparticles by controlling the nanoparticle composition and the support geometry. Such level of control is desirable for improving selectivity of catalysts.

5.2. Introduction

Bimetallic catalysts have been the focus of much research because of their chemical versatility, and the ability to tune their activity and selectivity by varying their composition and size.[36] For example, bimetallic nanoparticles have been used successfully for methanol oxidation[103-104] and oxygen reduction[105-107] reactions used in fuel cells, for selective hydrogenation,[108-112] and in remediation of groundwater.[113-114] In addition to increasing activity or selectivity, it is possible to use an alloy to replace expensive metals. For example, Fernandez et al.[115] found that, when used as catalyst for the oxygen reduction reaction, carbon-supported Pd-Co showed catalytic activity close to that of carbon-supported Pt, the traditionally-used, expensive, catalyst. Carbon nanotubes (CNTs), because of their unique properties, are attractive supports for bimetallic catalysts. Pt-Ni nanoparticles on multi-walled carbon nanotubes have been shown to have improved resistance to CO poisoning during methanol oxidation,[116] and CNT-supported Pd-Rh has a high activity for the hydrogenation of benzene under mild conditions.[117]

While bimetallic catalysts show great promise, the vast number of potential catalysts poses the problem of identifying the promising candidates while limiting the number of expensive and time-consuming experiments. Computer simulation can aid in the development of new materials. For example, Linic et al.[54] used density functional theory (DFT) calculations to formulate a Cu/Ag alloy that has higher selectivity for ethylene epoxidation compared to the traditional Ag catalyst. Studt et al.,[55] by performing DFT calculations of hydrocarbon heats of adsorption, identified Ni-Zn alloys as an alternative to the Pd catalysts most commonly used for the selective

hydrogenation of acetylene in industry. Both of these predictions were verified experimentally, demonstrating that simulation can be used to develop new catalytic materials. Classical molecular dynamics (MD) simulations can also be used to study catalytic nanoparticles. While classical simulations cannot directly measure catalytic activity, they can examine the structure and dynamics of the nanoparticles at the atomic level. Such data, which cannot always be obtained experimentally, especially under operating conditions, provide insights into the performance of heterogeneous catalysts. We have previously performed MD simulations of platinum nanoparticles supported by graphite and carbon nanotubes.[74, 89] The diffusion of the nanoparticles was found to be one order of magnitude slower on carbon nanotubes than on graphite, possibly one reason for the decreased sintering for CNT-supported catalysts found experimentally.[24] We have also found that the geometry of the support affects the morphology of the nanoparticles and the coordination numbers of surface atoms, both of which features play a role in determining catalytic activity. Many other MD studies of supported metal nanoparticles can be found in the literature,[28, 31-35, 57, 59, 90-96, 118-119] illustrating the importance of this technique in characterizing heterogeneous catalysts.

Molecular dynamics has also been used to study the properties of bimetallic nanoparticles, including, e.g., the effect of size, structure, and composition on the melting behavior of unsupported Ag-Pd,[120] Au-Pd,[121-122] Cu-Ni,[123] Pd-Pt,[124] and Au-Pt[125-126] nanoparticles. Oviedo et al.[127] studied the formation of core-shell nanoparticles for combinations of Au, Ag, and Pt. Size and composition effects on the stability of Au-Pt were examined by Xiao et al.[128] Mejía-Rosales et al.[129] investigated surface sites on Au-Pd nanoparticles. Several other examples exist in the literature of MD simulations

of bimetallic nanoparticles.[130-135] Fewer studies have been reported for supported bimetallic nanoparticles. Sankaranarayanan et al.[59] studied Pd-Pt, Pd-Rh, and Pd-Cu supported on graphite. Calvo and Balbuena[136] calculated the phonon spectra of graphite-supported Pt-Ag and Pt-Au nanoparticles. Huang et al.[90] studied the structure and dynamics of graphite-supported Cu-Ni and Pt-Au nanoparticles.

In the present manuscript we consider supported Pt-Au nanoparticles. In several cases, Pt-Au alloys are more efficient catalysts than monometallic Pt or Au nanoparticles. Dimitratos et al.[137] found that carbon-supported Pt-Au had a significantly higher activity for the oxidation of glycerol than carbon-supported Pt. Comotti et al.[138] found that, for the oxidation of glucose, pure platinum yields a turnover frequency of 60 h^{-1}, while a Pt-Au alloy with a Au:Pt ratio of 2:1 results in a turnover frequency of 924 h^{-1}. It has also been reported that Pt-Au nanoparticles supported on multi-walled carbon nanotubes show good electrocatalytic activity for methanol oxidation.[45] To our knowledge, no molecular dynamics studies of CNT-supported bimetallic nanoparticles exist in the literature. We have performed simulations of Pt-Au nanoparticles containing 25%, 50%, and 75% Pt atoms, supported on graphite and bundles of different-sized CNTs. Our goal is to study the effect of composition and support geometry on the structure of bimetallic Pt-Au nanoparticles, in particular focusing on the atomic-level properties of the nanoparticle surface, which determines the catalytic activity and selectivity.

5.3. Computational Details

Nanoparticles were created by carving a 250-atom sphere out of a perfect face-centered cubic lattice. The lattice constant used was that of Pt, 3.92 Å. The lattice constant for Au is slightly larger at 4.08 Å.[139] For each composition considered the proper number of atoms (25%, 50%, or 75%), selected randomly, were designated as Pt atoms, with the remaining atoms designated as Au. Starting from this initial configuration, the nanoparticle was heated from 300 to 1000 K, then cooled to 300 K, at a rate of 100 K/ns. The annealed nanoparticle was placed on four supports: a single graphite sheet, a bundle of (10,10) CNTs, a bundle of (13,13) CNTs, or a bundle of (20,20) CNTs. Each of these systems was heated to 1000 K, and then cooled to 700 K at a rate of 100 K/ns. All subsequent production runs were performed at 700 K. This temperature is sufficiently high to permit mobility of the metal atoms, but remains below the nanoparticles melting temperature (supported Pt nanoparticles of 250 atoms melt at ~1000 K[74]). Thus the simulated nanoparticles are at conditions representative of practical catalytic applications (although no reactants or products are considered herein). Further, our results can be considered representative of supported nanoparticles produced at large T (at which condition the atomic distribution is presumably at equilibrium) and then rapidly quenched to room conditions, where the atomic mobility is reduced. Sample snapshots of $Pt_{125}Au_{125}$ nanoparticles supported on the four substrates considered are shown in Figure 31.

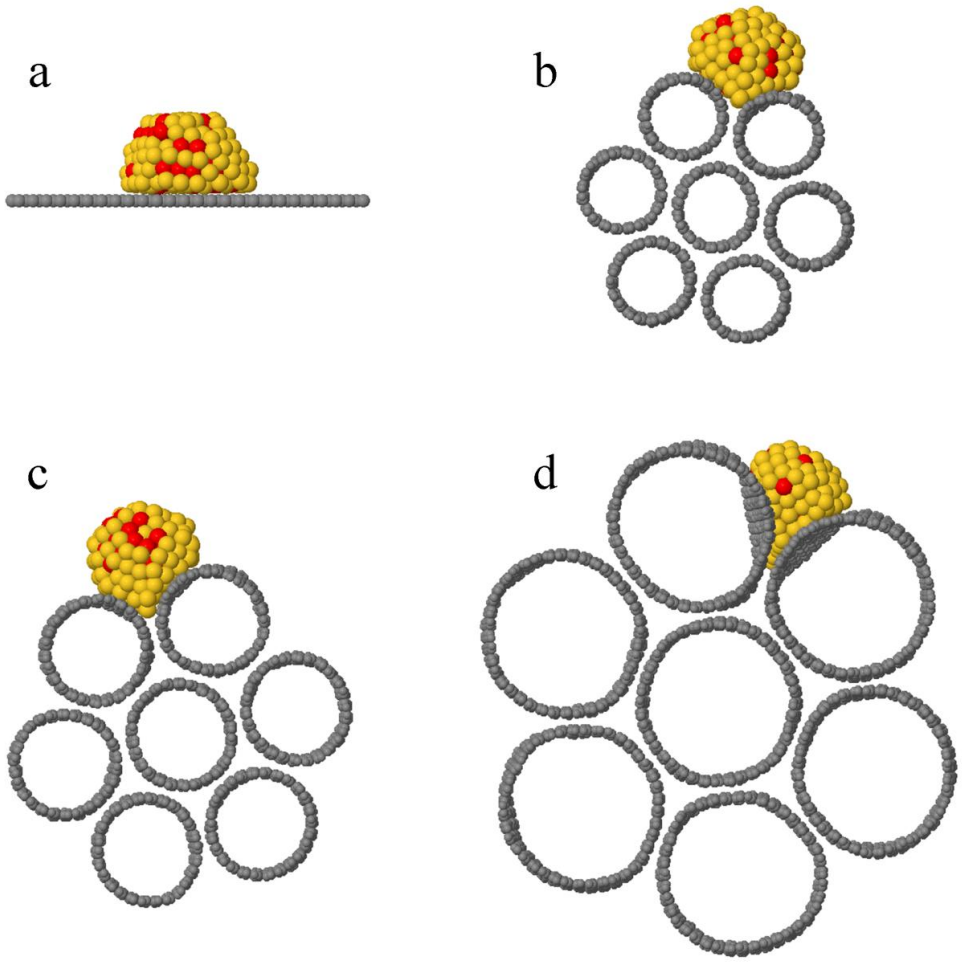

Figure 31: Snapshots of $Pt_{125}Au_{125}$ nanoparticles supported on (a) graphite, (b) (10,10) CNTs, (c) (13,13) CNTs, and (d) (20,20) CNTs. Red, yellow, and grey spheres represent platinum, gold, and carbon atoms, respectively.

Simulations were performed in the NVT ensemble (constant number of particles *N*, simulation box volume *V*, and temperature *T*) at T=700 K. All simulations were performed using the Large-scale Atomic/Molecular Massively Parallel Simulator (LAMMPS),[60] implementing the velocity-Verlet algorithm[65] to integrate the equations of motion with a 2 femtosecond timestep.

When graphite was used as a support, the carbon atoms were fixed in place. When CNTs were used as support, the carbon atoms were allowed to interact via the

Tersoff potential (see below). Periodic boundary conditions were used in all simulations.

The embedded-atom method (EAM),[61] which has been used to successfully model the properties of both free and supported metal nanoparticles,[99-101] was used to model metal-metal interactions. The force field parameters used to model platinum and gold are those developed by Foiles and Baskes[61] as included in the Pt_u3.eam and Au_u3.eam potential files in the LAMMPS package, respectively.

Carbon-carbon interactions within a CNT are described by the Tersoff potential,[79] which is a three-body potential that has previously been used to model the structural and mechanical properties of carbon nanotubes.[140-144] This force field allows the carbon atoms in CNTs to vibrate and move in response to the presence of the metal nanoparticles.

Carbon-carbon interactions between atoms in different CNTs were modeled using the 12-6 Lennard-Jones potential, using the parameters ε_{c-c} = 0.0024 eV, σ_{c-c} = 3.4 Å.[145] The Lennard-Jones potential was also used to model the metal-carbon interactions. Starting with the metal-metal parameters developed by Agrawal et al.,[146] the metal-C parameters were then obtained using the C-C parameters and the Lorentz-Berthelot mixing rules.[65] The metal-C parameters thus obtained are ε_{Pt-c} = 0.0408 eV, σ_{Pt-c} = 2.936 Å, ε_{Au-c} = 0.0332 eV, and σ_{Au-c} = 2.985 Å. Recent *ab initio* DFT simulation results suggest that these parameters for metal-carbon interactions (specifically for Pt-C interactions) may be too weak.[147] We previously performed simulations to assess the extent by which uncertainties in metal-carbon interactions affect MD results. We found that, except for small nanoparticles or for Pt nanoparticles

supported on carbon nanotubes with large curvature (small radius), the Lennard-Jones epsilon value does not significantly affect the structure of the supported nanoparticle.[148] Because the simulations performed here are conducted for rather large nanoparticles, we expect that the force fields implemented yield semi-quantitative results for the nanoparticle morphology.

5.4. Results and Discussion

5.4.1. Atomic Segregation within Nanoparticles

Snapshots for $Pt_{125}Au_{125}$ supported nanoparticles, with half of the nanoparticles not shown to provide a view of the interior of the nanoparticles, are shown in Figure 32. As can be seen from the snapshots, the gold atoms tend to segregate to the surface of the nanoparticle, leaving a Pt-rich core. The geometry of the support affects to some extent the atomic segregation. For all four supports, there is a core of Pt atoms surrounded by a shell of Au atoms interspersed with a few Pt atoms, but the supports deform the nanoparticles, thus yielding different atomic distributions compared to those observed for unsupported nanoparticles of similar composition. The support curvature in some cases enhances this effect (see, e.g., panel b in Figure 32 where it appears that Pt atoms, and not Au ones, are in contact with the CNTs). To quantify the distribution of the atoms within the metal nanoparticles we calculated the average number of atoms of each type as a function of the distance from the nanoparticle center of mass. These results for $Pt_{125}Au_{125}$ are reported in Figure 33.

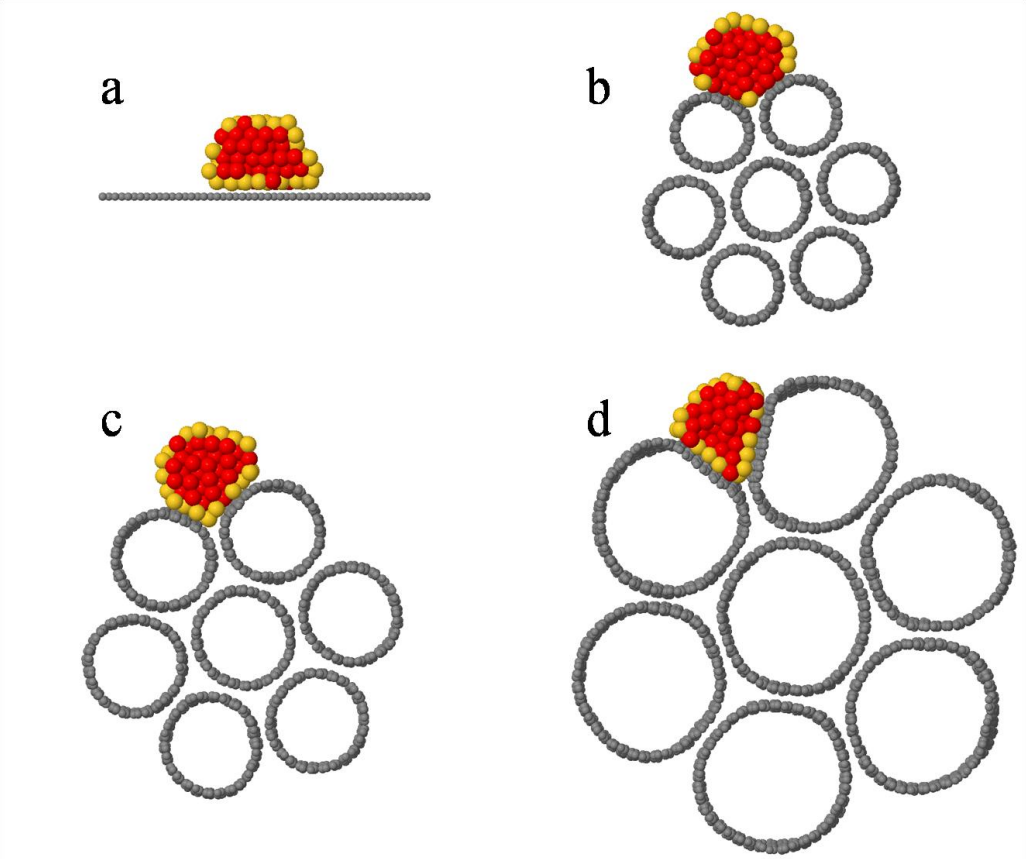

Figure 32: Same as Figure 31, but with half of the nanoparticles removed to provide a cutaway view of the interior of the nanoparticles.

Although the results are qualitatively similar for the nanoparticle in vacuum (unsupported) or supported on each carbonaceous material studied here [graphite, (10,10), (13,13), and (20,20) CNTs], some quantifiable differences can be observed as a function of the support. Closer to the center of mass of the nanoparticle only Pt atoms are present. Au atoms can be found starting at ~4 Å when the nanoparticle is supported by graphite, and at around 5-6 Å on CNTs and in vacuum. The Au atoms are concentrated farther from the nanoparticle center of mass, with the peak in their distribution occurring at around 9 Å. When the nanoparticle is unsupported, the atomic distributions show sharp peaks, reflecting the symmetric lattice structure of the metal

atoms. When supports are present, the symmetry is broken and radially averaging the distribution of the atoms results in fewer, smoother peaks. All five systems clearly indicate a well-defined Pt-Au core-shell structure, with the support affecting, albeit slightly, the radial distribution of the metal atoms. Despite the statistical uncertainty intrinsic in our calculations (the error in Figure 33 is estimated as one standard deviation from the five independent simulations conducted for each system), some of the differences observed for the atomic distribution within the nanoparticles are relevant. For example, at ~6 Å, the number of Pt atoms is lowest on (20,20) CNTs, and the number of Au atoms at ~8.5 Å is almost 2 atoms higher on (13,13) CNTs than on any other support. We do not examine these differences in any more detail, as small changes of the arrangement of the interior atoms are not expected to have a significant effect on the catalytic activity of the nanoparticle. The segregation of the Au atoms to the nanoparticle surface is driven both by the fact that Au atoms have larger diameters than Pt atoms and because Au has a lower surface energy than Pt. Thermodynamic models[128] and MD simulations[125, 128, 149] have predicted the formation of Pt-Au core-shell nanoparticles. Reyes-Nava et al.[150] used atomic properties of constituent elements to predict trends for surface segregation in bimetallic nanoparticles, and supported their predictions with MD and DFT calculations. Their results indicate an Au-rich shell in Pt-Au nanoparticles, in agreement with our results. Pt-Au core-shell nanoparticles have been observed experimentally,[151-154] although metastable Au-Pt core-shell nanoparticles can also be formed[155-156] which are not in thermodynamic equilibrium.

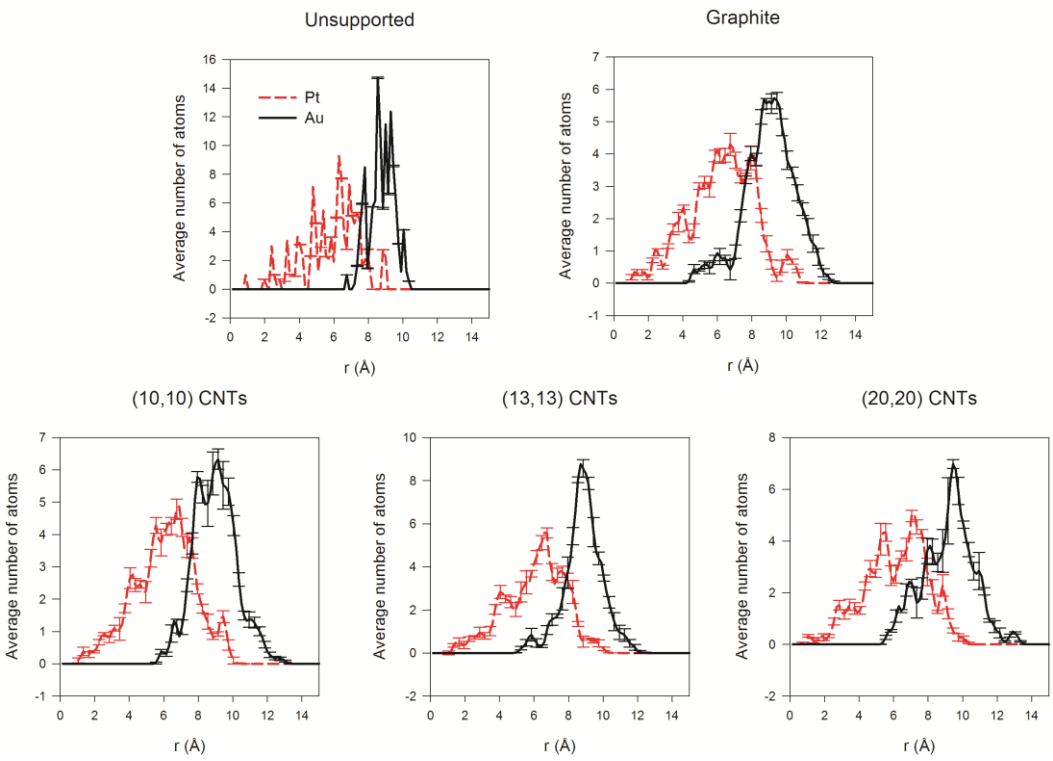

Figure 33: Number of Pt (red) and Au (black) atoms as a function of distance from the nanoparticle center of mass for $Pt_{125}Au_{125}$ in vacuum (unsupported), and on the four carbonaceous supports considered. The statistical uncertainty is estimated as one standard deviation.

As detailed below, and not surprisingly, our simulations show that the atomic distribution within the nanoparticles changes more significantly when the nanoparticle composition varies. In Figure 34 we report the atomic distribution as a function of distance from the center of mass for $Pt_{62}Au_{188}$, $Pt_{125}Au_{125}$, and $Pt_{188}Au_{62}$ nanoparticles, all supported by (10,10) CNTs. Results for $Pt_{62}Au_{188}$ and $Pt_{188}Au_{62}$ on all the supports are not shown for brevity, because the atomic distributions are qualitatively similar for all cases studied. Specifically, in the case of $Pt_{62}Au_{188}$, there are not enough Pt atoms within the nanoparticle to form a well-defined core-shell structure. There are Au atoms found at less than 2 Å from the center of mass, compared to $Pt_{125}Au_{125}$ where Au atoms are at least 5 Å away from the center of mass. The distributions of Pt and Au atoms are

nearly equal within ~7 Å of the center of mass, indicating that they are evenly mixed near the center of the nanoparticle. More than 7 Å away from the center of mass the nanoparticle is almost exclusively composed of Au atoms. As discussed above, $Pt_{125}Au_{125}$ nanoparticles display a Pt-Au core-shell structure. In the case of $Pt_{188}Au_{62}$ nanoparticles, aside from a small peak near 2 Å, there are no Au atoms present within 7 Å of the nanoparticle center of mass. At ~9 Å from the center of mass, Pt and Au are mixed, with slightly more Au atoms present at any given distance. Summarizing, our results show that $Pt_{125}Au_{125}$ nanoparticles consist of a core almost entirely composed of Pt and a shell consisting almost entirely of Au. When fewer Pt atoms are present, as in $Pt_{62}Au_{188}$, a mixed Pt-Au core covered by a nearly pure Au shell is formed. When the nanoparticle is predominantly Pt, as in $Pt_{188}Au_{62}$, the structure consists of a pure Pt core covered by a mixed Pt-Au shell.

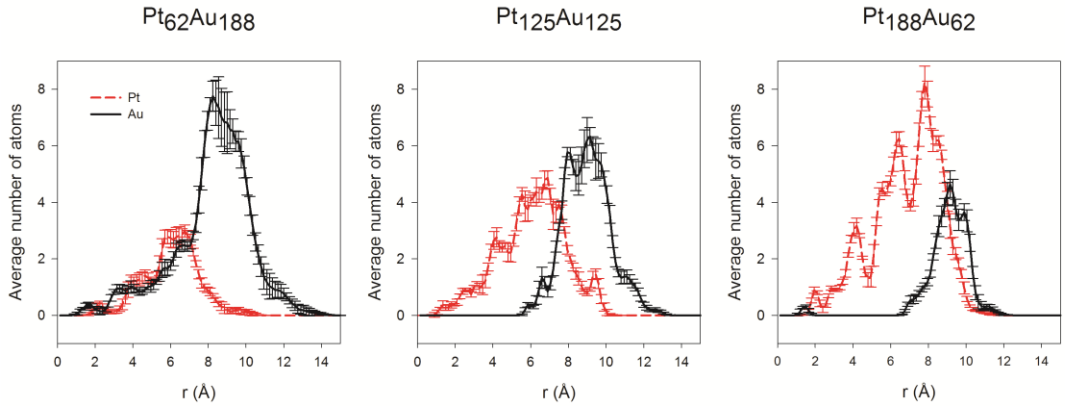

Figure 34: Number of Pt (red) and Au (black) atoms as a function of distance from the nanoparticle center of mass for $Pt_{62}Au_{188}$, $Pt_{125}Au_{125}$, and $Pt_{188}Au_{62}$ nanoparticles supported by bundles of (10,10) CNTs. The statistical uncertainty is estimated as one standard deviation.

5.4.2. Nanoparticle Surface Characterization

The different distributions of Pt and Au atoms in the nanoparticles' shells suggest that the atomic distribution on the nanoparticle surface may depend on the nanoparticle composition, and to some extent also on the support. Because of the importance of such results in catalysis, we quantify herein the distribution of atoms on the nanoparticle surface. In Figure 35 we report the percent of surface atoms that are platinum for each of the three compositions considered, as a function of the support. The values reported are the averages of five simulations, and the error bars represent one standard deviation in each direction. In the case of $Pt_{188}Au_{62}$, our calculations show the percentage of surface atoms that are platinum ranges from 55% for unsupported nanoparticles to 62% for nanoparticles supported by (13,13) CNTs, without a clear trend as a function of support. For both $Pt_{62}Au_{188}$ and $Pt_{125}Pt_{125}$ nanoparticles the percentage of surface atoms that are platinum is lowest when there is no support, increases on graphite, and is highest when CNTs are used as supports, increasing slightly as the CNT radius increases, except for $Pt_{62}Au_{188}$, where the percentage decreases slightly on (20,20) CNTs. As can be seen in detail in the bottom panel of Figure 35, for the $Pt_{62}Au_{188}$ nanoparticle the percentage ranges from 8.9% on (10,10) CNTs to 11.6% on (13,13) CNTs. For the $Pt_{125}Au_{125}$ nanoparticle the percentages ranges from 18.1% on (10,10) CNTs to 19.0% on (20,20) CNTs.

To explicitly quantify the results for the surface composition, in Figure 36 we report the number of Pt atoms on the surface of the three nanoparticles as a function of the support. The results in Figure 36 are quite important. For example, in the $Pt_{62}Au_{188}$ nanoparticle in vacuum <1% of the Pt atoms are on the surface, while when the same

nanoparticle is supported by (13,13) CNTs, ~10 of the 62 Pt atoms (~16% of the Pt atoms) are located on the nanoparticle surface. As another example, in the $Pt_{188}Au_{64}$ nanoparticle on graphite ~35% of the Pt atoms are on the nanoparticles surface, but when the same nanoparticles is supported on bundles of (20,20) CNTs only ~17% of the Pt atoms are available for catalytic applications. Note that the total number of Pt atoms on the nanoparticles surface can change even though the percentage of Pt atoms on the surface does not vary because when the support changes, due to the effective surface roughness, the nanoparticles rest between contiguous nanotubes, and the total number of surface atoms changes compared to when the nanoparticles rest on a flat graphite surface. We do not count as 'surface atoms' those metal atoms that are in contact with the carbon supports. As the number of Pt atoms on the surface varies, their coordination state (as discussed below) also varies. This effect, when considered combined for the large number of nanoparticles typically used for practical catalytic applications, will yield macroscopic effects on both catalytic activity and selectivity. Overall, the results in Figure 35 and Figure 36 suggest that for Pt-Au bimetallic nanoparticles it is possible to control the nanoparticle surface features by choosing the appropriate support.

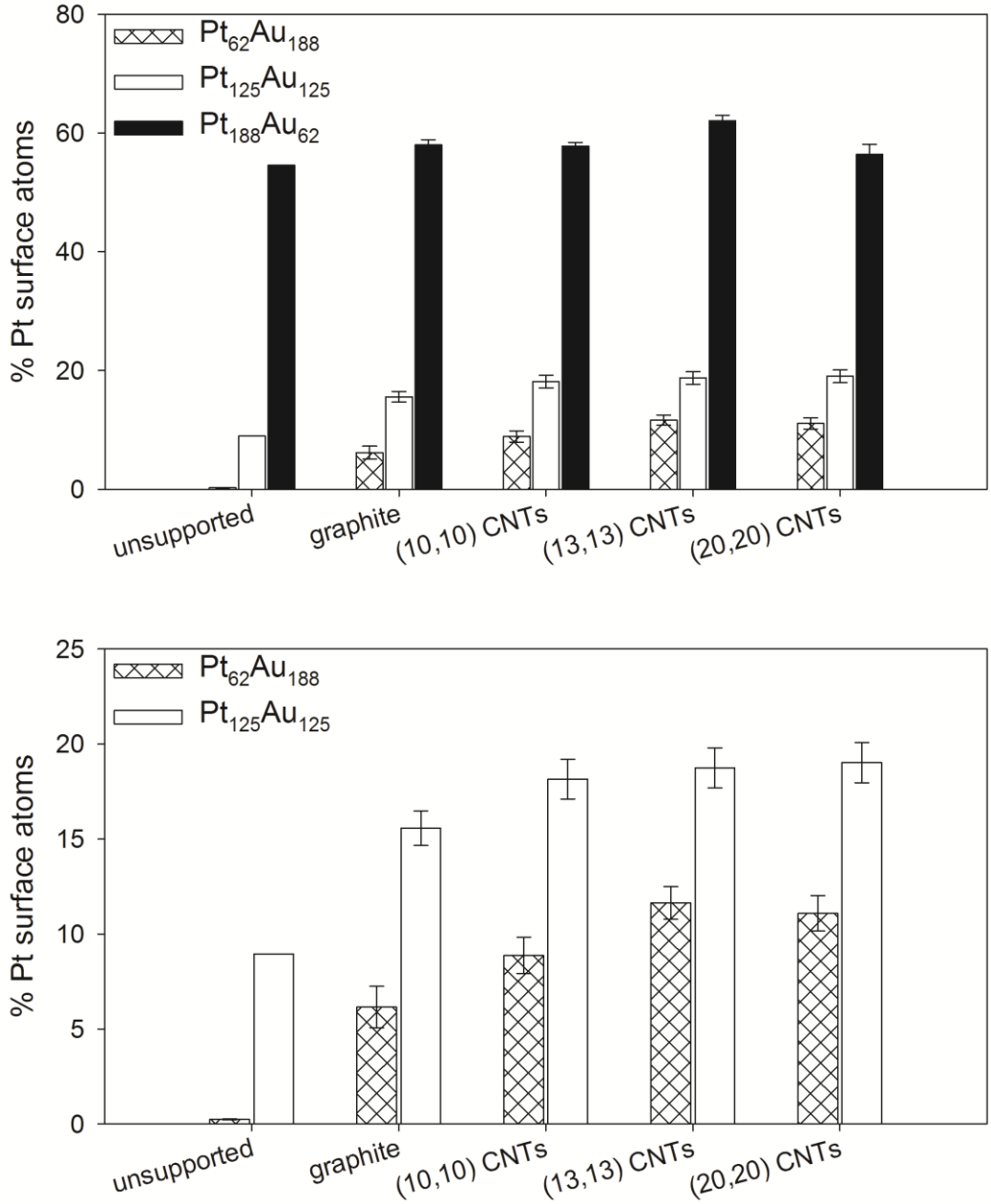

Figure 35: Average nanoparticle surface composition as a function of support. Three nanoparticle compositions are considered: $Pt_{62}Au_{188}$, $Pt_{125}Au_{125}$, and $Pt_{188}Au_{62}$. The bottom panel provides an expansion of the results shown in the top panel for $Pt_{62}Au_{188}$ and $Pt_{125}Au_{125}$ nanoparticles.

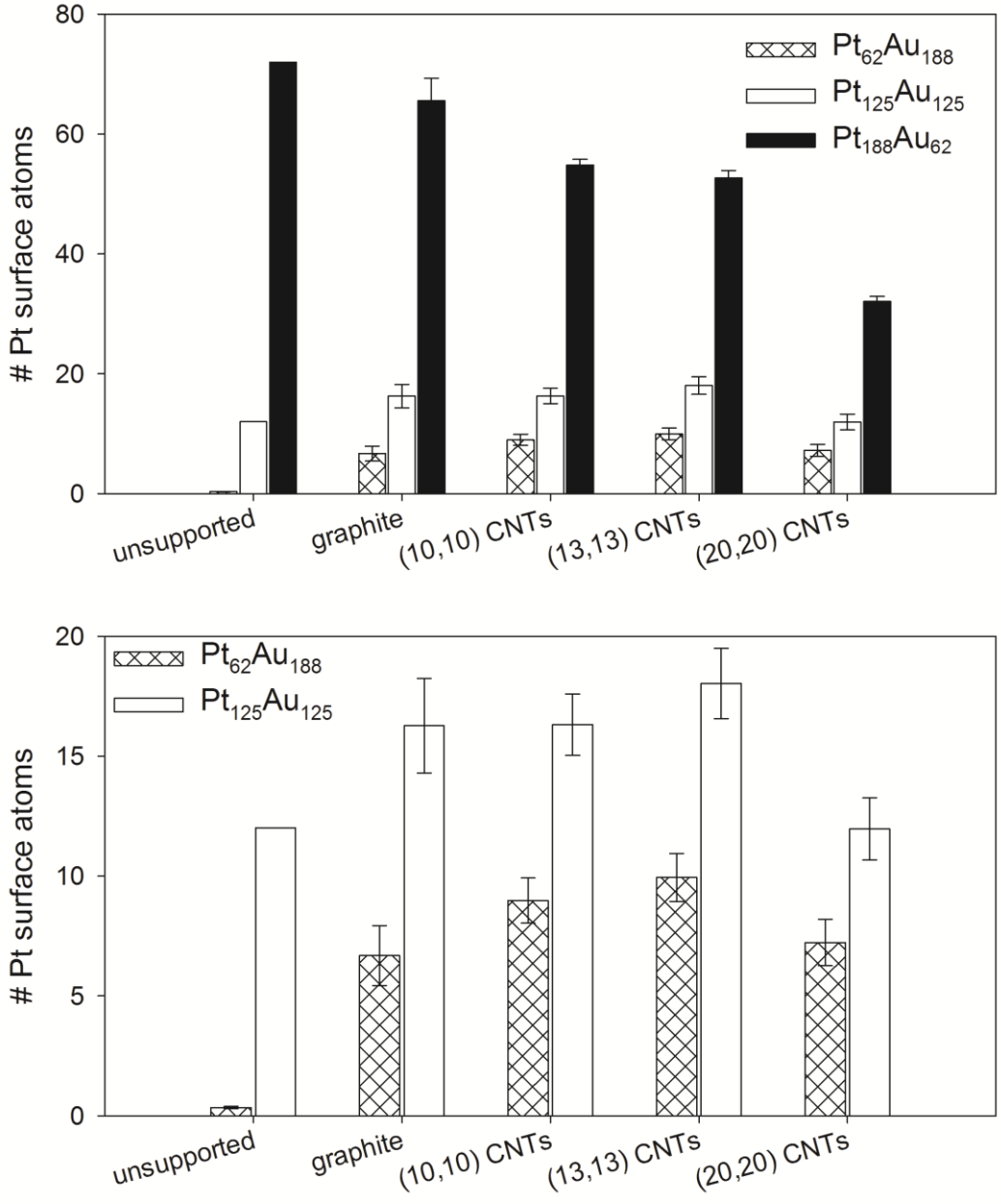

Figure 36: Average number of Pt atoms on the nanoparticle surface. Three nanoparticle compositions are considered: $Pt_{62}Au_{188}$, $Pt_{125}Au_{125}$, and $Pt_{188}Au_{62}$. The bottom panel provides an expansion of the results shown in the top panel for $Pt_{62}Au_{188}$ and $Pt_{125}Au_{125}$ nanoparticles.

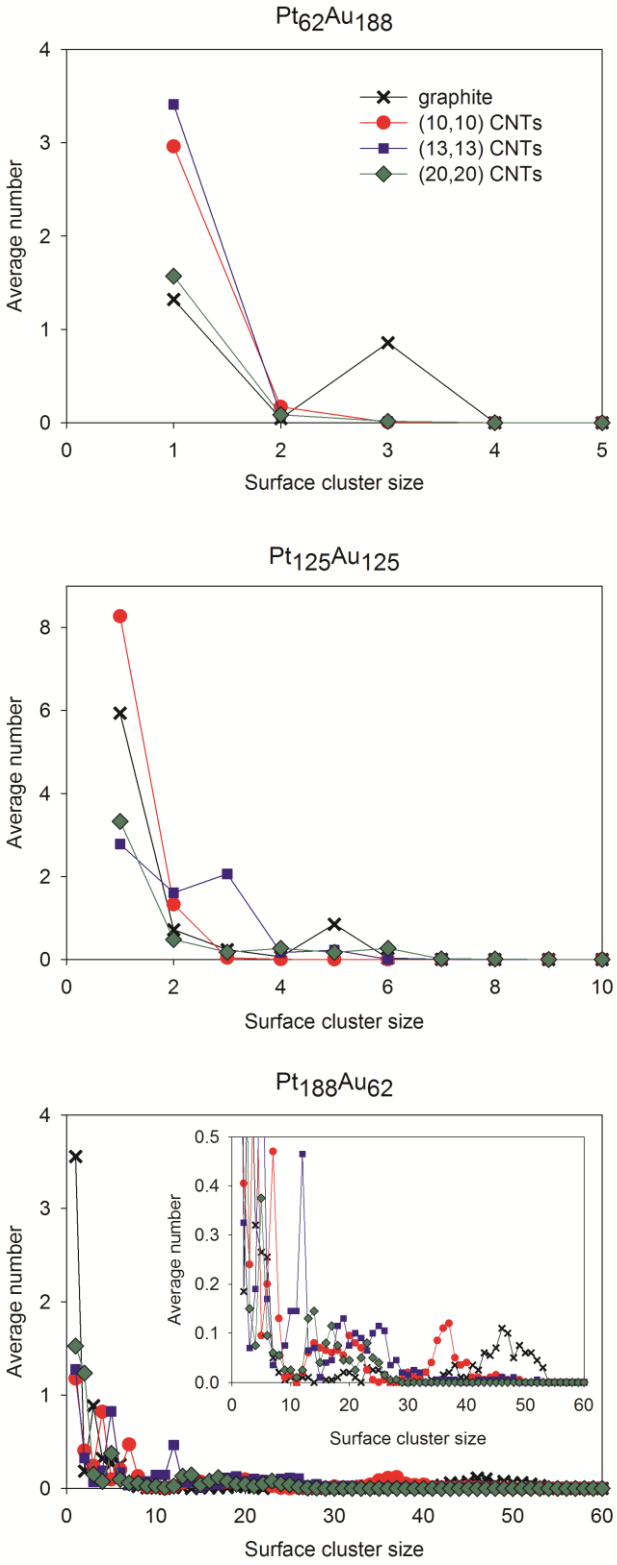

Figure 37: Average number of surface Pt clusters of given size, for $Pt_{62}Au_{188}$ (top), $Pt_{125}Au_{125}$ (middle), and $Pt_{188}Au_{62}$ (bottom). Error bars are not shown for clarity, but are ± ~0.2-0.3 for surface cluster sizes less than ~4, and ± ~0.01-0.02 for the larger cluster sizes found on $Pt_{188}Au_{62}$

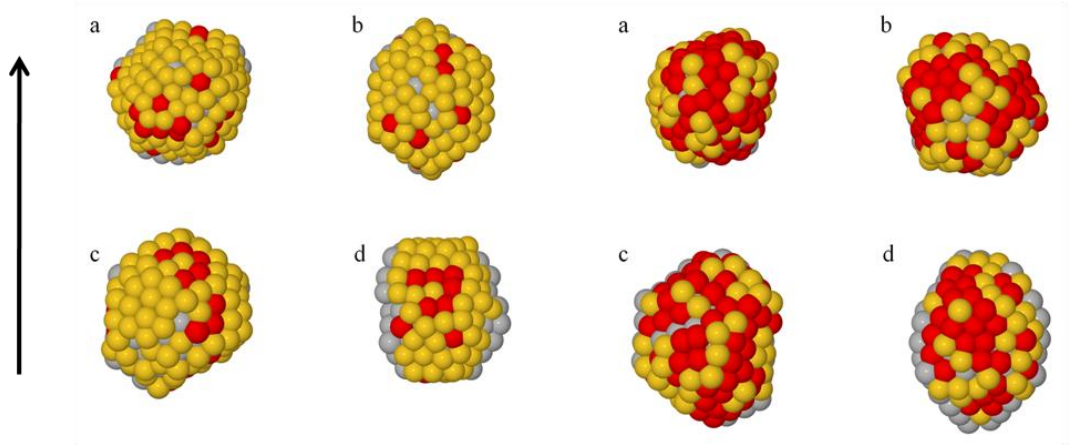

Figure 38: Snapshots of $Pt_{125}Au_{125}$ (left panel) and $Pt_{188}Au_{62}$ (right panel) on (a) a single graphite sheet, (b) (10,10) CNTs, (c) (13,13) CNTs, and (d) (20,20) CNTs. Pt and Au surface atoms are represented by red and yellow spheres, respectively. Metal atoms that are not on the surface are colored grey. Carbon atoms are not shown for clarity. The arrow indicates the direction of the CNT axis.

Even more important for catalytic applications is the coordination state of the Pt atoms on the nanoparticle surface. In Figure 37 we report the average number of Pt atom clusters found on the nanoparticle surface as a function of the number of Pt atoms in the cluster. Error bars are not shown for clarity, but are ± ~0.2-0.3 for surface cluster sizes less than ~4, and are much smaller (± ~0.01-0.02) for the larger cluster sizes found on $Pt_{188}Au_{62}$. A 'surface cluster' is defined as a group of surface Pt atoms that are neighbors with each other. For example, if atoms #1 and #2 are neighbors, atoms #2 and #3 are neighbors, and atoms #2 and #4 are neighbors, then atoms #1, 2, 3, and 4 are part of one surface cluster of size 4. On $Pt_{62}Au_{188}$ nanoparticles we predominantly see single-atom clusters when CNTs are supports. When graphite is the support clusters of 3 atoms are present. On $Pt_{125}Au_{125}$ nanoparticles there are no clusters larger than 6 Pt atoms, and the support influences the distribution of cluster sizes. For example, there are ~3 times as many clusters of 5 atoms when the support is graphite compared to

when the support is CNTs. The most pronounced differences are found for $Pt_{188}Au_{62}$ nanoparticles, in which case the support geometry appears to play a large role in the distribution of atoms on the nanoparticles' surface. When the support is graphite, there is a peak around cluster size 45-50, when the support is (10,10) CNTs the peak shifts to around 35-40 Pt atoms, and when the support is (13,13) CNTs there is a high concentration of surface clusters of 12 Pt atoms.

Snapshots of $Pt_{125}Au_{125}$ and $Pt_{188}Au_{62}$ nanoparticles, with the supporting carbon atoms not shown for clarity, are shown in Figure 38. These snapshots qualitatively confirm the results discussed above, and additionally indicate that the coordination state of the surface Pt atoms is affected by the support and by the nanoparticle composition. Specifically, $Pt_{125}Au_{125}$ shows chains of Pt and isolated Pt atoms on the surface, while the surfaces of the $Pt_{188}Au_{62}$ nanoparticles have larger clusters of Pt atoms, and fewer isolated Pt atoms.

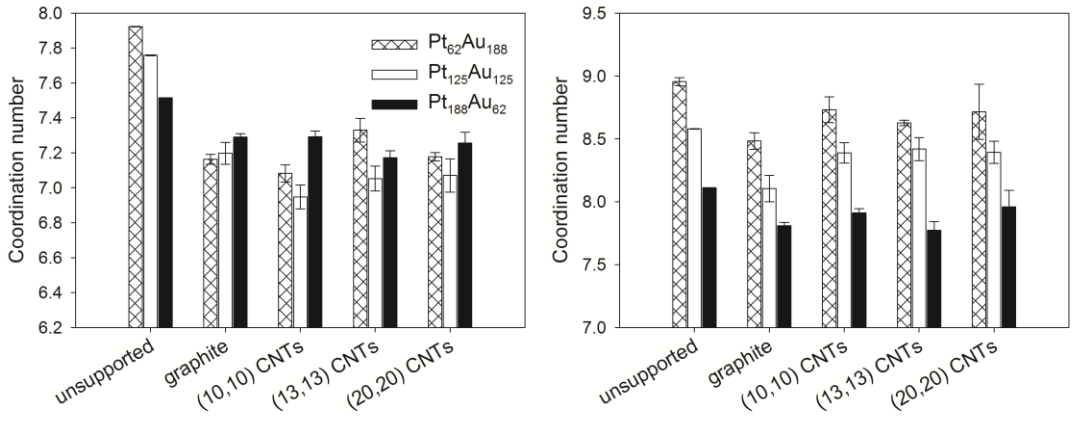

Figure 39: Average coordination number of all surface atoms (left) and Pt surface atoms (right) with any other atom.

To further examine the nanoparticles' surfaces we calculated the coordination numbers of the surface atoms. In Figure 39 we report the average coordination number

of all surface atoms (left panel) and of the Pt surface atoms (right panel). We point out that the data in Figure 39 correspond to the coordination with any other metal, either Au or Pt. The values reported are the averages of five simulations, and the error bars represent one standard deviation in each direction. For unsupported nanoparticles, the average coordination number decreases as the Pt content of the nanoparticle increases, both when all surface atoms and only Pt surface atoms are considered (left and right panel, respectively). When all surface atoms are considered, the average coordination number is lower when the nanoparticle is supported than when it is not, but there is no clear trend in the variations of the average coordination number as the support changes. When the average coordination number of the Pt surface atoms is calculated for a given composition the unsupported nanoparticles have the highest average coordination number, and nanoparticles on CNTs have higher average coordination number than those on graphite.

We have also calculated the Pt-Pt coordination number of Pt atoms on the surface; that is, for every Pt surface atom we count the number of nearest-neighbor Pt surface atoms. This is important to quantify because different sizes of groups of Pt atoms can catalyze different, sometimes competitive chemical reactions. The average number of surface Pt atoms having a given Pt-Pt coordination number is reported in Figure 40. A Pt-Pt coordination number of zero represents a single surface Pt atom surrounded by gold atoms. Surface Pt atoms with coordination number 1 are arranged in pairs surrounded by gold atoms, etc.

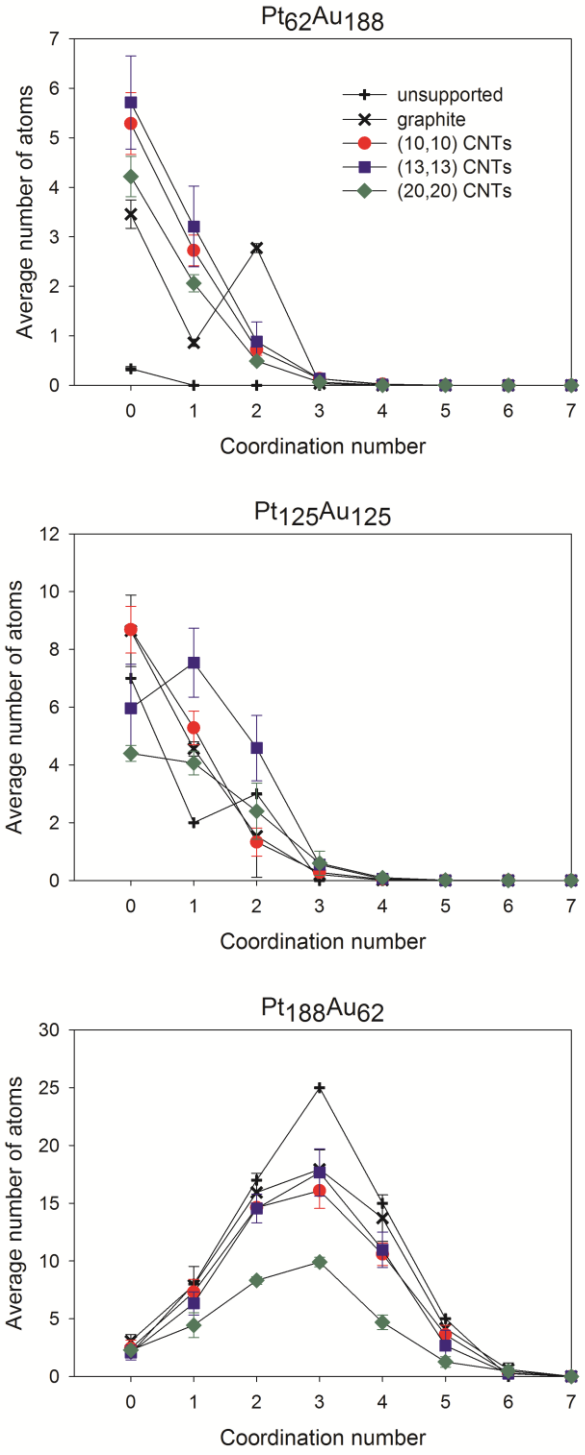

Figure 40: Average number of surface Pt atoms of a given coordination number with other Pt surface atoms. Results are shown for $Pt_{62}Au_{188}$ (top), $Pt_{125}Au_{125}$ (middle), and $Pt_{188}Au_{62}$ nanoparticles (bottom).

For $Pt_{62}Au_{188}$ the distribution of coordination numbers is similar on all three sizes of CNTs studied. For these nanoparticles most of the surface Pt atoms are surrounded only by Au atoms. On graphite, however, we find a larger number of Pt surface atoms with a Pt-Pt coordination number of 2, meaning that on graphite there is a larger concentration of islands of 3 Pt atoms on the nanoparticle surface. For $Pt_{125}Au_{125}$, the nanoparticle on (13,13) CNTs has the highest concentration of atoms with a coordination number of 1 (pairs of Pt atoms on the nanoparticle surface). For $Pt_{188}Au_{62}$, on all supports as well as for the unsupported nanoparticle, the distribution increases as the coordination number increases from 0 to 3, then decreases as the coordination number increases further. The distribution for coordination numbers 2, 3, and 4 is similar for nanoparticles on graphite, (10,10) CNTs and (13,13) CNTs, but is ~50% lower for nanoparticles on (20,20) CNTs. At the lower Pt compositions, $Pt_{62}Au_{188}$ and $Pt_{125}Au_{125}$, there are fewer Pt atoms on the surface (see Figure 36), so many of the Pt atoms are isolated or only have 1 or 2 surface Pt neighbors. As the coordination number increases the number of Pt atoms having that coordination number decreases. There are many more Pt atoms on the surface of $Pt_{188}Au_{62}$ nanoparticles, so a smaller percentage compared to $Pt_{62}Au_{188}$ and $Pt_{125}Au_{125}$ are isolated or have only 1 or 2 surface Pt neighbors. As the coordination number increases past 3 it is more difficult for an atom to have a large number of neighbors on the surface. This explains the maximum at coordination number 3 in the case of the $Pt_{188}Au_{62}$ nanoparticle. While experimental verification of our predictions is currently not available, the results in Figure 40 suggest that by appropriately tuning the nanoparticle composition and the support it is possible to tailor the catalytic activity of supported metal nanoparticles. Towards improving

selectivity, when single Pt atoms are required the best choice would be $Pt_{62}Au_{188}$ nanoparticles on (10,10) CNTs. When chains of Pt atoms or isolated Pt atoms are required, $Pt_{125}Au_{125}$ nanoparticles on (13,13) CNTs is the best choice. When small islands of Pt are required $Pt_{188}Au_{62}$ nanoparticles on (13,13) CNTs bundles are the recommended catalyst, etc.

Experimental validation of our predictions could be attempted by EXAFS, which yields the coordination number of surface atoms to be compared to our results; XPS, which yields the composition of a surface and may yield information about surface enrichment; and, more importantly, by spectroscopy analysis of CO adsorption. CO is expected to have different adsorption energies on metal atoms of different coordination, thus yielding different vibration frequencies. To enable the comparison between experimental and simulation data for vibration frequencies of adsorbed CO we are conducting *ab initio* density functional theory calculations.

All of the changes in the arrangement of the surface atoms discussed above are related to the change in the curvature of the support. As can be seen in the snapshots in Figure 38, nanoparticles on supports of different curvature have different shapes, a result which leads to different arrangements of atoms. To elucidate the molecular driving force for the observed results we calculated the adsorption energy and the 'deformation' energy for the nanoparticles on each of the supports. The adsorption energy is calculated by subtracting from the energy of the particle plus CNT bundle system the sum of the energy of the nanoparticle in vacuum and that of the CNT bundle without the nanoparticle. The deformation energy is the difference between the energy of the supported nanoparticle, deformed by the CNT bundle, and the energy of the

nanoparticle in vacuum. The results for the adsorption energy are reported in Figure 41 and indicate that the adsorption energy depends strongly on both the nanoparticle composition and the support geometry. The most favorable adsorption occurs on the (20,20) CNTs, likely because the nanoparticles are 'sandwiched' between neighboring CNTs, and consequently more atoms interact with carbon atoms (see snapshots in Figure 31). The results for the 'deformation' energy, reported in Figure 42, show that any of the supports considered here deform the nanoparticles. The deformation energy for the nanoparticles is largest on the (20,20) CNT bundle, where the adsorption energy is the most negative (see Figure 41). These results demonstrate that the support actively affects the properties of the supported nanoparticles, and therefore affects the distribution of metal atoms on the nanoparticle surface.

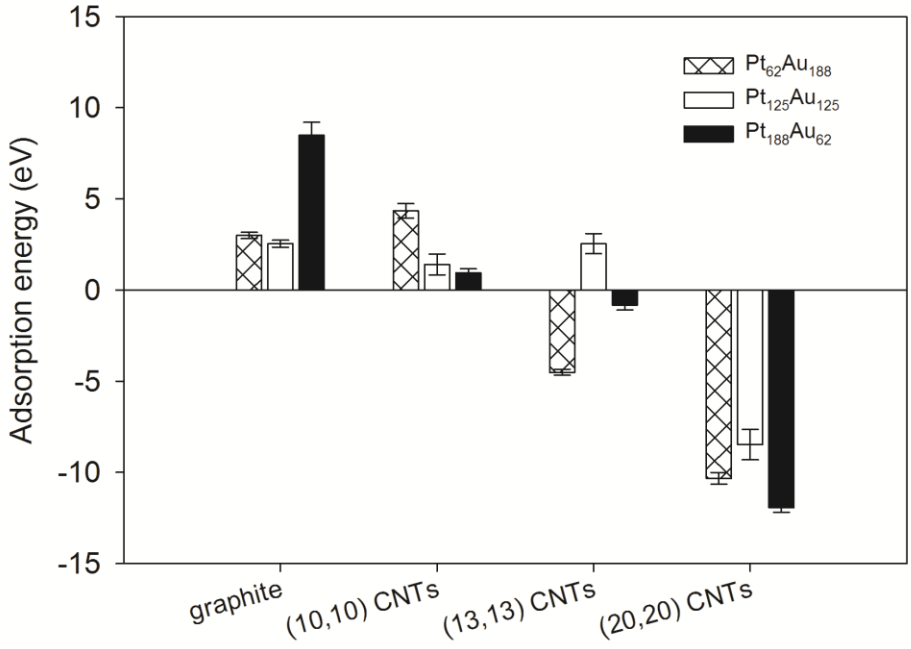

Figure 41: Nanoparticle adsorption energy on the four supports.

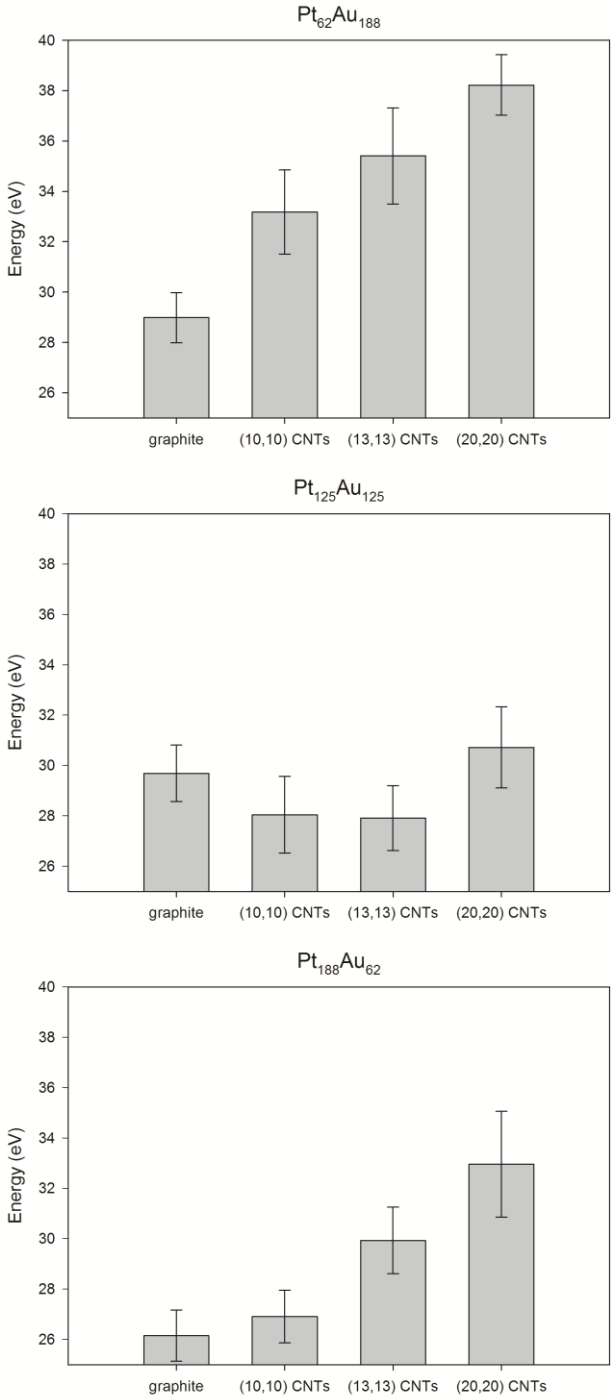

Figure 42: Nanoparticle deformation energy, calculated as the difference in energy between adsorbed and free nanoparticles.

5.5. Conclusions

We have conducted all-atom molecular dynamics simulations of bimetallic Pt-Au nanoparticles supported by graphite and bundles of carbon nanotubes of various radii. The embedded-atom method, Lennard-Jones potential, and the Tersoff potential were used to model metal-metal, metal-carbon, and carbon-carbon interactions, respectively. We have found that $Pt_{125}Au_{125}$ nanoparticles form a well-defined Pt-Au core-shell structure, and that the support slightly affects the atomic segregation within the nanoparticle. $Pt_{62}Au_{188}$ and $Pt_{188}Au_{62}$ nanoparticles form structures with a mixed Pt-Au core surrounded by an Au shell and a Pt core covered by a mixed Pt-Au shell, respectively. The support affects not only the number of Pt atoms on the nanoparticles surface, but also their arrangement. For $Pt_{188}Au_{62}$ nanoparticles the number of Pt atoms on the nanoparticles surface decreases when the nanoparticles are supported on bundles of carbon nanotubes. For $Pt_{62}Au_{188}$ nanoparticles the maximum number of Pt atoms is found when the nanoparticles is supported on bundles of (13,13) CNTs. For $Pt_{125}Pt_{125}$ nanoparticles the minimum number of Pt atoms on the surface is found when the nanoparticles are either unsupported or supported by bundles of (20,20) CNTs. Our calculations suggest that because the supports deform the supported nanoparticles, it determines changes in surface properties. Because of their importance in catalytic applications, we also studied the size of the clusters of Pt atoms on the nanoparticles' surface. Our results show that changing the support geometry alters the distribution of the sizes of the surface clusters, especially for $Pt_{188}Au_{62}$ nanoparticles. Because the coordination states of the surface atoms are also affected by the support, our results suggest that it should be possible to tailor the distribution of atoms in bimetallic

nanoparticles by careful selection of the nanoparticle composition and geometry of the support, with important implications in controlling the selectivity of catalysts.

6. CO Adsorption on Noble Metal Clusters: Local-Environment Effects

6.1. Abstract

We have used *ab initio* density functional theory calculations to study the adsorption of CO on clusters of 13 noble metal atoms. The cluster composition ranges from 100% Pt to 100% Au. Because our goal is to study the effect of local environment on CO adsorption, adsorption is only studied on the top atom site. This atom can be either Pt or Au, depending on the cluster considered. Results are analyzed in terms of CO adsorption energy, CO bond stretching frequency, geometry of the CO+cluster system, and HOMO-LUMO gaps. It is found that, as expected, the CO adsorption energy on Pt is >1 eV more favorable than that on Au. As expected, the cluster composition affects both adsorption energy and stretching frequency. Specifically, when CO adsorbs on Pt, increasing Au content decreases the adsorption energy. In contrast, when CO adsorbs on Au, increasing Pt content increases the adsorption energy. In general, higher adsorption energies lead to lower C-O stretching frequencies. Electronic-structure details (i.e., density of states) are discussed to explain the observed results, towards improving the interpretation of experimental spectroscopic data, and possibly designing new catalysts.

6.2. Introduction

Bimetallic catalysts are useful because of their versatility, such as the ability to tune their catalytic activity and selectivity by varying properties such as composition, particle size, and support.[36] In particular, Pt-Au catalysts have been shown to exhibit enhanced activity and selectivity in specific reactions when compared to monometallic catalysts. For example, Dimitratos et al.[137] showed that carbon-supported Pt-Au has higher catalytic activity for the oxidation of glycerol than carbon-supported Pt, and that the catalyst preparation method affects the selectivity. Selvarani et al.[157] determined that the optimum Pt:Au ratio for carbon-supported Pt-Au as a direct methanol fuel cell catalyst is 2:1, at which composition the catalyst delivers a peak power density 1.5 times that of pure Pt. Comotti et al.[138] found a turnover frequency of 60 h^{-1} for the oxidation of glucose over pure platinum, while a Pt-Au alloy with Au:Pt ratio of 2:1 yields a turnover frequency of 924 h^{-1}. The authors also found that, for 7 different Au:Pt ratios ranging from 4 to 0.25, the minimum and maximum turnover frequencies are 240 h^{-1} and 924 h^{-1}, observed for Au:Pt ratios of 1 and 2, respectively. It is likely that these results depend on the atomic arrangement on the surface of the bimetallic nanoparticles used as catalysts. Unfortunately, direct experimental visualization of the composition and structure of nanoparticle surfaces is at present problematic, especially at operating conditions. Techniques such as high-energy resonant x-ray diffraction can be used to probe the structure of bimetallic catalysts.[158] Molecular simulations could be useful to interpret such experiments, and also identify the local structure of supported mono- and bi-metallic nanoparticles.[59, 90, 136] For example, we have previously used molecular dynamics (MD) simulations to study the effect of composition and support geometry on

the properties of Pt-Au nanoparticles containing 250 atoms,[159] finding that it should be possible to tailor the distribution of atoms by manipulating nanoparticle composition and support geometry. This could lead to greater control of catalyst selectivity by maximizing the active sites on the nanoparticle surface that catalyze a certain reaction.

In order to link our previous MD results to experimentally verifiable measurements, we report here *ab initio* density functional theory (DFT) calculations for CO adsorption on Pt-Au clusters. CO is often employed as a probe molecule because its adsorption energy and C-O stretching frequency depend on the adsorption site, as can be observed experimentally via, e.g., Fourier transform infrared spectroscopy.[160] CO adsorption is also important in CO oxidation, which occurs in automobile catalytic converters,[161] in preferential CO oxidation (PROX reaction) in hydrogen feeds,[162] and CO hydrogenation, the critical step in Fischer-Tropsch processes.[163] DFT has been used to study adsorption of CO on metal surfaces, such as Pt(111),[46-49] on Pt(111) overlayers on other metals,[164-165] and on metal nanoparticles.[166] For example, Sadek and Wang[51] have investigated CO adsorption on Pt/Au clusters containing 2-4 atoms, while Song et al.[167] have reported adsorption energies for CO on Pt/Au clusters of up to 7 atoms. Sadek and Wang[18] found that CO vibrational frequency and CO bond length depend primarily on the adsorption site. Specifically, bridge site adsorption leads to CO bond vibrational frequencies in the range 1737-1927 cm^{-1} and bond lengths in the range 1.167-1.204Å, irrespectively of cluster composition. When adsorption occurs on the top site, vibrational frequencies are in the range 2000-2091 cm^{-1} and bond lengths are in the range 1.151-1.167Å. These results did not show a direct relationship between adsorption energy and CO bond vibrational frequency, although the authors found that

CO frequency decreases linearly with the decrease in CO bond length. Song et al.[19] found that CO adsorption on Pt atoms is more favorable than that on Au atoms. They found that cluster composition affects the adsorption energy, and in particular they found that when CO adsorbs on Au atoms the most favorable cluster composition is that with 25% Pt. They also found that, for a 6-atom cluster, CO adsorption energy increases with Pt composition. However, they did not report data for either CO bond stretching frequency or CO bond length. A detailed understanding of how the cluster composition affects the observed results remains elusive.

Pedersen et al.[168] have performed experiments involving Pt overlayers on Au(111). Among their findings was the fact that CO adsorption was weaker on single Pt atoms in the Au(111) surface than on pure Pt(111) surfaces. They also found that a monolayer of Pt on Au(111) exhibits stronger CO adsorption than pure Pt(111). Nilekar et al.[165] showed via DFT calculations that CO adsorption on Pt(111) overlayers on Ru is much weaker than on pure Pt(111) surfaces, and also that the monolayer coverage on the former material is much less than on the latter. Combining DFT results with experiments, they demonstrated that these effects lead to potent catalysts for the PROX reaction, even when conducted at mild conditions.[164] Habrioux et al.[169] found an increase in CO-Pt binding energy with increasing gold content in nanoparticles with diameters of ~4-10 nm. Irissou et al.[170] synthesized Pt-Au films that also showed an increase in CO adsorption energy with increasing Au content. These experimental findings, in agreement with DFT calculations conducted on flat surfaces, appear to disagree with the DFT results of Song et al.[167] discussed above, which were obtained for metal clusters of <10 atoms. This discrepancy suggests that size effects can play a very

important role in the properties of metal nanoparticles and clusters. For example, Pt clusters containing 8-10 atoms have been shown to have a 40-100 times greater activity for the oxidative dehydrogenation of propane than a Pt-coated monolith.[171] This brief literature survey suggests the need of better understanding the catalytic properties of metal clusters of various sizes.

In this manuscript we investigate CO adsorption on Pt and Au atoms in Pt-Au clusters of 13 atoms. Our goal is to quantify how the local environment around the metal atom on which adsorption occurs affects the properties of the adsorbed CO. We study how the CO adsorption energy, C-O stretching frequency, and cluster morphology depend on the cluster composition. All our calculations are conducted using Pt-Au clusters containing 13 atoms. While smaller than nanoparticles used in most industrial and academic applications of catalysis, including those considered in our MD simulations,[74, 89, 148, 159] these clusters could serve as a useful model for atoms with low coordination numbers, such as those on corners and edges of nanoparticles, which are expected to have high catalytic activity. We found that C-O stretching frequency and CO adsorption energy are inversely related, with higher adsorption energies leading to lower C-O stretching frequencies. To explain the local environmental effects on the properties of adsorbed CO we studied the electronic properties of the clusters, calculating the charges of relevant atoms, energy differences between highest occupied and lowest unoccupied molecular orbitals (HOMO-LUMO gaps), and the density of states for the various clusters.

The remainder of this chapter is organized as follows. First we describe the details of our calculations. Next we discuss results for cluster geometries, CO

adsorption energy, and C-O stretching frequency. To explain the observed trends in adsorption energy and frequency, we characterize the electronic structure of the clusters by examining atomic charges, HOMO-LUMO gaps, and density of states.

6.3. Computational Details

Ab initio density functional theory (DFT) calculations were performed using Gaussian03.[172] We performed calculations using six different exchange-correlation functionals: (1) the Beck three-parameter hybrid functional[173] with the non-local correlation functional of Lee, Yang, and Parr[174] and the local correlation functional of Vosko, Wilk, and Nusair[175] (B3LYP);[176] (2) the functional of (1) but with the non-local correlation functional of Perdew[177] (B3P86); (3) Becke's 1988 exchange functional[178] with Perdew and Wang's 1991 gradient-corrected correlation functional[179-180] (BPW91); (4) the exchange and correlation of Perdew and Wang's 1991 functional (PW91); (5) the functional of Perdew, Burke, and Ernzerhof[181] (PBE); and (6) the PBE functional as rendered into a hybrid by Adamo[182] (known as PBE0, but referred to as PBE1PBE in Gaussian). Quantitative comparisons between the results are given as Appendix to the text. All the results reported in this chapter were obtained using the B3LYP functional, which was chosen because of its agreement with experimental results and its previous use in similar calculations.[49, 183-186]

The LANL2DZ effective core potential and basis set[187] was used to describe metal atoms, while the 6-311G* basis set was used to describe C and O atoms. Calculations for an isolated CO molecule match the experimental bond length of 1.13

Å.[188] The calculated C-O stretching frequency of 2212 cm^{-1} overestimates the experimental value of 2143 cm^{-1} by ~3%.

Clusters containing 13 metal atoms were used in our calculations. We studied both Au_{13} and Pt_{13}. We generated other clusters by replacing one atom in Au_{13} (Pt_{13}) with Pt (Au). When the replaced atom is in the center of the cluster, the cluster name is designated by "-c". The atom on which CO is adsorbed is referred to as the "top" atom. When that atom is replaced the cluster is designated as "-t". By this naming convention, the clusters studied here are designated as Au_{13}, $Au_{12}Pt_1$-c, $Pt_{12}Au_1$-t, $Au_{12}Pt_1$-t, $Au_{12}Pt_1$-c, and Pt_{13} (see Figure 43).

Adsorption energies are calculated by subtracting the sum of the energies of isolated CO and the metal cluster from the energy of the metal cluster with adsorbed CO. More negative values indicate stronger adsorption. Density of states calculations were performed using the program GaussSum 2.2.[189] Atomic charges were calculated by the Natural Bond Orbital analysis (NBO), using the NBO version 3 program contained in Gaussian.[190-191]

6.4. Results and Discussion

6.4.1. Cluster Geometry

Optimized geometries of the six clusters studied with and without adsorbed CO, with no symmetry restraints, are shown in Figure 43. In three of the clusters (Au_{13}, $Au_{12}Pt_1$-c, and $Pt_{12}Au_1$-t) CO is adsorbed on Au, and in the other three ($Au_{12}Pt_1$-t, $Pt_{12}Au_1$-c, and Pt_{13}) CO is adsorbed on Pt. Our previous MD simulations, conducted at 700 K for Pt-Au bimetallic nanoparticles of 250 atoms,[159] indicated, in agreement with

a number of theoretical[125, 128, 149-150] and experimental[151-154] results, that Au tends to segregate to the outer shell of Pt-Au bimetallic nanoparticles. However, individual Pt atoms can still be found at the surface of such bimetallic nanoparticles.[155-156] It should also be pointed out that experimental techniques are available to prepare Pt adlayers on gold, even though such structures are not stable at high temperatures.[164]

In some of the energy-minimized structures for the 13-atom clusters in Figure 43 (e.g. in the $Pt_{12}Au_1$-c cluster) Au is located in the cluster interior. It should be noted that DFT calculations are effectively conducted at 0 K, and that the energy minimization procedure does not guarantee that the global minimum energy structure of the clusters has been reached. Rather, the energy minimization routine finds a local minimum on the potential energy surfaces. In fact, $Pt_{12}Au_1$-t is 2.46 eV more stable than $Pt_{12}Au_1$-c prior to CO adsorption. With CO adsorbed, the energy difference decreases to 1.3 eV. Prior to adsorption, $Au_{12}Pt_1$-c is 1.15 eV more stable than $Au_{12}Pt_1$-t. Upon CO adsorption, the complex CO+$Au_{12}Pt_1$-t is more stable than CO+$Au_{12}Pt_1$-c by 0.25 eV, due to the strong adsorption energy of CO on Pt. This change of the energetic stability of $Au_{12}Pt_1$-t vs. $Au_{12}Pt_1$-c upon CO adsorption may be related to changes in the morphology of heterogeneous catalysts under reaction conditions, a topic not further discussed here.

The energy-minimized clusters of Figure 43 are used to study the adsorption of CO and therefore assess the effect of local environment on adsorption energy and vibrational frequency, quantities that are experimentally observable. By comparing the structures of the metal clusters before and after CO adsorption (top and bottom panels in Figure 43, respectively), we observe that CO adsorption results in minimal changes in

the geometries of the clusters, except in the case of $Pt_{12}Au_1$-t, which will be discussed below.

Distances between the C atom of CO and the metal atom on which it is adsorbed, as well as those between C and O atoms in adsorbed CO are reported in Table 4. When CO is adsorbed on Au, the C-metal distance ranges from 1.948 Å, on $Pt_{12}Au_1$-t, to 1.993 Å, on Au_{13}. When CO is adsorbed on Pt, the C-metal distance is ~0.1-0.15 Å shorter, and ranges from 1.807 Å, on $Pt_{12}Au_1$-c, to 1.852 Å, on $Au_{12}Pt_1$-t. Comparing the C-metal to the C-O distance we find, for CO adsorbed on Pt, that the shorter the C-metal distance is, the longer the C-O bond becomes. The C-O distance ranges from 1.147 Å, on $Au_{12}Pt_1$-t, to 1.152 Å, on $Pt_{12}Au_1$-c. The Pt-C distance is shortest for CO on $Pt_{12}Au_1$-c and not for CO on Pt_{13}, as might have been expected. For CO adsorbed on Au the C-O distance is 1.133 Å for all three systems studied. Based on these results, one could speculate that adsorption on Pt changes the CO electronic structure significantly, while adsorption on Au does not perturb to a large extent the CO electronic structure.

Table 4: Bond lengths in CO+cluster systems.

Cluster	C-metal distance (Å)	C-O distance (Å)
Au_{13}	1.993	1.133
$Au_{12}Pt_1$-c	1.984	1.133
$Pt_{12}Au_1$-t	1.948	1.133
$Au_{12}Pt_1$-t	1.852	1.147
$Pt_{12}Au_1$-c	1.807	1.152
Pt_{13}	1.834	1.149
gas phase CO	-	1.13

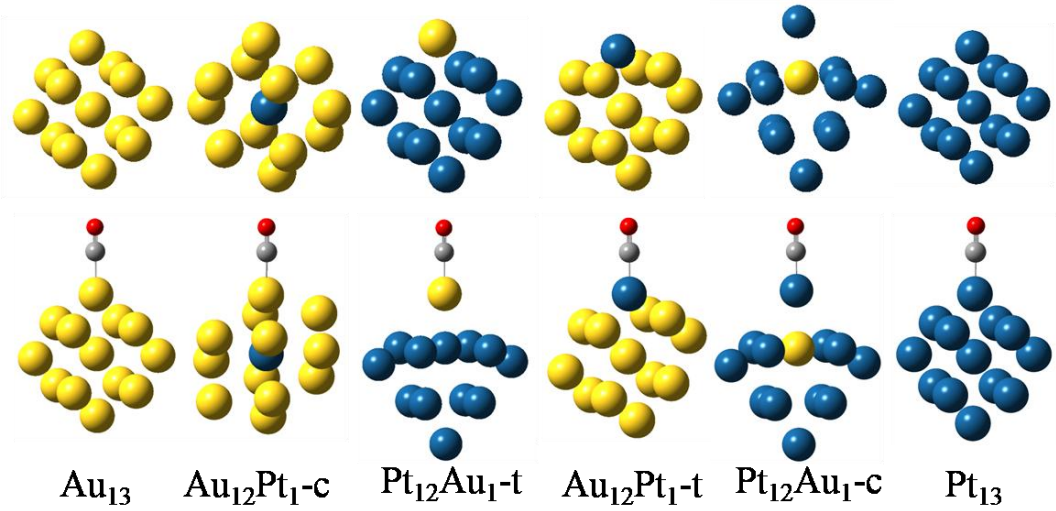

Figure 43: Top: Optimized geometries of 13-atom metal clusters. Bottom: Optimized geometries of 13-atom clusters with adsorbed CO. Pt, Au, C, and O atoms are represented by blue, yellow, grey and red spheres, respectively.

6.4.2. Adsorption Energy

The adsorption energy for CO on the six metal clusters is reported in Figure 44. The adsorption is the weakest on Au_{13}, -0.66 eV, and it is the strongest on Pt_{13}, -2.40 eV.

Experiments for CO adsorption on alumina-supported Pt nanoparticles give an adsorption energy of -2.13 eV.[192] Given the differences between the systems studied (supported nanoparticles in Ref. [192] versus clusters in vacuum here) and the inherent uncertainties in both experiment and DFT calculations, our DFT-calculated result seems to agree reasonably well with experiments. Experimental CO adsorption energies on TiO_2-supported Au nanoparticles with size of 1.8-3.1 nm were found to range from 0.54 to 0.79 eV,[193] also in reasonable agreement with our data. Additional validation could be attained by comparing our results to theoretical literature reports. Previous DFT

calculations yield adsorption energies of -2.86 eV[51] for CO on Pt_4 and -2.73 eV[194] for CO on Pt_6, in reasonable agreement with our findings.

Not surprisingly, our calculations show adsorption energies >1 eV stronger (more negative) when CO adsorbs on Pt than when it adsorbs on Au.

More importantly for the scope of the present paper, however, is that the results show that changing the composition of the cluster has a quantifiable effect on the adsorption energy even when CO adsorbs on the same metal atom (i.e., Au or Pt). When CO adsorbs on Au, increasing the Pt content of the cluster increases the adsorption energy. When the central atom of Au_{13} is replaced by Pt, the adsorption energy increases (i.e., becomes more negative) by 0.07 eV; when CO adsorbs on a single Au atom in an otherwise Pt cluster ($Pt_{12}Au_1$-t), the adsorption energy is 0.40 eV higher than on Au_{13}. In contrast, when CO adsorbs on the Pt top atom, increasing the Au content within the cluster decreases the adsorption energy. When the central atom of Pt_{13} is replaced by Au the adsorption energy becomes less negative by 0.12 eV; the adsorption energy on $Au_{12}Pt_1$-t is 0.27 eV lower than on Pt_{13}. Pedersen et al.[168] showed experimentally that the CO desorption temperature is lower on single Pt atoms in Au(111) than for clean Pt(111), analogous to our result of lower CO adsorption energy on $Au_{12}Pt_1$-t than Pt_{13}. To highlight the relevance of our calculations, we point out that changes in the CO adsorption energy on transition metal catalysts of the order of ~0.5 eV have led to the design of effective catalysts that promote the PROX reaction at mild conditions.[164-165] We notice that, in general, as the adsorption energy increases (becomes more negative) the C- metal distance decreases and the C-O distance increases (see Table 4). Some deviations from this general trend are, however, evident

from our results (compare for example the results obtained on Pt_{13} vs. those on $Pt_{12}Au_1$-c).

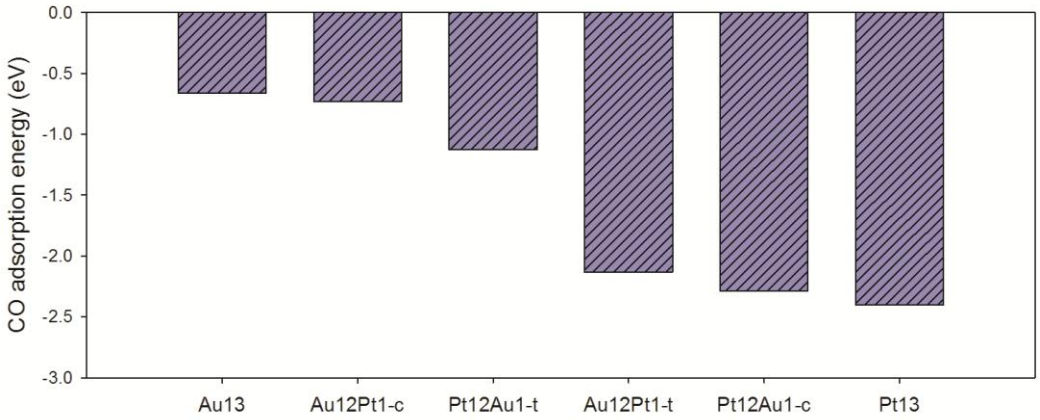

Figure 44: CO adsorption energy on 13-atom metal clusters. For identification of the clusters see Figure 43.

6.4.3. C-O Stretching Frequency

Values for the C-O stretching frequency are reported in Figure 45. Although we could rescale our CO vibrational frequency results to account for differences from experimental values in the gas phase, we prefer to report the raw data. The experimental value[192] for CO adsorbed on alumina-supported Pt nanoparticles is 2075 cm^{-1}. Gruene *et al.*[195] experimentally measured single-molecule CO adsorption on group 10 transition metal clusters and reported a value of ~2070 cm^{-1} for CO on Pt_{13}. These results are comparable to our calculated value of 2091 cm^{-1} for CO on Pt_{13}, especially when we recall our calculations overestimate the vibrational frequency for isolated CO (2212 cm^{-1} vs 2143 cm^{-1} found experimentally). Meier and Goodman[193] found experimental frequencies of ~2123 cm^{-1} for CO adsorbed on Au nanoparticles with sizes of 1.8-3.1

nm, also in reasonable agreement with our calculations. As expected from the Blyholder model,[196] because of differences in adsorption energies, the C-O stretching frequency is larger for CO adsorbed on Au, and lower for CO adsorbed on Pt.

Our results show that the local environment affects the C-O stretching frequency. In the case of CO adsorbed on Pt, increasing the Au content of the cluster slightly increases the C-O stretching frequency. Replacing the central atom of Pt_{13} with Au results in a frequency of 2093 cm^{-1}, while the frequency for CO on $Au_{12}Pt_1$-t is 2100 cm^{-1}. Frequencies for CO adsorbed on Au are ~70-80 cm^{-1} higher than those for CO on Pt.

According to the Blyholder model[196] the C-O stretching frequency is expected to increase as the adsorption energy decreases (the decreased back-donation of electrons results in weaker adsorption, leading to a stronger C-O bond). Consequently, the vibration frequencies should be highest on Au_{13}, and progressively lower for $Au_{12}Pt_1$-c and $Pt_{12}Au_1$-t. This trend is generally obeyed by our data, as can be seen from Figure 45. Our results show the highest stretching frequency for CO on $Pt_{12}Au_1$-t.

The somewhat peculiar behavior of the $Pt_{12}Au_1$-t cluster can be explained by examining the optimized geometries shown in Figure 43. In the $Pt_{12}Au_1$-t cluster, the Au atom is pulled away from the Pt ones, leaving the former isolated at the top of the cluster. This geometrical effect changes the electronic properties of the Au atom, resulting in different CO adsorption behavior compared to that on the 'top' Au atoms in Au_{13} and $Au_{12}Pt_1$-c. Calculations for CO adsorption on a single Au atom (not discussed in detail here for sake of brevity) support this hypothesis, yielding a C-O stretching

frequency of 2180 cm^{-1}, very close to the frequency of 2183 cm^{-1} found for CO on $Pt_{12}Au_1$-t.

In Figure 46 we report the relationship between C-O stretching frequency and CO adsorption energy. The result for the high frequency observed on the $Pt_{12}Au_1$-t cluster is included as a square symbol to differentiate it from the other data points. As can be seen from Figure 46, our results show that as the CO stretching frequency decreases the adsorption energy becomes more negative. It is important to reiterate that for all cases considered in Figure 46 CO adsorbs on top of either Pt or Au, and that changes in both adsorption energy and vibrational frequency are due to changes in the cluster composition (i.e., local environment). Changes in the adsorption site (e.g., adsorption between adjacent metal atoms) have not been considered.

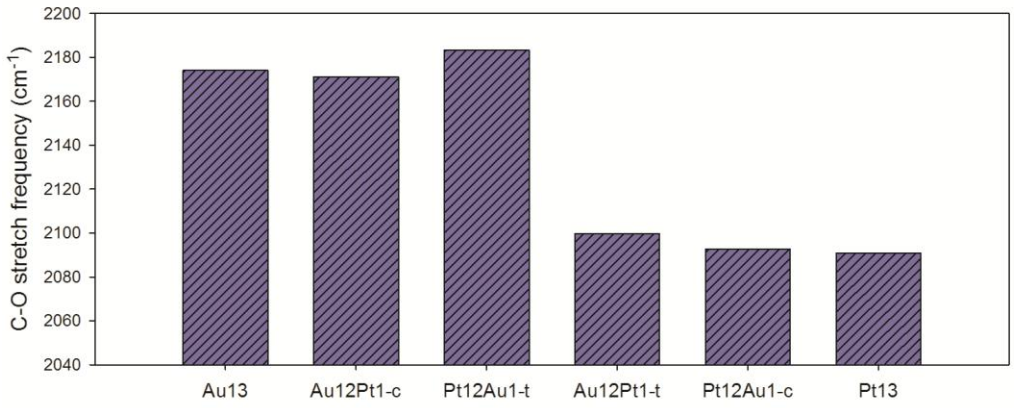

Figure 45: C-O stretching frequency for CO adsorbed on 13-atom metal clusters.

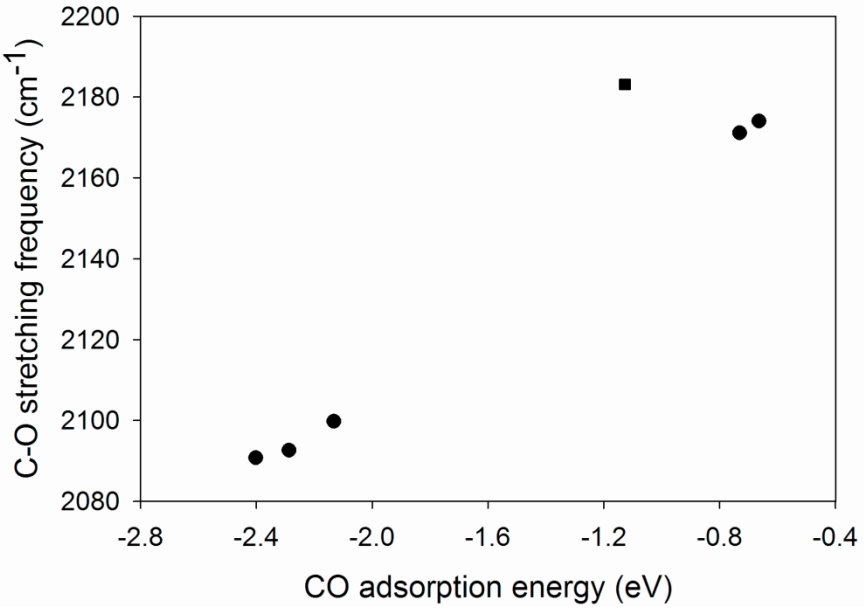

Figure 46: C-O stretching frequency vs CO adsorption energy, data from Figure 44 and Figure 45. The square represents results obtained for CO adsorption on Pt12Au1-t.

6.4.4. Atomic Charges

To attempt rationalizing why CO adsorption energy changes for clusters of different compositions, and to determine if there is a correlation between atomic charges in the clusters and the adsorption energy, we calculated the atomic charges on various atoms. There is no consensus in the literature on how to rigorously calculate atomic charges.[197] All currently available methods, which include the Mulliken population analysis,[198] the electrostatic potential (ESP),[199] and the Natural Bond Orbital (NBO) methods[190-191] involve approximations. We have used the NBO method, as it has been found to be in good agreement with Lewis structure concepts and give accurate results for bond hybridization and polarization.[200]

Reported in Figure 47 are the charges for carbon and oxygen atoms when CO is adsorbed on the clusters. Additionally, we report the charges of the 'top' metal atom,

both for bare clusters (no adsorbed CO) and for the clusters with adsorbed CO. In the left panel of Figure 47 the first three clusters considered on the *x*-axis have CO adsorbed on Au, while in the last three CO is adsorbed on Pt.

Comparing the charge on the carbon and oxygen atoms of CO prior to, and after adsorption (left panel), it might be possible to differentiate among different mechanisms of CO adsorption on the various clusters. However, the results do not show significant changes when the cluster composition is altered. We can only report that when CO is adsorbed on Pt, the charge of the oxygen atom is slightly more negative than when CO adsorbs on Au, possibly a consequence of electronic back donation.

For systems with CO adsorbed on Pt, the adsorption energy is reported as a function of the charge on the 'top' metal atom prior to CO adsorption in the right panel of Figure 47. As the metal cluster composition changes, the charge in the top metal atom also changes. As the charge on the top metal atom prior to CO adsorption becomes more positive, the CO adsorption energy increases, going from -2.13 eV when the charge is -0.20e, to -2.40 eV when the charge is 0.15e. This could indicate that a lower electron density on the top Pt atom results in more electron donation from the carbon atom of adsorbing CO, yielding stronger adsorption. There is no corresponding trend when adsorption occurs on Au, suggesting that the electronic phenomena leading to CO adsorption differ when CO adsorbs on Pt or on Au.

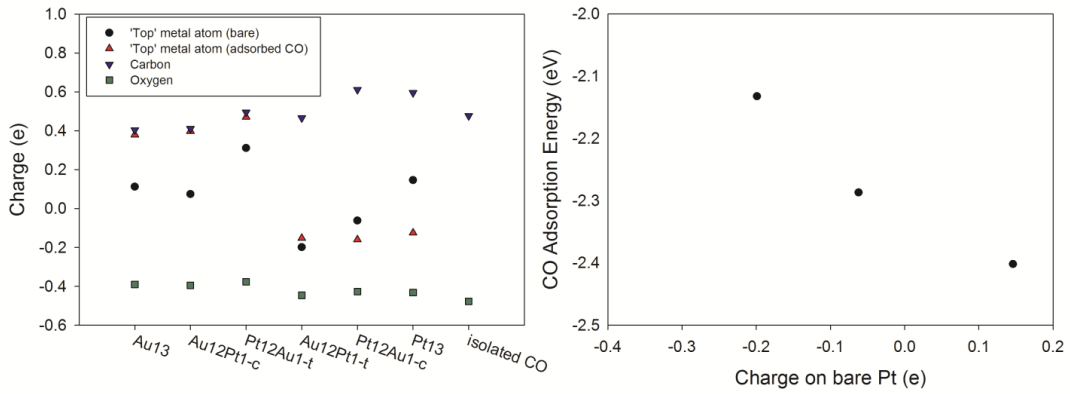

Figure 47: Left: Charges for 'top' metal atoms on bare metal clusters, 'top' metal atoms on clusters with adsorbed CO, and for C and O atoms of adsorbed CO. Right: CO adsorption energy as a function of charge of 'top' Pt atoms. All charges are calculated using the Natural Bond Orbital method.[190-191]

6.4.5. HOMO-LUMO Gaps

In order to characterize the electronic structure of the clusters considered, we calculated the difference in energy between the highest occupied and lowest unoccupied molecular orbitals (HOMO-LUMO gaps). From a catalytic perspective, systems with smaller HOMO-LUMO gaps tend to be more reactive.[201-202] In Table 5 we report the HOMO-LUMO gaps for the clusters studied here, both with and without adsorbed CO. The results obtained for the HOMO-LUMO gap for the metal clusters before CO adsorption are identified as 'bare' clusters. For these, we find that Au_{13} and Pt_{13} have the highest and lowest HOMO-LUMO gaps, respectively. In general, correlating the results in Table 5 to data for CO adsorption energy, we observe that a lower HOMO-LUMO gap for the bare clusters results in higher CO adsorption energy (see Figure 48). However, our data suggest that the correlation just described holds only when CO adsorbs on the same type of metal (i.e., either Pt or Au). Further, because the trend just documented is not obeyed for the $Au_{12}Pt_1$-c cluster (which has the third-lowest HOMO-

LUMO gap, while CO adsorption on $Au_{12}Pt_1$-c shows the second-lowest energy of the systems considered) it appears that CO adsorption on Pt is more easily explained than that on Au. For the clusters with adsorbed CO, Pt_{13} again has the lowest HOMO-LUMO gap, but $Au_{12}Pt_1$-t has the highest.

To visualize the effect of cluster composition on the overall electronic structure, we report in Figure 49 the highest occupied molecular orbitals for the bare clusters. Visualizations of both highest occupied and lowest unoccupied molecular orbitals for each cluster considered here, with and without adsorbed CO, are reported in the Appendix.

Table 5: HOMO-LUMO gap calculations for 13-atom clusters in vacuum (bare) or with adsorbed CO.

Cluster	**HOMO-LUMO gap, bare cluster (eV)**	**HOMO-LUMO gap, CO+cluster (eV)**
Au_{13}	1.497	1.252
$Au_{12}Pt_1$-c	1.279	1.170
$Pt_{12}Au_1$-t	1.361	0.844
$Au_{12}Pt_1$-t	1.306	1.361
$Pt_{12}Au_1$-c	1.088	0.844
Pt_{13}	0.925	0.762

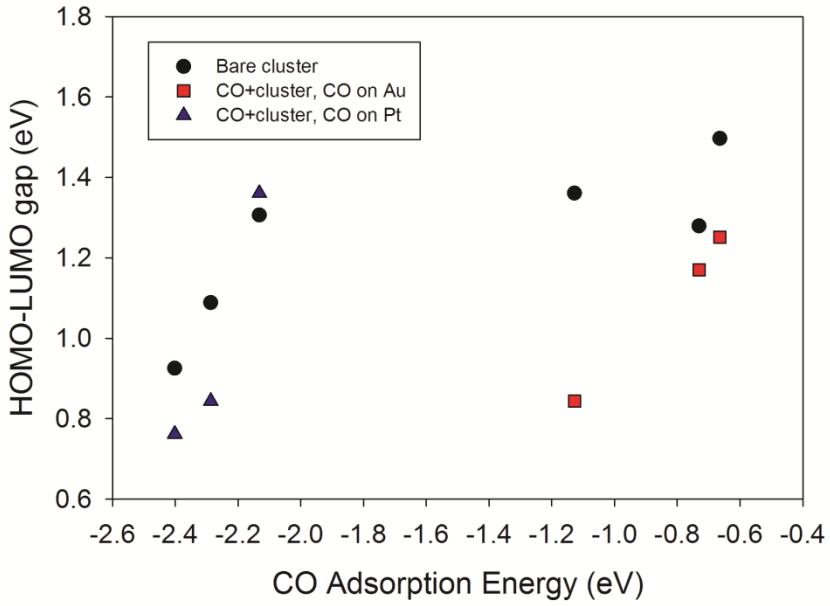

Figure 48: HOMO-LUMO gaps as a function of CO adsorption energy.

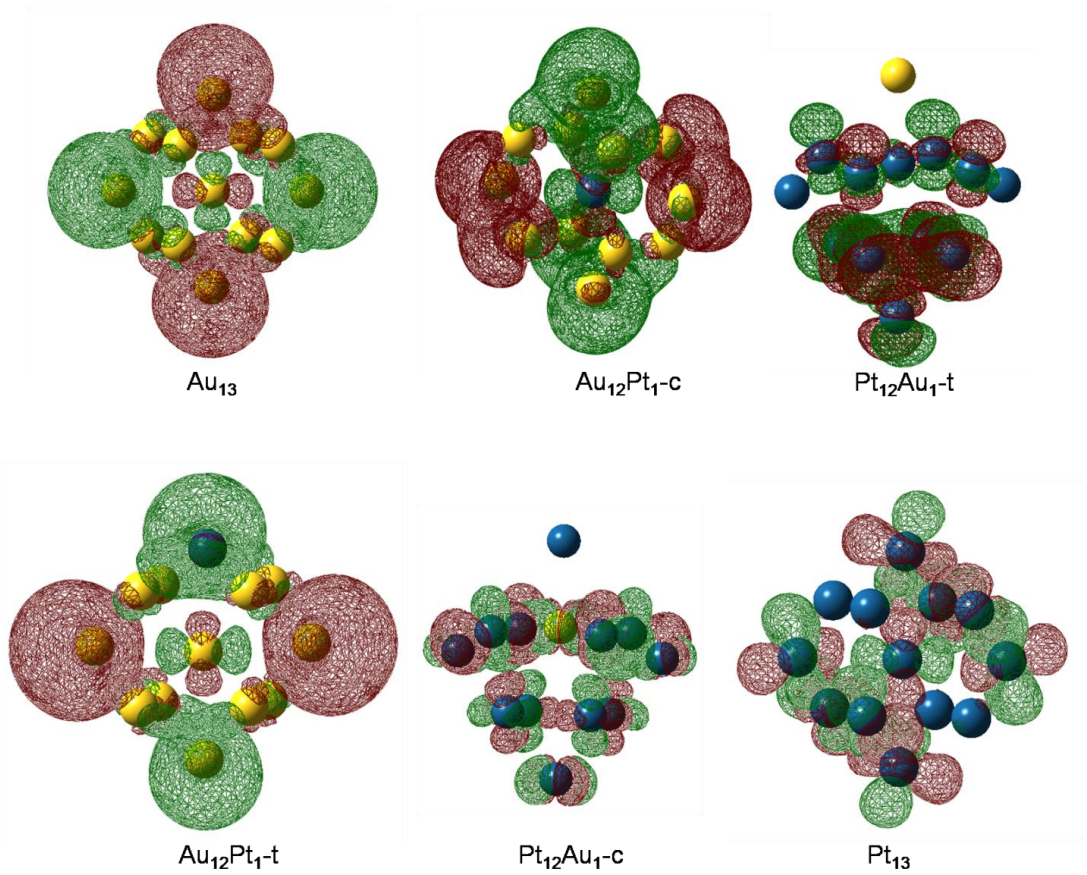

Figure 49: Highest occupied molecular orbitals (HOMOs) for bare metal clusters. Pt and Au atoms are represented by blue and yellow spheres, respectively. Red and green represent positive and negative phases, respectively.

6.4.6. Density of States

In order to gain a deeper insight of the electronic mechanisms that play a role in the adsorption properties of CO we analyzed the density of states (DOS) projected on the metal atom on which CO adsorbs, as well as on the C and O atoms of CO. Differences in densities of states can indicate changes in reactivity. It has been shown[168, 203-205] that the center of the d-band relative to the Fermi energy plays a role in the reactivity of transition metals in different environments. For a variety of metals and adsorbates, it has been shown that adsorption energy increases as the d-band center shifts to higher energies. For example, Kitchin et al.[204] used DFT calculations to show

that a subsurface alloy shifted the d-band center of Pt(111), and that a lower d-band center led to a decrease in dissociative adsorption energy for hydrogen and oxygen. These changes in the metal d-bands can be caused by forming alloys or overlayers, or by changing the coordination state of the metal atom.[206-207]

Our results are shown in Figure 8 for the six bare clusters and for CO in vacuum. Here, the energies are all referenced to the vacuum level and the black vertical lines in each panel indicate the position of the Fermi level in the corresponding bare metal cluster. In all cases the three CO bands below the clusters' Fermi levels are occupied, while the band located at ~ -1 eV corresponds to the CO LUMO. It is interesting to point out that the cluster composition has a strong effect on the local density of states for both Au (top panels) and Pt (bottom panels) atoms. In particular, we observe a partial occupation of the top energy level in the clusters identified as Au_{13}, $Au_{12}Pt_1$-c, $Au_{12}pt_1$-t, and Pt_{13}, while the top energy level appears fully occupied in the $Pt_{12}Au_1$-t and $Pt_{12}Au_1$-c clusters (a sizeable gap exists between HOMO and LUMO for the top metal atom). Furthermore, the cluster composition has a strong effect on the position and intensity of the projection of the d-bands on the top metal atoms. From visual examination of Figure 50, it appears that the d-band is shifted towards higher energies for Pt than for Au. This may have important consequences from a catalysis perspective, based on the importance of the d-band center as discussed above. To quantify this effect, in Figure 51 we plot CO adsorption energy versus the d-band center, calculated as the first moment of the projected d-band density of states on the top atom referenced to the Fermi level.[204] As expected, the d-band center is higher for Pt atoms, which have stronger CO adsorption than Au atoms. In general, CO adsorption

is more favorable when the d-band center is higher, in qualitative agreement with DFT results obtained using plane-wave approaches on flat surfaces.

The observed differences in the projected DOS become more pronounced upon CO adsorption. In Figure 52 we report the projected DOS on the top metal atom in each cluster, and on C and O atoms of adsorbed CO. The energies are now expressed relative to the Fermi energy of the cluster+CO system. The DOS change significantly compared to those obtained for isolated metal clusters and gas-phase CO. For example, in all cases the metal atoms significantly contribute to the DOS of the three occupied bands of CO (see the bands at the three lowest energies), a direct consequence of the hybridization upon adsorption.

In all cases, CO adsorption causes large changes in the structure of the d-bands and also in their position with respect to the cluster Fermi energy. This effect is particularly pronounced for Au_{13}, $Pt_{12}Au_1$-t, $Au_{12}Pt_1$-t, and $Pt_{12}Au_1$-c. When CO adsorbs on Au atoms (top panels in Figure 52) the structure of the unoccupied molecular orbitals belonging to both C and O atoms changes significantly compared to that observed for gas-phase CO (in particular, the LUMO observed in gas-phase CO splits in two bands when CO adsorbs). However, very little evidence is provided by the DOS of the top three panels with respect to charge transfer from the metal to CO (only small and rather broad peaks are observed in connection to either C or O atoms at energy levels below the cluster Fermi level, but above -8 eV).

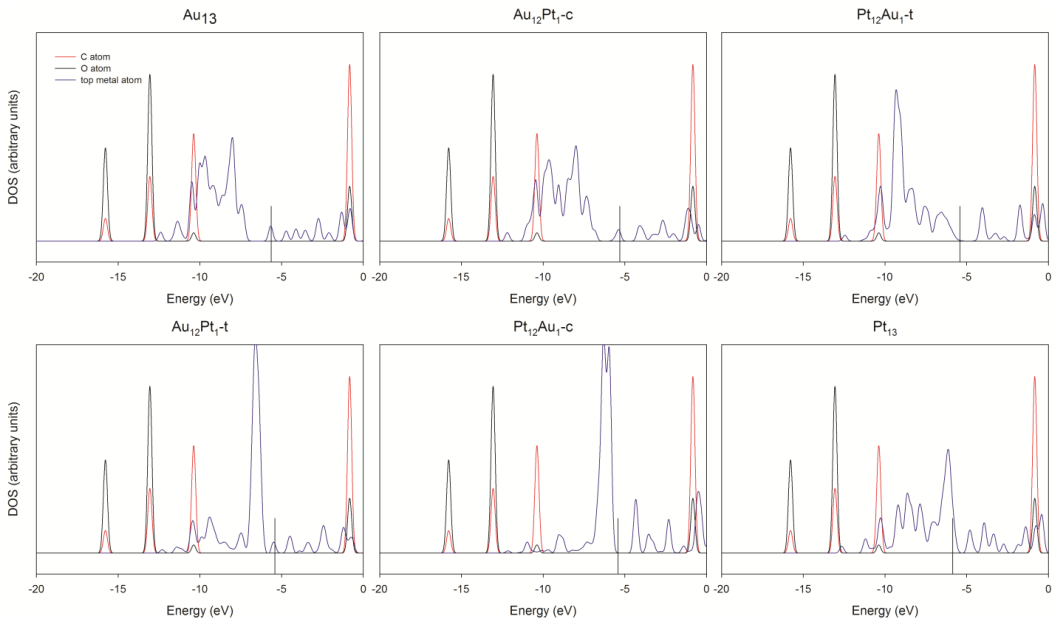

Figure 50: Density of states for the C and O atoms of gas-phase CO (red and black, respectively) and the top atom of the bare metal clusters (blue). The black vertical lines give the Fermi energy for the bare metal clusters.

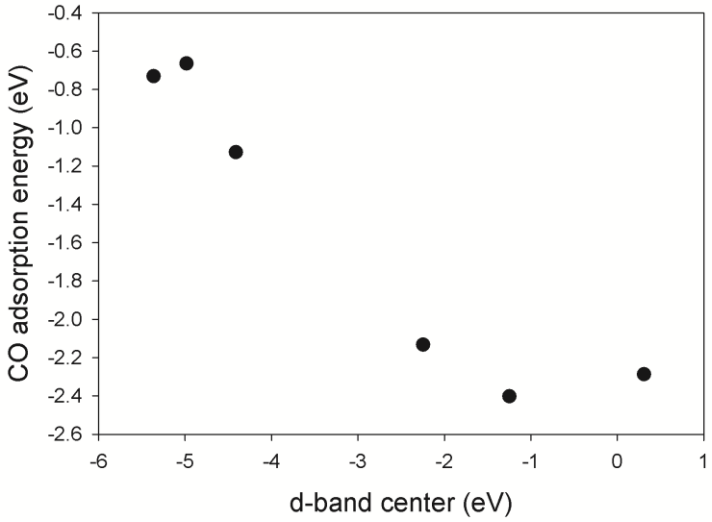

Figure 51: CO adsorption energy as a function of the d-band center of the top metal atom.

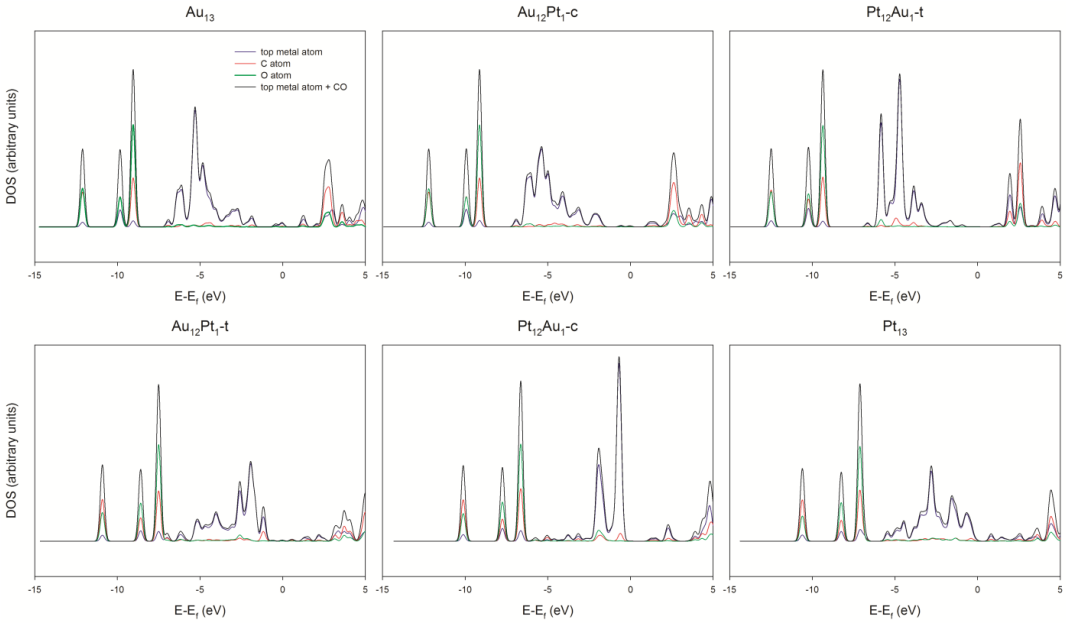

Figure 52: Density of states for the C (red) and O (green) atoms of adsorbed CO and the top atom of the metal clusters with adsorbed CO (blue). The energy is relative to the cluster Fermi energy.

When CO adsorbs on Pt atoms (bottom panels in Figure 52) both C and O atoms contribute to a reasonable extent to well-defined occupied orbitals in the range -3 to 0 eV. The effect is less evident on Pt_{13}, on which, however, the charge transfer is still sufficient to change the position of the d-band of the metal atom with respect to that observed before CO adsorption (compare Figure 10 to Figure 50). It is worth pointing out that the metal-C bond (see Table 4) is shorter on $Pt_{12}Au_1$-c than on Pt_{13}, possibly a consequence of the different features of the DOS shown in Figure 52.

To visualize the electronic effects due to CO adsorption and in particular the charge transfer consistent with the back-donation mechanism of Blyholder,[196] in Figure 53 we report plots of the electrostatic potentials of the six cluster+CO systems. In these plots a more negative value (shaded red) indicates higher electron density, while a more positive value (shaded blue) indicates lower electron density. The results indicate that,

for CO adsorbed on Au atoms, there is less electron density located around the C and O atoms compared to CO adsorbed on Pt atoms. This difference is consistent with a more significant back-donation of electrons to CO that appears to occur upon adsorption on Pt. The most pronounced back-donation appears on the $Pt_{12}Au_1$-c cluster, for which the metal-C bond is the shortest (see Table 4). Also in qualitative agreement with results for the C-O bond distance (Table 1), the results in Figure 10 suggest that when CO adsorbs on Au (top three panels) the electrostatic potential around the adsorbed CO does not depend significantly on the cluster composition. On the contrary, when CO adsorbs on Pt (bottom three panels in Figure 10) the electrostatic potential shows significant differences depending on the cluster composition.

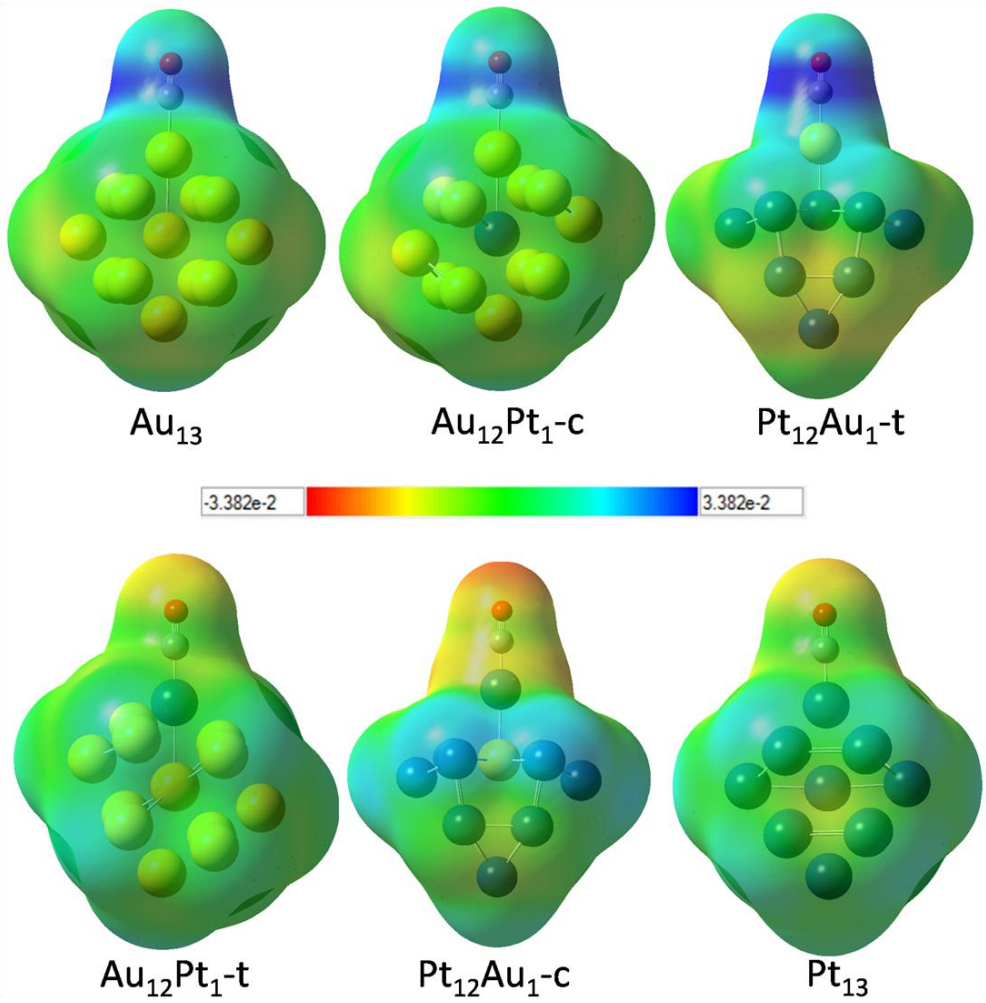

Figure 53: Electrostatic potential of the six clusters with adsorbed CO.

6.5. Conclusions

We have used DFT calculations to study the adsorption of CO on top of Pt and Au atoms in clusters of 13 atoms. Our results show that the cluster composition affects the adsorption energy and the C-O vibrational frequency even when adsorption occurs on the same metal atom (i.e., Au or Pt). Specifically, when adsorption occurs on Au, increasing the Pt content of the cluster increases the adsorption energy and decreases the C-O vibrational frequency. Increasing the Au content of the cluster when adsorption

occurs on Pt yields a decrease in the adsorption energy and an increase in the C-O vibrational frequency.

The electronic structures of the clusters were analyzed to rationalize these observed changes due to the cluster composition. More positive charges on the top Pt atom prior to adsorption result in stronger CO adsorption. For CO adsorption on a given metal, CO+cluster systems with lower HOMO-LUMO gaps have higher adsorption energy. Analysis of the density of states shows the effect of composition on the electronic structure of the clusters, which shifts the d-band and alters the electronic structure of adsorbed CO. Our results suggest that the closer the d-band center is to the Fermi level in the isolated cluster, the more favorable CO adsorption is. The electrostatic potential around the adsorbed CO molecule is more negative, providing evidence for rather significant electronic back donation, when adsorption occurs on Pt than when CO adsorbs on Au. Collectively, when compared to literature DFT results obtained for CO adsorption on clusters of metal atoms smaller than those considered here, as well as to those obtained for CO adsorption on flat metal surfaces, our results show that the local environment of a transition metal atom determines the properties of adsorbed CO. These effects appear to be strongly dependent on the cluster size, especially for metal clusters of a few atoms.

7. Conclusions and Future Work

This project could be expanded in several ways. MD simulations of nanoparticles supported on functionalized or defective carbon nanotubes could be performed. All of our simulations thus far have used pristine CNTs. It is common to create functionalized or defective CNT surfaces in order to anchor nanoparticles. MD simulations could be used to investigate how these functionalities or defects affect the structure and mobility of the supported nanoparticles. Our MD results have shown that the support geometry affects the structure of supported nanoparticles. DFT calculations could be performed to assess how changes in support alter the electronic structure and catalytic properties of the nanoparticles. DFT could also be used to study reactions on bimetallic clusters. We are currently studying hydrogen dissociation, which is important in, for example, proton exchange membrane fuel cells, on bimetallic Pt-Au clusters. Since hydrogen feeds produced by steam reforming of methanol contain CO, and CO poisons Pt catalysts, it would be beneficial to determine what cluster compositions maximize hydrogen dissociation while minimizing CO adsorption.

We have used molecular dynamics and density functional theory to study platinum-containing nanoparticles and clusters. Our simulations have shown that the diffusion of the nanoparticle center of mass is one order of magnitude slower for Pt nanoparticles supported by carbon nanotube bundles than for Pt nanoparticles supported by graphite. This could be one reason for the increased lifetime of carbon nanotube supported catalysts observed experimentally. Carbon nanotube supported nanoparticles exhibit a different structure than those supported by graphite. Density profiles for nanoparticles on carbon nanotubes are more disordered, and both the average

coordination number and the distribution of atoms with a given coordination number are different than on graphite. These differences in nanoparticle structure will lead to different catalytic activities and selectivities.

The effect of nanoparticle size on morphology and mobility was also assessed via simulations of nanoparticles containing 130, 249, and 498 atoms. We determined that nanoparticle size and diffusion coefficient are inversely related, and that increasing nanoparticle size increases melting temperature. The size of the nanoparticle appears to affect the nanoparticle structure less than the geometry of the support, as for all sizes the nanoparticles are more disordered on carbon nanotubes than on graphite. All three nanoparticles have different structures, as quantified by coordination numbers, on different supports. These results suggest the reactivity and selectivity of a catalyst will be affected by choice of support.

We also investigated the effect of the strength of the metal-carbon interaction. Our results indicate that the largest differences occur for small (130 atom) nanoparticles, and nanoparticles supported by small-diameter carbon nanotubes.

Bimetallic Pt-Au nanoparticles were studied to determine how the support and nanoparticle composition affect the distribution of atoms within and on the surface of the nanoparticles. We found that Au atoms tended to segregate to the exterior of the nanoparticles, regardless of the type of support. However, we found that the distribution of atoms on the nanoparticle surface varied for different supports and different nanoparticle compositions.

We also performed density functional theory calculations for CO adsorption on 13-atom Pt-Au clusters. We found that changing the environment around the metal

atom on which CO adsorbs changes the adsorption energy and C-O vibrational frequency. Electronic structure properties of the clusters, such as charges on relevant atoms, densities of states, and electronegativities, were calculated to explain these differences in the properties of adsorbed CO. These calculations provide insights into the behavior of small metal clusters, which can be important in catalysis, and could be used to help link molecular dynamics simulations to experiment.

In conclusion, we have performed molecular dynamics simulations and density functional theory calculations involving Pt and Pt-Au nanoparticles supported on graphite and carbon nanotubes. These include, to our knowledge, the first published molecular dynamics simulations of mono- and bimetallic nanoparticles supported on carbon nanotubes, an important class of catalytic materials. Our calculations have provided insight into the different behavior of nanoparticles on different supports, point to some of the possible reasons for experimentally observed differences in catalytic activity and selectivity caused by different supports, and could be used to aid in the design of highly selective or active catalysts.

8. Appendix

The CO adsorption energy calculated using six different exchange-correlation functionals is reported in Figure 54. All 6 data sets predict adsorption on Pt to be >1 eV more favorable than on Au. In general, the adsorption energies follow the trend described in the main text for B3LYP, with a few exceptions. For example, the adsorption energy on $Au_{12}Pt_1$-t calculated with the PBE1PBE functional is larger than that on $Pt_{12}Au_1$-c and Pt_{13}. The adsorption energy on Pt_{13} calculated with the PBE functional is much lower than that on $Au_{12}Pt_1$-t and $Pt_{12}Au_1$-c. Aside from these differences, which could be due to the geometry minimization procedure for a given structure getting trapped in a local minimum with relatively high energy, the trend discussed in the main text appears to be independent of the choice of exchange-correlation functional. Calculations using all functionals other than B3LYP predict higher adsorption energies for CO on Au_{13} than the experimental range of 0.54-0.79 eV for CO on Au nanoparticles.[193] Calculations using all functionals except for PBE overestimate the adsorption energy for CO on Pt_{13} compared to the experimental value of -2.13 eV for CO on alumina-supported Pt nanoparticles.[192] Calculations using PBE1PBE and B3LYP come closest to the experimental value, at -2.22 and -2.40 eV, respectively.

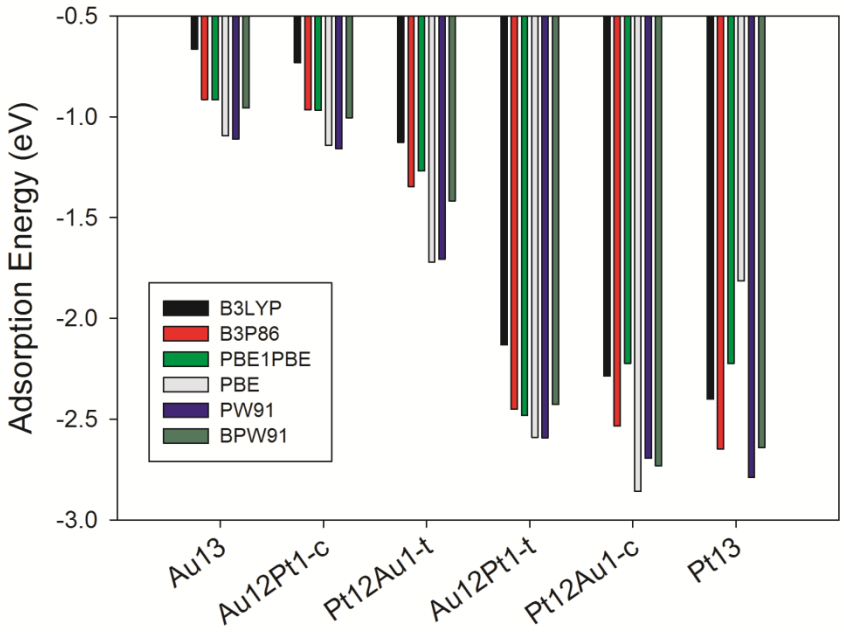

Figure 54: CO adsorption energy on the 6 clusters for the 6 functionals considered here.

In Figure 55 we report the C-O stretching frequency calculated using different functionals. The results follow the trend described in the main text for all of the functionals, with the highest frequency occurring for CO adsorption on $Pt_{12}Au_1$-t and the lowest frequency occurring for adsorption on Pt_{13}. However, the different functionals produce very different values. Frequencies calculated using hybrid functionals (B3LYP, B3P86, and PBE1PBE) are consistently ~100 cm^{-1} higher than those calculated using non-hybrid functionals (PBE, PW91, and BPW91). Compared to the experimental values[192, 195] of ~2070-2075 cm^{-1} for CO adsorbed on alumina-supported Pt nanoparticles, B3LYP is the most accurate, predicting a frequency ~15 cm^{-1} higher. B3P86 and PBE1PBE overestimate the frequency by ~40 and ~50 cm^{-1}, respectively, while PBE, PW91, and BPW91 all underestimate the frequency by ~50

cm^{-1}. For CO adsorbed on Au (experimental value[193] of 2123 cm^{-1}), calculations performed using B3LYP, B3P86, and PBE1PBE predict frequencies ~50, ~65, and ~80 cm^{-1} higher, respectively. Calculations performed using PBE, PW91, and BPW91 all predict frequencies ~40 cm^{-1} lower than the experimental value.

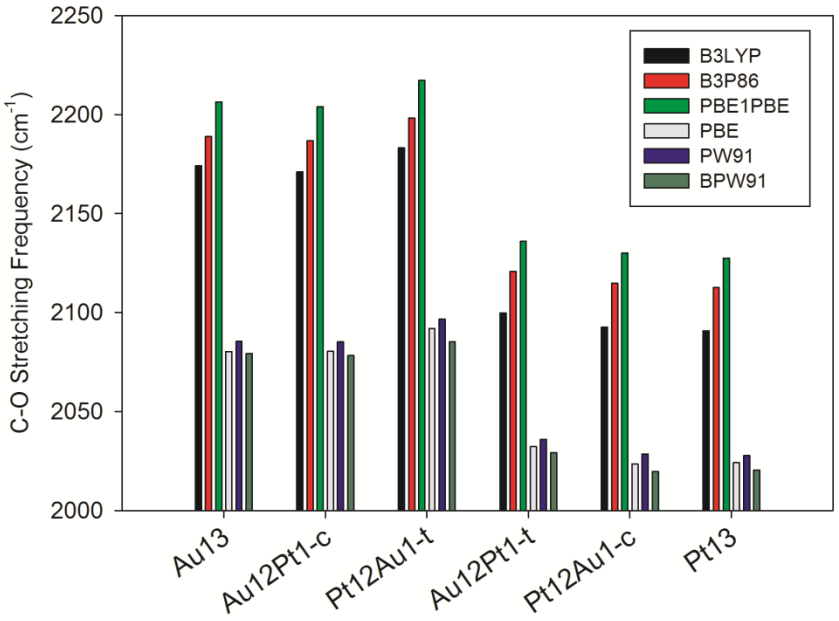

Figure 55: C-O stretching frequency for the 6 functionals considered here.

Figure 56 through Figure 61 show the highest occupied and lowest unoccupied molecular orbitals (HOMOs and LUMOs, respectively) for the six clusters, both with and without adsorbed CO. In these figures Pt and Au atoms are represented by blue and yellow spheres, respectively. Red and green represent positive and negative phases of the orbitals, respectively.

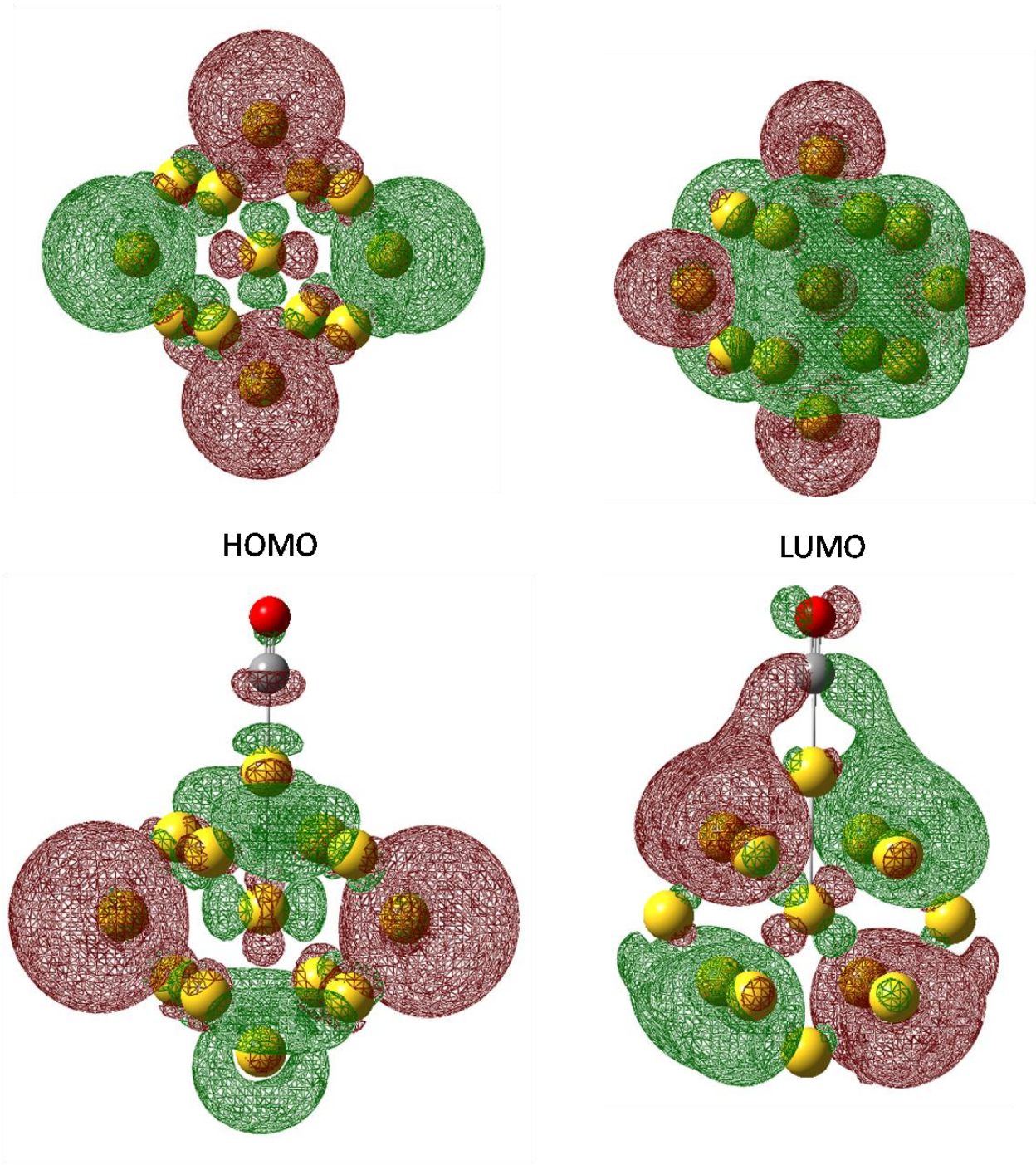

Figure 56: HOMO (left) and LUMO (right) for Au_{13} (top) and Au_{13} with adsorbed CO (bottom).

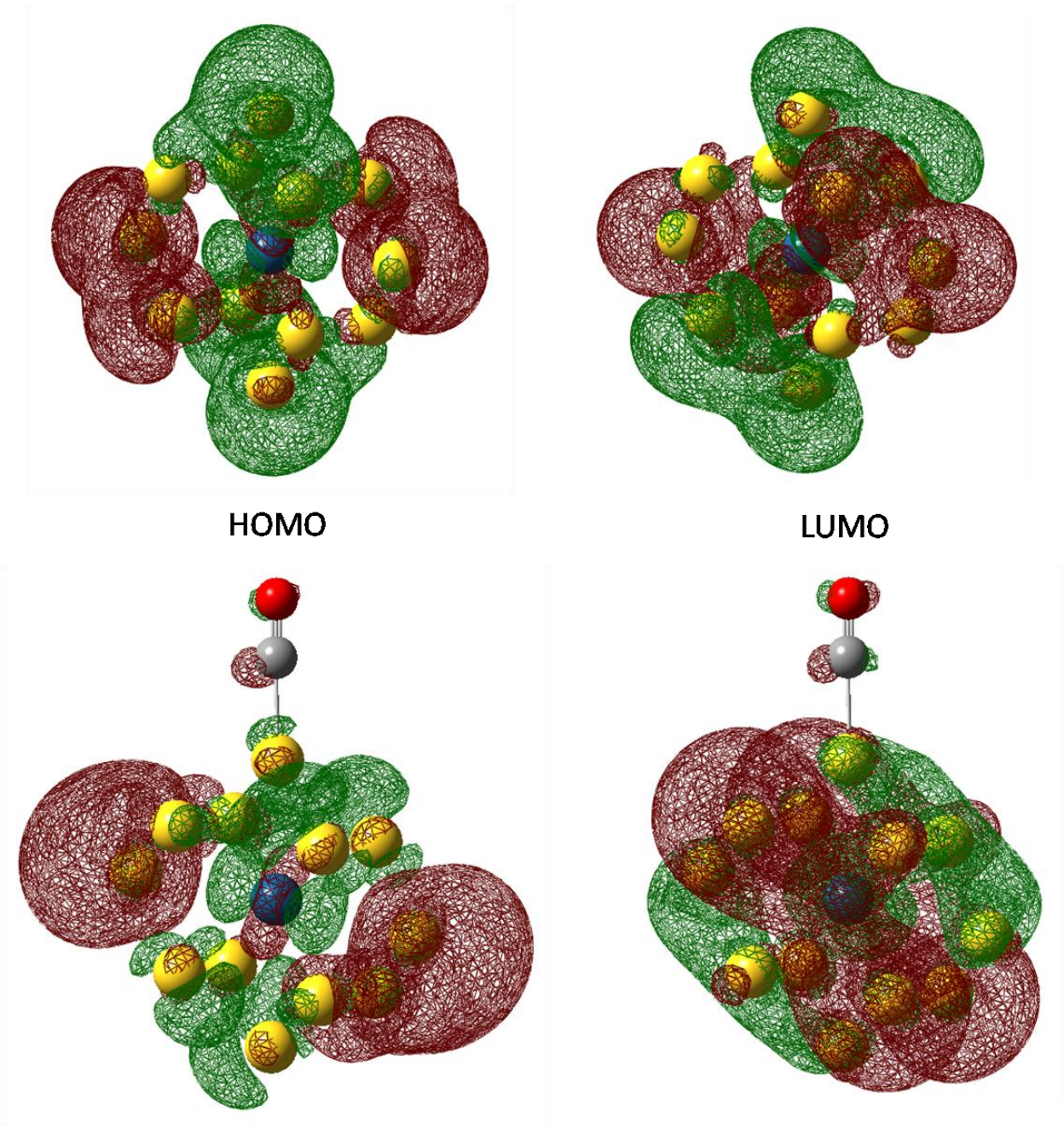

Figure 57: HOMO (left) and LUMO (right) for $Au_{12}Pt_1$-c (top) and $Au_{12}Pt_1$-c with adsorbed CO (bottom).

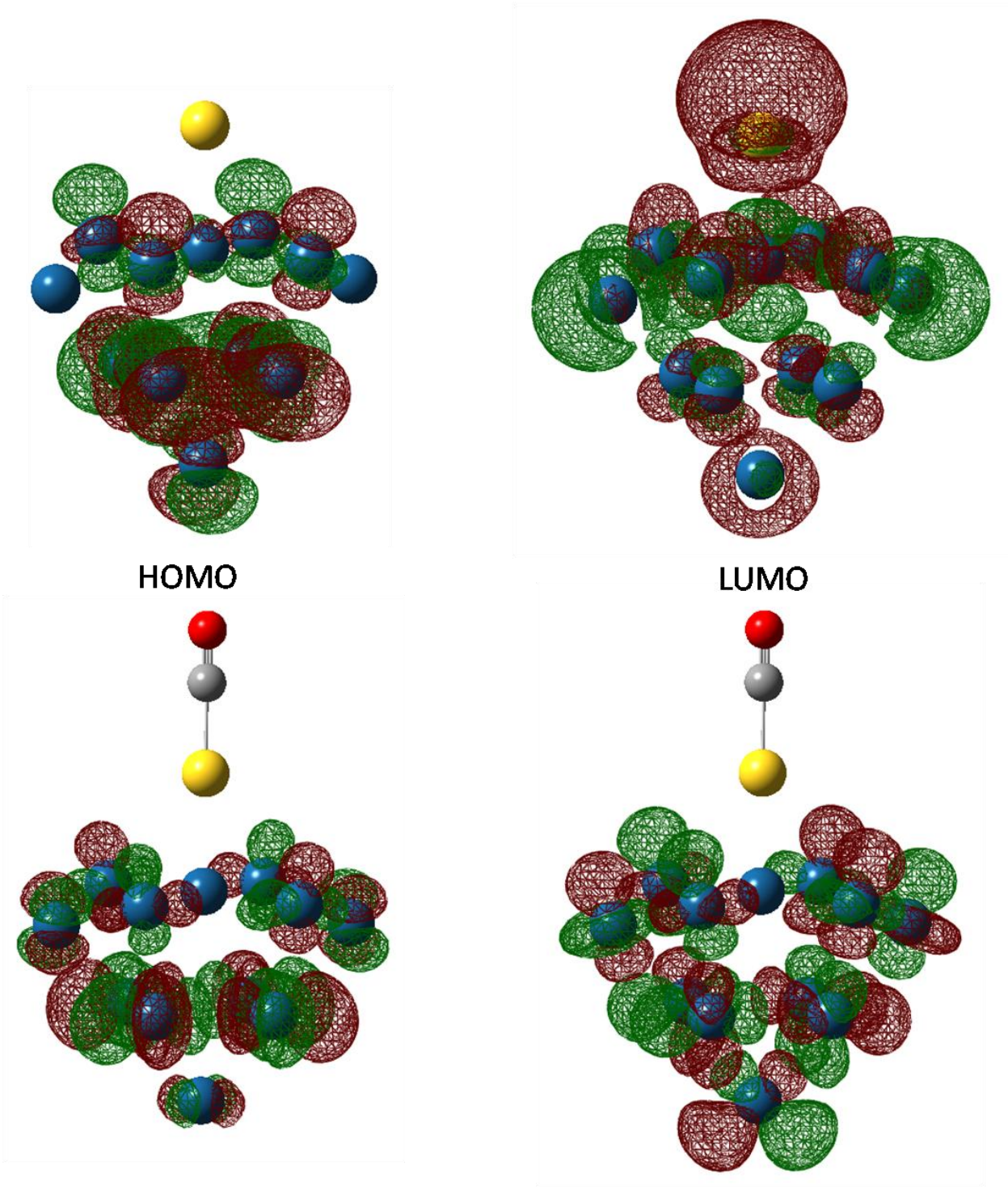

Figure 58: HOMO (left) and LUMO (right) for $Pt_{12}Au_1$-t (top) and $Pt_{12}Au_1$-t with adsorbed CO (bottom).

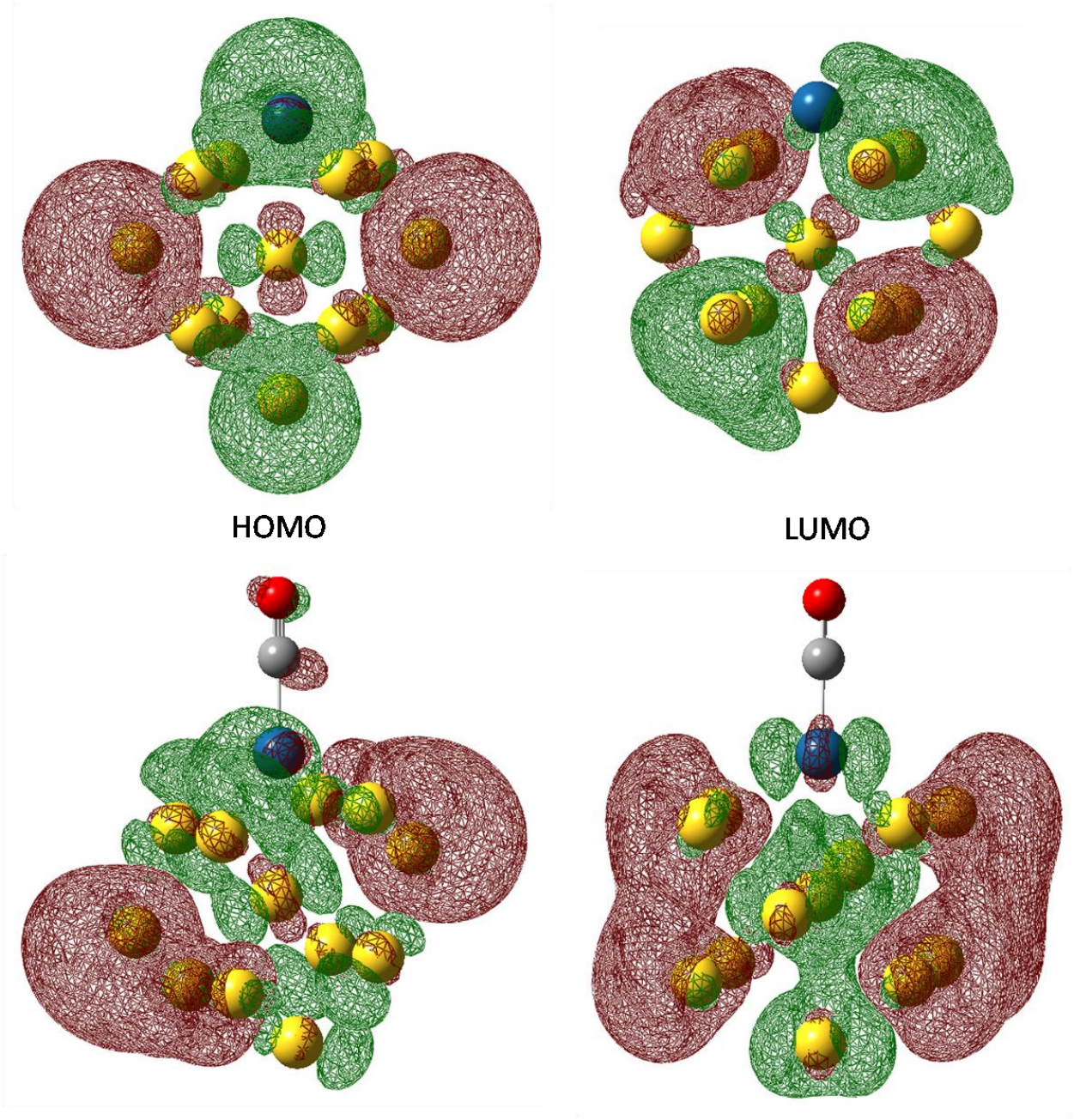

Figure 59: HOMO (left) and LUMO (right) for $Au_{12}Pt_1$-t (top) and $Au_{12}Pt_1$-t with adsorbed CO (bottom).

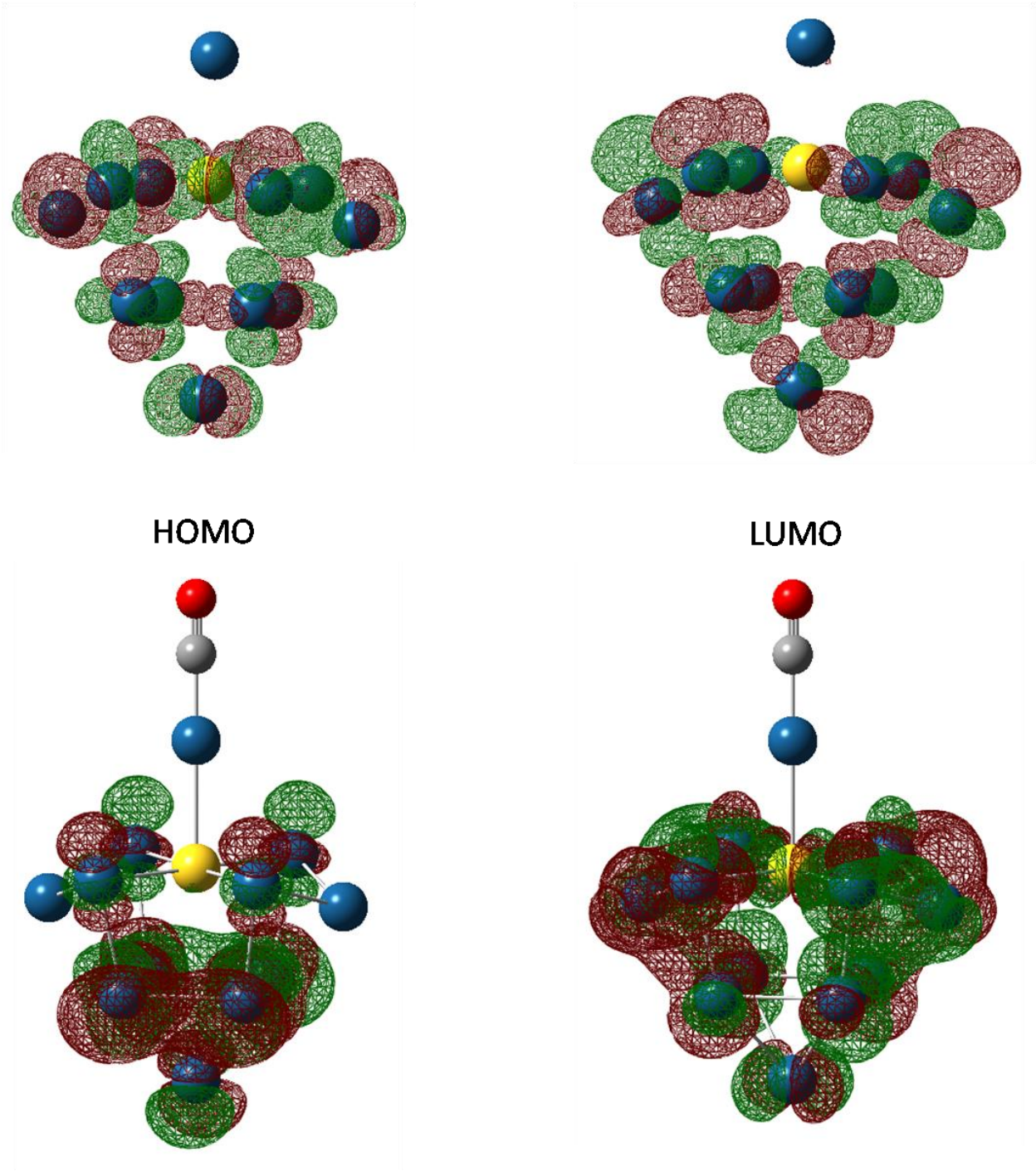

Figure 60: HOMO (left) and LUMO (right) for $Pt_{12}Au_1$-c (top) and $Pt_{12}Au_1$-c with adsorbed CO (bottom).

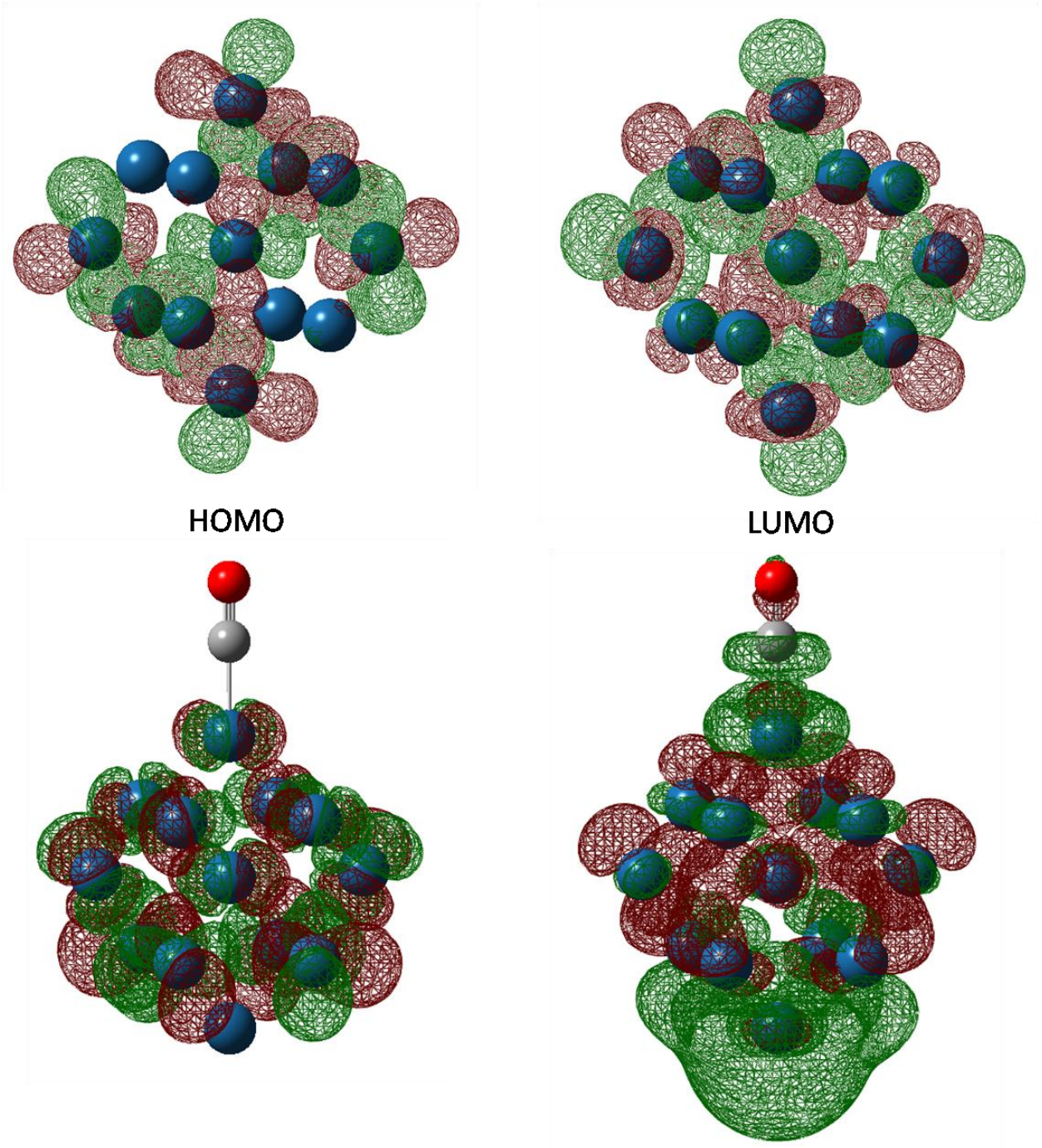

Figure 61: HOMO (left) and LUMO (right) for Pt_{13} (top) and Pt_{13} with adsorbed CO (bottom).

The following is a sample Gaussian input file for the geometry optimization of Pt_{13} with adsorbed CO. The first section contains the details such as number of processors used, calculation type, the functional used, and other options. This is followed by the initial positions of the atoms in z-matrix format, and the values for the distances, angles, and dihedrals. Next comes a list of atoms, indicating where there are bonds (for example, the line "2 14 1.0" indicates atoms 2 and 14 are connected by a single bond). The final section specifies the basis sets and effective core potentials used in the calculation. More details on the format of input files can be found in the Gaussian documentation.

```
%Chk=b3lyp.chk
%nproclinda=8
#p opt freq=noraman ub3lyp/gen pseudo=read scf=(maxcycle=999) geom=connectivity

CO adsorption on Pt13

0 3
 Pt
 Pt                  1           B1
 Pt                  1           B2      2           A1
 Pt                  3           B3      1           A2      2           D1
 Pt                  2           B4      1           A3      3           D2
 Pt                  3           B5      1           A4      2           D3
 Pt                  6           B6      3           A5      1           D4
 Pt                  4           B7      3           A6      1           D5
 Pt                  8           B8      4           A7      3           D6
 Pt                  3           B9      1           A8      2           D7
 Pt                 10           B10     3           A9      1           D8
 Pt                 10           B11     3           A10     1           D9
 Pt                 10           B12     3           A11     1           D10
 C                   2           B13     1           A12    10           D11
 O                   2           B14     1           A13    10           D12

  B1              2.78954332
  B2              2.78954332
  B3              2.78954332
  B4              2.78954332
  B5              2.78954332
  B6              2.78954332
  B7              2.78954332
  B8              2.78954332
  B9              2.78954332
  B10             2.78954332
  B11             2.78954332
```

```
 B12                2.78954332
 B13                1.80000000
 B14                2.92000000
 A1                90.00000000
 A2                90.00000000
 A3                60.00000000
 A4                60.00000000
 A5               120.00000000
 A6               120.00000000
 A7               120.00000000
 A8                60.00000000
 A9                60.00000000
 A10               90.00000000
 A11              120.00000000
 A12              120.00000000
 A13              120.00000000
 D1                 0.00000000
 D2              -125.26438968
 D3               125.26438968
 D4               -70.52877937
 D5                54.73561032
 D6                 0.00000000
 D7                54.73561032
 D8               180.00000000
 D9               125.26438968
 D10              180.00000000
 D11             -180.00000000
 D12             -180.00000000

1
2 14 1.0
3
4
5
6
7
8
9
10
11
12
13
14 15 3.0
15

C     0
6-311G
D   1        1.00
     0.5870000                    1.0000000
****
O     0
6-311G
D   1        1.00
     0.9610000                    1.0000000
****
Pt    0
```

LANL2DZ
****

Pt 0
LANL2DZ

9. References

1. Satterfield, C. N., *Heterogeneous Catalysis in Industrial Practice*, Second ed.; Krieger Publishing Company: Malabar, FL, 1996.

2. Peigney, A.; Laurent, C.; Flahaut, E.; Bacsa, R. R.; Rousset, A., Specific surface area of carbon nanotubes and bundles of carbon nanotubes. *Carbon* **2001,** *39* (4), 507-514.

3. Zacharia, R.; Kim, K. Y.; Hwang, S. W.; Nahm, K. S., Intrinsic linear scaling of hydrogen storage capacity of carbon nanotubes with the specific surface area. *Catalysis Today* **2007,** *120* (3-4), 426-431.

4. Kayiran, S. B.; Lamari, F. D.; Levesque, D., Adsorption Properties and Structural Characterization of Activated Carbons and Nanocarbons. *The Journal of Physical Chemistry B* **2004,** *108* (39), 15211-15215.

5. Bacsa, R. R.; Laurent, C.; Peigney, A.; Bacsa, W. S.; Vaugien, T.; Rousset, A., High specific surface area carbon nanotubes from catalytic chemical vapor deposition process. *Chemical Physics Letters* **2000,** *323* (5-6), 566-571.

6. Baughman, R. H.; Zakhidov, A. A.; de Heer, W. A., Carbon Nanotubes--the Route Toward Applications. *Science* **2002,** *297* (5582), 787-792.

7. Terrones, M., Carbon nanotubes: Synthesis and properties, electronic devices and other emerging applications. *International Materials Reviews* **2004,** *49* (6), 325-377.

8. Liang, W.; Bockrath, M.; Bozovic, D.; Hafner, J. H.; Tinkham, M.; Park, H., Fabry - Perot interference in a nanotube electron waveguide. *Nature* **2001,** *411* (6838), 665-669.

9. Frank, S.; Poncharal, P.; Wang, Z. L.; de Heer, W. A., Carbon Nanotube Quantum Resistors. *Science* **1998,** *280* (5370), 1744-1746.

10. Skoulidas, A. I.; Ackerman, D. M.; Johnson, J. K.; Sholl, D. S., Rapid Transport of Gases in Carbon Nanotubes. *Physical Review Letters* **2002,** *89* (18), 185901.

11. Joo, S. H.; Choi, S. J.; Oh, I.; Kwak, J.; Liu, Z.; Terasaki, O.; Ryoo, R., Ordered nanoporous arrays of carbon supporting high dispersions of platinum nanoparticles. *Nature* **2001,** *412* (6843), 169-172.

12. Kongkanand, A.; Kuwabata, S.; Girishkumar, G.; Kamat, P. V., Single-Wall Carbon Nanotubes Supported Platinum Nanoparticles with Improved Electrocatalytic Activity for Oxygen Reduction Reaction. *Langmuir* **2006,** *22*, 2392-2396.

13. Kongkanand, A.; Vinodgopal, K.; Kuwabata, S.; Kamat, P. V., Highly Dispersed Pt Catalysts on Single-Walled Carbon Nanotubes and Their Role in Methanol Oxidation. *Journal of Physical Chemistry B* **2006,** *110* (33), 16185-16188.

14. Li, W.; Liang, C.; Zhou, W.; Qiu, J.; Zhou; Sun, G.; Xin, Q., Preparation and Characterization of Multiwalled Carbon Nanotube-Supported Platinum for Cathode Catalysts of Direct Methanol Fuel Cells. *The Journal of Physical Chemistry B* **2003,** *107* (26), 6292-6299.

15. Baret, B.; Aubert, P. H.; L'Hermite, M. M.; Pinault, M.; Reynaud, C.; Etcheberry, A.; Perez, H., Nanocomposite electrodes based on pre-synthesized organically capped platinum nanoparticles and carbon nanotubes. Part I: Tuneable low platinum loadings, specific H upd feature and evidence for oxygen reduction. *Electrochimica Acta* **2009,** *54* (23), 5421-5430.

16. Perez, H.; Morin, A.; Akrour, L.; Cremona, C.; Baret, B.; Haccoun, J.; Escribano, S.; Etcheberry, A., Evidence for high performances of low Pt loading electrodes based on capped platinum electrocatalyst and carbon nanotubes in fuel cell devices. *Electrochimica Acta* **2010,** *55* (7), 2358-2362.

17. Ye, F.; Wang, T.; Li, J.; Wang, Y.; Li, J.; Wang, X., Pt Nanoclusters Electrodeposited on Single-Walled Carbon Nanotubes for Electrochemical Catalysis. *Journal of The Electrochemical Society* **2009,** *156* (8), B981-B985.

18. Lin, Y.; Cui, X.; Yen, C.; Wai, C. M., Platinum/Carbon Nanotube Nanocomposite Synthesized in Supercritical Fluid as Electrocatalysts for Low-Temperature Fuel Cells. *The Journal of Physical Chemistry B* **2005,** *109* (30), 14410-14415.

19. Wang, J. J.; Yin, G. P.; Zhang, J.; Wang, Z. B.; Gao, Y. Z., High utilization platinum deposition on single-walled carbon nanotubes as catalysts for direct methanol fuel cell. *Electrochimica Acta* **2007,** *52* (24), 7042-7050.

20. Rajesh, B.; Ravindranathan Thampi, K.; Bonard, J. M.; Xanthopoulos, N.; Mathieu, H. J.; Viswanathan, B., Carbon Nanotubes Generated from Template Carbonization of Polyphenyl Acetylene as the Support for Electrooxidation of Methanol. *The Journal of Physical Chemistry B* **2003,** *107* (12), 2701-2708.

21. Zheng, S.-F.; Hu, J.-S.; Zhong, L.-S.; Wan, L.-J.; Song, W.-G., In Situ One-Step Method for Preparing Carbon Nanotubes and Pt Composite Catalysts and Their Performance for Methanol Oxidation. *The Journal of Physical Chemistry C* **2007,** *111* (30), 11174-11179.

22. Wang, C.; Waje, M.; Wang, X.; Tang, J. M.; Haddon, R. C.; Yan, Y., Proton Exchange Membrane Fuel Cells with Carbon Nanotube Based Electrodes. *Nano Letters* **2004,** *4* (2), 345-348.

23. Tang, J. M.; Jensen, K.; Waje, M.; Li, W.; Larsen, P.; Pauley, K.; Chen, Z.; Ramesh, P.; Itkis, M. E.; Yan, Y.; Haddon, R. C., High Performance Hydrogen Fuel Cells with Ultralow Pt Loading Carbon Nanotube Thin Film Catalysts†. *The Journal of Physical Chemistry C* **2007,** *111* (48), 17901-17904.

24. Shao, Y.; Yin, G.; Gao, Y.; Shi, P., Durability study of Pt/C and Pt/CNTs Catalysts under Simulated PEM Fuel Cell Conditions. *Journal of the Electrochemical Society* **2006,** *153* (6), A1093-A1097.

25. Wang, X.; Li, W.; Chen, Z.; Waje, M.; Yan, Y., Durability investigation of carbon nanotube as catalyst support for proton exchange membrane fuel cell. *Journal of Power Sources* **2006,** *158* (1), 154-159.

26. Davis, S. M.; Zaera, F.; Somorjai, G. A., Surface structure and temperature dependence of n-hexane skeletal rearrangement reactions catalyzed over platinum single crystal surfaces: Marked structure sensitivity of aromatization. *Journal of Catalysis* **1984,** *85* (1), 206-223.

27. Bratlie, K. M.; Lee, H.; Komvopoulos, K.; Yang, P.; Somorjai, G. A., Platinum Nanoparticle Shape Effects on Benzene Hydrogenation Selectivity. *Nano Letters* **2007,** *7* (10), 3097-3101.

28. Luedtke, W. D.; Landman, U., Slip Diffusion and Levy Flights of an Adsorbed Gold Nanoclulster. *Physical Review Letters* **1999,** *82* (19), 3835-3838.

29. Maruyama, Y.; Murakami, J., Truncated Levy walk of a nanocluster bound weakly to an atomically flat surface: Crossover from superdiffusion to normal diffusion. *Physical Review B* **2003,** *67*, 085406.

30. Maruyama, Y., Temperature dependence of Levy-type stick-slip diffusion of gold nanocluster on graphite. *Physical Review B* **2004,** *69*, 245408-1,245408-6.

31. Lewis, L. J.; Jensen, P.; Combe, N.; Barrat, J. L., Diffusion of gold nanoclusters on graphite. *Physical Review B* **2000,** *61* (23), 16084-16090.

32. Lamas, E. J.; Balbuena, P. B., Adsorbate Effects on Structure and Shape of Supported Nanoclusters: A Molecular Dynamics Study. *Journal of Physical Chemistry B* **2003,** *107* (42), 11682-11689.

33. Chen, J.; Chan, K.-Y., Size-dependent mobility of platinum cluster on a graphite surface. *Molecular Simulation* **2005,** *31* (6-7), 527-533.

34. Jensen, P.; Clement, A.; Lewis, L. J., Diffusion of nanoclusters on non-ideal surfaces. *Physica E* **2004,** *21* (1), 71-76.

35. Yoon, B.; Luedtke, W. D.; Gao, J.; Landman, U., Diffusion of Gold Clusters on Defective Graphite Surfaces. *Journal of Physical Chemistry B* **2003,** *107* (24), 5882-5891.

36. Ferrando, R.; Jellinek, J.; Johnston, R. L., Nanoalloys: From Theory to Applications of Alloy Clusters and Nanoparticles. *Chemical Reviews* **2008,** *108* (3), 845-910.

37. Choi, J.-H.; Park, K.-W.; Park, I.-S.; Kim, K.; Lee, J.-S.; Sung, Y.-E., A PtAu Nanoparticle Electrocatalyst for Methanol Electro-oxidation in Direct Methanol Fuel Cells. *Journal of The Electrochemical Society* **2006,** *153* (10), A1812-A1817.

38. Yang, L.; Yang, W.; Cai, Q., Well-Dispersed PtAu Nanoparticles Loaded into Anodic Titania Nanotubes: A High Antipoison and Stable Catalyst System for Methanol Oxidation in Alkaline Media. *The Journal of Physical Chemistry C* **2007,** *111* (44), 16613-16617.

39. Zhao, D.; Xu, B.-Q., Platinum covering of gold nanoparticles for utilization enhancement of Pt in electrocatalysts. *Physical Chemistry Chemical Physics* **2006,** *8* (43), 5106-5114.

40. Xu, J.; Zhao, T.; Liang, Z.; Zhu, L., Facile Preparation of AuPt Alloy Nanoparticles from Organometallic Complex Precursor. *Chemistry of Materials* **2008,** *20* (5), 1688-1690.

41. Wang, S.; Kristian, N.; Jiang, S.; Wang, X., Controlled deposition of Pt on Au nanorods and their catalytic activity towards formic acid oxidation. *Electrochemistry Communications* **2008,** *10* (7), 961-964.

42. Xu, J. B.; Zhao, T. S.; Liang, Z. X., Carbon supported platinum-gold alloy catalyst for direct formic acid fuel cells. *Journal of Power Sources* **2008,** *185* (2), 857-861.

43. Hernández-Fernández, P.; Rojas, S.; Ocón, P.; Gómez de la Fuente, J. L.; San Fabián, J.; Sanza, J.; Peña, M. A.; García-García, F. J.; Terreros, P.; Fierro, J. L. G., Influence of the Preparation Route of Bimetallic Pt−Au Nanoparticle Electrocatalysts for the Oxygen Reduction Reaction. *The Journal of Physical Chemistry C* **2007,** *111* (7), 2913-2923.

44. Zhang, J.; Sasaki, K.; Sutter, E.; Adzic, R. R., Stabilization of Platinum Oxygen-Reduction Electrocatalysts Using Gold Clusters. *Science* **2007,** *315* (5809), 220-222.

45. Guo, X.; Guo, D.-J.; Qiu, X.-P.; Chen, L.-Q.; Zhu, W.-T., A simple one-step preparation of high utilization AuPt nanoparticles supported on MWCNTs for methanol oxidation in alkaline medium. *Electrochemistry Communications* **2008,** *10* (11), 1748-1751.

46. Desai, S.; Neurock, M., A first principles analysis of CO oxidation over Pt and Pt66.7%Ru33.3% (111) surfaces. *Electrochimica Acta* **2003,** *48* (25-26), 3759-3773.

47. Zhang, C.; Hu, P.; Alavi, A., A General Mechanism for CO Oxidation on Close-Packed Transition Metal Surfaces. *Journal of the American Chemical Society* **1999,** *121* (34), 7931-7932.

48. Ford, D. C.; Xu, Y.; Mavrikakis, M., Atomic and molecular adsorption on Pt(1 1 1). *Surface Science* **2005,** *587* (3), 159-174.

49. Doll, K., CO adsorption on the Pt(1 1 1) surface: a comparison of a gradient corrected functional and a hybrid functional. *Surface Science* **2004,** *573* (3), 464-473.

50. Yudanov, I. V.; Sahnoun, R.; Neyman, K. M.; Rosch, N., Metal nanoparticles as models of single crystal surfaces and supported catalysts: Density functional study of size effects for CO/Pd(111). *The Journal of Chemical Physics* **2002,** *117* (21), 9887-9896.

51. Sadek, M. M.; Wang, L., Effect of Adsorption Site, Size, and Composition of Pt/Au Bimetallic Clusters on the CO Frequency: A Density Functional Theory Study. *The Journal of Physical Chemistry A* **2006,** *110* (51), 14036-14042.

52. Song, C.; Ge, Q.; Wang, L., DFT Studies of Pt/Au Bimetallic Clusters and Their Interactions with the CO Molecule. *The Journal of Physical Chemistry B* **2005,** *109* (47), 22341-22350.

53. Jacob, T.; Muller, R. P.; Goddard, W. A., Chemisorption of Atomic Oxygen on Pt(111) from DFT Studies of Pt-Clusters. *The Journal of Physical Chemistry B* **2003,** *107* (35), 9465-9476.

54. Linic, S.; Jankowiak, J.; Barteau, M. A., Selectivity driven design of bimetallic ethylene epoxidation catalysts from first principles. *Journal of Catalysis* **2004,** *224* (2), 489-493.

55. Studt, F.; Abild-Pedersen, F.; Bligaard, T.; Sorensen, R. Z.; Christensen, C. H.; Norskov, J. K., Identification of Non-Precious Metal Alloy Catalysts for Selective Hydrogenation of Acetylene. *Science* **2008,** *320* (5881), 1320-1322.

56. Wu, G.-W.; Chan, K.-Y., Morphology of platinum clusters on graphite at different loadings. *Surface Science* **1996,** *365* (1), 38-52.

57. Huang, S.-P.; Balbuena, P. B., Platinum nanoclusters on graphite substrates: a molecular dynamics study. *Molecular Physics* **2002,** *100* (13), 2165-2174.

58. Green, D. W.; Perry, R. H., *Perry's Chemical Engineers' Handbook*. 8th ed.; McGraw-Hill: New York, 2007.

59. Sankaranarayanan, S. K. R. S.; Bhethanabotla, V. R.; Joseph, B., Molecular dynamics simulations of the structural and dynamic properties of graphite-supported bimetallic transition metal clusters. *Physical Review B* **2005,** *72,* 195405.

60. Plimpton, S., Fast Parallel Algorithms for Short-Range Molecular Dynamics. *Journal of Computational Physics* **1995,** *117* (1), 1-19.

61. Foiles, S. M.; Baskes, M. I.; Daw, M. S., Embedded-atom-method functions for the fcc metals Cu, Ag, Au, Ni, Pd, Pt, and their alloys. *Physical Review B* **1986,** *33* (12), 7983-7991.

62. Foiles, S. M.; Daw, M. S., Calculation of the thermal expansion of metals using the embedded-atom method. *Physical Review B* **1988,** *38* (17), 12643.

63. Foiles, S. M.; Adams, J. B., Thermodynamic properties of fcc transition metals as calculated with the embedded-atom method. *Physical Review B* **1989,** *40* (9), 5909.

64. Dahmen, U.; Hetheringtont, C. J. D.; O'Keefe, M. A.; Westmacottt, K. H.; Mills, M. J.; Daw, M. S.; Vitek, V., Atomic structure of a Σ99 grain boundary in aluminium: A comparison between atomic-resolution observation and pair-potential and embedded-atom simulations. *Philosophical Magazine Letters* **1990,** *62* (5), 327 - 335.

65. Allen, M. P.; Tildesley, D. J., *Computer Simulation of Liquids,* Oxford University Press: Oxford, 2004.

66. Liem, S. Y.; Chan, K.-Y., Effective pairwise potential for simulations of adsorbed platinum. *Molecular Physics* **1995,** *86* (4), 939-949.

67. Sutton, A. P.; Chen, J., Long-range Finnis-Sinclair potentials. *Philosophical Magazine Letters* **1990,** *61* (3), 139 - 146.

68. Chen, W.-X.; Lee, J. Y.; Liu, Z., Preparation of Pt and PtRu nanoparticles supported on carbon nanotubes by microwave-assisted heating polyol process. *Materials Letters* **2004,** *58* (25), 3166-3169.

69. Li, X.; Hsing, I.-M., The effect of the Pt deposition method and the support on Pt dispersion on carbon nanotubes. *Electrochimica Acta* **2006,** *51,* 5250-5258.

70. Naumovets, A. G.; Zhang, Z., Fidgety particles on surfaces: how do they jump, walk, group, and settle in virgin areas? *Surface Science* **2002,** *500*, 414-436.

71. Bandow, S.; Asaka, S.; Saito, Y.; Rao, A. M.; Grigorian, L.; Richter, E.; Eklund, P. C., Effect of the Growth Temperature on the Diameter Distribution and Chirality of Single-Wall Carbon Nanotubes. *Physical Review Letters* **1998,** *80* (17), 3779.

72. Fogler, H. S., *Elements of Chemical Reaction Engineering*, Prentice Hall: Upper Saddle River, New Jersey, 2005.

73. Dicks, A. L., The role of carbon in fuel cells. *Journal of Power Sources* **2006,** *156* (2), 128-141.

74. Morrow, B. H.; Striolo, A., Morphology and Diffusion Mechanism of Platinum Nanoparticles on Carbon Nanotube Bundles. *J. Phys. Chem. C* **2007,** *111* (48), 17905-17913.

75. Bergamaski, K.; Pinheiro, A. L. N.; Teixeira-Neto, E.; Nart, F. C., Nanoparticle Size Effects on Methanol Electrochemical Oxidation on Carbon Supported Platinum Catalysts. *Journal of Physical Chemistry B* **2006,** *110*, 19271-19279.

76. Chen, G.; Kawazoe, Y., Interaction between a single Pt atom and a carbon nanotube studied by density functional theory. *Physical Review B* **2006,** *73*, 125410.

77. Wang, L.-L.; Khare, S. V.; Chirita, V.; Johnson, D. D.; Rockett, A. A.; Frenkel, A. I.; Mack, N. H.; Nuzzo, R. G., Origin of Bulklike Structure and Bond Length Disorder of Pt37 and Pt6Ru37 Clusters on Carbon: Comparison of Theory and Experiment. *Journal of the American Chemical Society* **2006,** *128* (1), 131-142.

78. Wang, L.-L.; Johnson, D. D., Shear Instabilities in Metallic Nanoparticles: Hydrogen-Stabilized Structure of Pt37 on Carbon. *Journal of the American Chemical Society* **2007,** *129* (12), 3658-3664.

79. Tersoff, J., New empirical approach for the structure and energy of covalent systems. *Physical Review B* **1988,** *37* (12), 6991-7000.

80. Yoon, B.; Akulin, V. M.; Cahuzac, P.; Carlier, F.; de Frutos, M.; Masson, A.; Mory, C.; Colliex, C.; Bréchignac, C., Morphology control of the supported islands grown from soft-landed clusters. *Surface Science* **1999,** *443* (1-2), 76-88.

81. Steinhardt, P. J.; Nelson, D. R.; Ronchetti, M., Bond-orientational order in liquids and glasses. *Physical Review B* **1983,** *28* (2), 784.

82. ten Wolde, P. R.; Ruiz-Montero, M. J.; Frenkel, D., Numerical calculation of the rate of crystal nucleation in a Lennard-Jones system at moderate undercooling. *Journal of Chemical Physics* **1996,** *104* (24), 9932-9947.

83. Tessonnier, J.-P.; Pesant, L.; Ehret, G.; Ledoux, M. J.; Pham-Huu, C., Pd nanoparticles introduced inside multi-walled carbon nanotubes for selective hydrogenation of cinnamaldehyde into hydrocinnamaldehyde. *Applied Catalysis A: General* **2005,** *288* (1-2), 203-210.

84. Selvaraj, V.; Alagar, M.; Kumar, K. S., Synthesis and characterization of metal nanoparticles-decorated PPY-CNT composite and their electrocatalytic oxidation of formic acid and formaldehyde for fuel cell applications. *Applied Catalysis B: Environmental* **2007,** *75* (1-2), 129-138.

85. Gupta, S. S.; Bandyopadhya, N. R.; Datta, J., Carbon-Supported Platinum Catalysts for Direct Alcohol Fuel Cell Anode. *Materials and Manufacturing Processes* **2006,** *21* (7), 703-709.

86. Li, W.; Liang, C.; Qiu, J.; Zhou, W.; Han, H.; Wei, Z.; Sun, G.; Xin, Q., Carbon nanotubes as support for cathode catalyst of a direct methanol fuel cell. *Carbon* **2002,** *40* (5), 791-794.

87. Joo, S. H.; Choi, S. J.; Oh, I.; Kwak, J.; Liu, Z.; Terasaki, O.; Ryoo, R., Ordered nanoporous arrays of carbon supporting high disperison of platinum nanoparticles. *Nature* **2001,** *412* (6843), 169.

88. Wang, L.-L.; Johnson, D. D., Shear Instabilities in Metallic Nanoparticles: Hydrogen-Stabilized Structure of Pt37 on Carbon. *Journal of the American Chemical Society* **2007**.

89. Morrow, B. H.; Striolo, A., Platinum nanoparticles on carbonaceous materials: the effect of support geometry on nanoparticle mobility, morphology, and melting. *Nanotechnology* **2008,** *19* (19), 195711.

90. Huang, S.-P.; Mainardi, D. S.; Balbuena, P. B., Structure and dynamics of graphite-supported bimetallic nanoclusters. *Surface Science* **2003,** *545*, 163-179.

91. Liem, S. Y.; Chan, K.-Y., Simulation study of platinum adsorption on graphite using the Sutton-Chen potential. *Surface Science* **1995,** *328*, 119-128.

92. Wu, G.-W.; Chan, K.-Y., Morphology of platinum clusters on graphite at different loadings. *Surface Science* **1996,** *365*, 38-52.

93. Gu, Z.; Balbuena, P. B., Structural characterization of Pt nanoclusters deposited on graphite: Effects of substrate and surrounding medium. *Catalysis Today* **2005,** *105*, 152-161.

94. Wu, G.-W.; Chan, K.-Y., Molecular simulation of platinum clusters on graphite. *Surface Review and Letters* **1997,** *4* (5), 855-858.

95. Wu, G.-W.; Chan, K.-Y., Molecular simulation of oxygen on supported platinum clusters. *Journal of Electroanalytical Chemistry* **1998,** *450* (2), 225-231.

96. Lee, S. H.; Han, S. S.; Kang, J. K.; Ryu, J. H.; Lee, H. M., Phase stability of Pt nanoclusters and the effect of a (0 0 0 1) graphite surface through molecular dynamics simulation. *Surface Science* **2008,** *602* (7), 1433-1439.

97. Acharya, C. K.; Sullivan, D. I.; Turner, C. H., Characterizing the interaction of Pt and PtRu clusters with boron-doped, nitrogen-doped, and activated carbon: DFT calculations and parameterization. *Journal of Physical Chemistry C* **2008,** *112* (35), 13607-13622.

98. Chi, D. H.; Cuong, N. T.; Tuan, N. A.; Kim, Y.-T.; Bao, H. T.; Mitani, T.; Ozaki, T.; Nagao, H., Electronic structures of Pt clusters adsorbed on (5,5) single wall carbon nanotube. *Chemical Physics Letters* **2006,** *432*, 213-217.

99. Daw, M. S.; Foiles, S. M.; Baskes, M. I., The embedded-atom method: a review of theory and applications. *Materials Science Reports* **1993,** *9* (7-8), 251-310.

100. Trushin, O. S.; Salo, P.; Ala-Nissila, T., Energetics and many-particle mechanisms of two-dimensional cluster diffusion on Cu(100) surfaces. *Physical Review B* **2000,** *62* (3), 1611.

101. Sebetci, A.; Güvenç, Z. B., Energetics and structures of small clusters: PtN, N=2-21. *Surface Science* **2003,** *525* (1-3), 66-84.

102. Liu, J.; Selvan, M. E.; Cui, S.; Edwards, B. J.; Keffer, D. J.; Steele, W. V., Molecular-Level Modeling of the Structure and Wetting of Electrode/Electrolyte Interfaces in Hydrogen Fuel Cells. *J. Phys. Chem. C* **2008,** *112* (6), 1985-1993.

103. Luo, J.; Njoki, P. N.; Lin, Y.; Mott, D.; Wang; Zhong, C.-J., Characterization of Carbon-Supported AuPt Nanoparticles for Electrocatalytic Methanol Oxidation Reaction. *Langmuir* **2006,** *22* (6), 2892-2898.

104. Luo, J.; Maye, M. M.; Kariuki, N. N.; Wang, L.; Njoki, P.; Lin, Y.; Schadt, M.; Naslund, H. R.; Zhong, C.-J., Electrocatalytic oxidation of methanol: carbon-supported gold-platinum nanoparticle catalysts prepared by two-phase protocol. *Catalysis Today* **2005,** *99* (3-4), 291-297.

105. Balbuena, P. B.; Wang, Y.; Lamas, E. J.; Calvo, S. R.; Agapito, L. A.; Seminario, J. M., Reactivity of Bimetalllic Nanoclusters Toward the Oxygen Reduction in Acid Medium. In *Device and Materials Modeling in PEM Fuel Cells*, Paddison, S. J.; Promislow, K. S., Eds. Springer Berlin: Heidelberg, 2009; Vol. 113, pp 509-532.

106. Zhong, C.-J.; Luo, J.; Njoki, P. N.; Mott, D.; Wanjala, B.; Loukrakpam, R.; Lim, S.; Wang, L.; Fang, B.; Xu, Z., Fuel cell technology: nano-engineered multimetallic catalysts. *Energy & Environmental Science* **2008,** *1* (4), 454-466.

107. Luo, J.; Njoki, P. N.; Lin, Y.; Wang, L.; Zhong, C. J., Activity-composition correlation of AuPt alloy nanoparticle catalysts in electrocatalytic reduction of oxygen. *Electrochemistry Communications* **2006,** *8* (4), 581-587.

108. Shu, Y.; Murillo, L. E.; Bosco, J. P.; Huang, W.; Frenkel, A. I.; Chen, J. G., The effect of impregnation sequence on the hydrogenation activity and selectivity of supported Pt/Ni bimetallic catalysts. *Applied Catalysis A: General* **2008,** *339* (2), 169-179.

109. Merlo, A. B.; Vetere, V.; Ruggera, J. F.; Casella, M. L., Bimetallic PtSn catalyst for the selective hydrogenation of furfural to furfuryl alcohol in liquid-phase. *Catalysis Communications* **2009,** *10* (13), 1665-1669.

110. Plomp, A. J.; van Asten, D. M. P.; van der Eerden, A. M. J.; Mäki-Arvela, P.; Murzin, D. Y.; de Jong, K. P.; Bitter, J. H., Catalysts based on platinum-tin and platinum-gallium in close contact for the selective hydrogenation of cinnamaldehyde. *Journal of Catalysis* **2009,** *263* (1), 146-154.

111. Bertero, N. M.; Trasarti, A. F.; Moraweck, B.; Borgna, A.; Marchi, A. J., Selective liquid-phase hydrogenation of citral over supported bimetallic Pt-Co catalysts. *Applied Catalysis A: General* **2009,** *358* (1), 32-41.

112. Thomas, J. M.; Adams, R. D.; Boswell, E. M.; Captain, B.; Gronbeck, H.; Raja, R., Synthesis, characterization, electronic structure and catalytic performance of bimetallic and trimetallic nanoparticles containing tin. *Faraday Discussions* **2008,** *138*, 301-315.

113. Nutt, M. O.; Hughes, J. B.; Wong, M. S., Designing Pd-on-Au Bimetallic Nanoparticle Catalysts for Trichloroethene Hydrodechlorination. *Environmental Science & Technology* **2005,** *39* (5), 1346-1353.

114. He, F.; Zhao, D.; Liu, J.; Roberts, C. B., Stabilization of Fe-Pd Nanoparticles with Sodium Carboxymethyl Cellulose for Enhanced Transport and Dechlorination of Trichloroethylene in Soil and Groundwater. *Industrial & Engineering Chemistry Research* **2006,** *46* (1), 29-34.

115. Fernandez, J. L.; Walsh, D. A.; Bard, A. J., Thermodynamic Guidelines for the Design of Bimetallic Catalysts for Oxygen Electroreduction and Rapid Screening by Scanning Electrochemical Microscopy. M-Co (M: Pd, Ag, Au). *Journal of the American Chemical Society* **2005,** *127* (1), 357-365.

116. Zhao, Y.; E, Y.; Fan, L.; Qiu, Y.; Yang, S., A new route for the electrodeposition of platinum-nickel alloy nanoparticles on multi-walled carbon nanotubes. *Electrochimica Acta* **2007,** *52* (19), 5873-5878.

117. Yoon, B.; Pan, H.-B.; Wai, C. M., Relative Catalytic Activities of Carbon Nanotube-Supported Metallic Nanoparticles for Room-Temperature Hydrogenation of Benzene. *The Journal of Physical Chemistry C* **2009,** *113* (4), 1520-1525.

118. Ryu, J. H.; Seo, D. H.; Kim, D. H.; Lee, H. M., Molecular dynamics simulations of the diffusion and rotation of Pt nanoclusters supported on graphite. *Physical Chemistry Chemical Physics* **2009,** *11* (3), 503-507.

119. Seo, D. H.; Kim, H. Y.; Ryu, J. H.; Lee, H. M., Molecular Dynamics Simulation of the Diffusion of Au and Pt Nanoclusters on Carbon Nanotubes. *The Journal of Physical Chemistry C* **2009,** *113* (24), 10416-10421.

120. Kim, D. H.; Kim, H. Y.; Ryu, J. H.; Lee, H. M., Phase diagram of Ag-Pd bimetallic nanoclusters by molecular dynamics simulations: solid-to-liquid transition and size-dependent behavior. *Physical Chemistry Chemical Physics* **2009,** *11* (25), 5079-5085.

121. Mejia-Rosales, S. J.; Fernandez-Navarro, C.; Perez-Tijerina, E.; Montejano-Carrizales, J. M.; Jose-Yacaman, M., Two-Stage Melting of Au-Pd Nanoparticles. *The Journal of Physical Chemistry B* **2006,** *110* (26), 12884-12889.

122. Liu, H. B.; Pal, U.; Perez, R.; Ascencio, J. A., Structural Transformation of Au-Pd Bimetallic Nanoclusters on Thermal Heating and Cooling: A Dynamic Analysis. *The Journal of Physical Chemistry B* **2006,** *110* (11), 5191-5195.

123. Li, G.; Wang, Q.; Li, D.; Lü, X.; He, J., Size and composition effects on the melting of bimetallic Cu-Ni clusters studied via molecular dynamics simulation. *Materials Chemistry and Physics* **2009,** *114* (2-3), 746-750.

124. Sankaranarayanan, S. K. R. S.; Bhethanabotla, V. R.; Joseph, B., Molecular dynamics simulation study of the melting of Pd-Pt nanoclusters. *Physical Review B* **2005,** *71*, 195415.

125. Liu, H. B.; Pal, U.; Ascencio, J. A., Thermodynamic Stability and Melting Mechanism of Bimetallic Au-Pt Nanoparticles. *The Journal of Physical Chemistry C* **2008,** *112* (49), 19173-19177.

126. Yang, Z.; Yang, X.; Xu, Z., Molecular Dynamics Simulation of the Melting Behavior of Pt-Au Nanoparticles with Core-Shell Structure. *The Journal of Physical Chemistry C* **2008,** *112* (13), 4937-4947.

127. Oviedo, O. A.; Leiva, E. P. M.; Mariscal, M. M., Thermodynamic considerations and computer simulations on the formation of core-shell nanoparticles under electrochemical conditions. *Physical Chemistry Chemical Physics* **2008,** *10* (24), 3561-3568.

128. Xiao, S.; Hu, W.; Luo, W.; Wu, Y.; Li, X.; Deng, H., Size effect on alloying ability and phase stability of immiscible bimetallic nanoparticles. *European Physical Journal B -- Condensed Matter* **2006,** *54* (4), 479-484.

129. Mejia-Rosales, S. J.; Fernandez-Navarro, C.; Perez-Tijerina, E.; Blom, D. A.; Allard, L. F.; Jose-Yacaman, M., On the Structure of Au/Pd Bimetallic Nanoparticles. *The Journal of Physical Chemistry C* **2007,** *111* (3), 1256-1260.

130. Chen, F.; Johnston, R. L., Martensitic transformations in Ag-Au bimetallic core-shell nanoalloys. *Applied Physics Letters* **2008,** *92* (2), 023112.

131. Chui, Y. H.; Chan, K.-Y., Structures and Energetics of Platinum-Cobalt Bimetallic Clusteres. *Molecular Simulation* **2004,** *30* (10), 679-690.

132. Chui, Y. H.; Chan, K.-Y., Distribution of platinum and cobalt atoms in a bimetallic nanoparticle. *Chemical Physics Letters* **2005,** *408* (1-3), 49-53.

133. Kim, D. H.; Kim, H. Y.; Kim, H. G.; Ryu, J. H.; Lee, H. M., The solid-to-liquid transition region of an Ag-Pd bimetallic nanocluster. *Journal of Physics: Condensed Matter* **2008,** *20* (3), 035208.

134. Mariscal, M. M.; Dassie, S. A.; Leiva, E. P. M., Collision as a way of forming bimetallic nanoclusters of various structures and chemical compositions. *Journal of Chemical Physics* **2005,** *123*, 184505.

135. Liu, H. B.; Pal, U.; Medina, A.; Maldonado, C.; Ascencio, J. A., Structural incoherency and structure reversal in bimetallic Au-Pd nanoclusters. *Physical Review B* **2005,** *71* (7), 075403-6.

136. Calvo, S. R.; Balbuena, P. B., Molecular dynamics studies of phonon spectra in mono- and bimetallic nanoclusters. *Surface Science* **2005,** *581* (2-3), 213-224.

137. Dimitratos, N.; Messi, C.; Porta, F.; Prati, L.; Villa, A., Investigation on the behaviour of Pt(0)/carbon and Pt(0),Au(0)/carbon catalysts employed in the oxidation of glycerol with molecular oxygen in water. *Journal of Molecular Catalysis A: Chemical* **2006,** *256* (1-2), 21-28.

138. Comotti, M.; Pina, C. D.; Rossi, M., Mono- and bimetallic catalysts for glucose oxidation. *Journal of Molecular Catalysis A: Chemical* **2006,** *251* (1-2), 89-92.

139. *CRC Handbook of Chemistry and Physics*, 84th ed.; CRC Press: Boca Raton, 2003.

140. Tersoff, J.; Ruoff, R. S., Structural Properties of a Carbon-Nanotube Crystal. *Physical Review Letters* **1994,** *73* (5), 676-679.

141. Zang, J.; Aldas-Palacios, O.; Liu, F., MD Simulation of Structural and Mechanical Transformation of Single-Walled Carbon Nanotubes Under Pressure. *Communications in Computational Physics* **2007,** *2* (3), 451-465.

142. Imtani, A. N.; Jindal, V. K., Structure of armchair single-wall carbon nanotubes under hydrostatic pressure. *Physical Review B* **2007,** *76* (19), 195447-9.

143. Hsieh, J.-Y.; Lu, J.-M.; Huang, M.-Y.; Hwang, C.-C., Theoretical variations in the Young's modulus of single-walled carbon nanotubes with tube radius and temperature: a molecular dynamics study. *Nanotechnology* **2006,** *17* (15), 3920.

144. Raravikar, N. R.; Keblinski, P.; Rao, A. M.; Dresselhaus, M. S.; Schadler, L. S.; Ajayan, P. M., Temperature dependence of radial breathing mode Raman frequency of single-walled carbon nanotubes. *Physical Review B* **2002,** *66* (23), 235424.

145. Bhethanabotla, V. R.; Steele, W. A., Computer-simulation study of melting in dense oxygen layers on graphite. *Physical Review B* **1990,** *41* (13), 9480.

146. Agrawal, P. M.; Rice, B. M.; Thompson, D. L., Predicting trends in rate parameters for self-diffusion on FCC metal surfaces. *Surface Science* **2002,** *515* (1), 21-35.

147. Acharya, C. K.; Sullivan, D. I.; Turner, C. H., Characterizing the Interaction of Pt and PtRu Clusters with Boron-Doped, Nitrogen-Doped, and Activated Carbon: Density Functional Theory Calculations and Parameterization. *The Journal of Physical Chemistry C* **2008,** *112* (35), 13607-13622.

148. Morrow, B. H.; Striolo, A., Assessing how metal-carbon interactions affect the structure of supported platinum nanoparticles. *Molecular Simulation* **2009,** *35* (10/11), 795-803.

149. Yang, Z.; Yang, X.; Xu, Z.; Liu, S., Structural evolution of Pt-Au nanoalloys during heating process: comparison of random and core-shell orderings. *Physical Chemistry Chemical Physics* **2009,** *11* (29), 6249-6255.

150. Reyes-Nava, J. A.; Rodriguez-Lopez, J. L.; Pal, U., Generalizing segregation and chemical ordering in bimetallic nanoclusters through atomistic view points. *Physical Review B* **2009,** *80* (16), 161412.

151. Henglein, A., Preparation and Optical Aborption Spectra of AucorePtshell and PtcoreAushell Colloidal Nanoparticles in Aqueous Solution. *The Journal of Physical Chemistry B* **2000,** *104* (10), 2201-2203.

152. Hodak, J. H.; Henglein, A.; Hartland, G. V., Tuning the spectral and temporal response in PtAu core-shell nanoparticles. *Journal of Chemical Physics* **2001,** *114* (6), 2760-2765.

153. Garcia-Gutierrez, D. I.; Gutierrez-Wing, C. E.; Giovanetti, L.; Ramallo-Lopez, J. M.; Requejo, F. G.; Jose-Yacaman, M., Temperature Effect on the Synthesis of Au−Pt Bimetallic Nanoparticles. *The Journal of Physical Chemistry B* **2005,** *109* (9), 3813-3821.

154. Yang, J.; Yang Lee, J.; Too, H.-P., Phase-Transfer Identification of Core-Shell Structures in Bimetallic Nanoparticles. *Plasmonics* **2006,** *1* (1), 67-78.

155. Wang, S.; Kristian, N.; Jiang, S.; Wang, X., Controlled synthesis of dendritic Au@Pt core-shell nanomaterials for use as an effective fuel cell electrocatalyst. *Nanotechnology* **2009,** *20* (2), 025605.

156. Zhang, W.; Li, L.; Du, Y.; Wang, X.; Yang, P., Gold/Platinum Bimetallic Core/Shell Nanoparticles Stabilized by a Fréchet-Type Dendrimer: Preparation and Catalytic Hydrogenations of Phenylaldehydes and Nitrobenzenes. *Catalysis Letters* **2009,** *127* (3), 429-436.

157. Selvarani, G.; Selvaganesh, S. V.; Krishnamurthy, S.; Kiruthika, G. V. M.; Sridhar, P.; Pitchumani, S.; Shukla, A. K., A Methanol-Tolerant Carbon-Supported Pt-Au Alloy Cathode Catalyst for Direct Methanol Fuel Cells and Its Evaluation by DFT. *The Journal of Physical Chemistry C* **2009,** *113* (17), 7461-7468.

158. Petkov, V.; Shastri, S. D., Element-specific structure of materials with intrinsic disorder by high-energy resonant x-ray diffraction and differential atomic pair-distribution functions: A study of PtPd nanosized catalysts. *Physical Review B* **2010,** *81* (16), 165428.

159. Morrow, B. H.; Striolo, A., Supported bimetallic Pt-Au nanoparticles: Structural features predicted by molecular dynamics simulations. *Physical Review B* **2010,** *81* (15), 155437.

160. Pestryakov, A. N.; Bogdanchikova, N.; Simakov, A.; Tuzovskaya, I.; Jentoft, F.; Farias, M.; Díaz, A., Catalytically active gold clusters and nanoparticles for CO oxidation. *Surface Science* **2007,** *601* (18), 3792-3795.

161. Bell, A. T., The Impact of Nanoscience on Heterogeneous Catalysis. *Science* **2003,** *299* (5613), 1688-1691.

162. Carrette, L.; Friedrich, K. A.; Stimming, U., Fuel Cells: Principles, Types, Fuels, and Applications. *ChemPhysChem* **2000,** *1* (4), 162-193.

163. Khodakov, A. Y.; Chu, W.; Fongarland, P., Advances in the Development of Novel Cobalt Fischer−Tropsch Catalysts for Synthesis of Long-Chain Hydrocarbons and Clean Fuels. *Chemical Reviews* **2007,** *107* (5), 1692-1744.

164. Alayoglu, S.; Nilekar, A. U.; Mavrikakis, M.; Eichhorn, B., Ru-Pt core-shell nanoparticles for preferential oxidation of carbon monoxide in hydrogen. *Nature Materials* **2008,** *7* (4), 333-338.

165. Nilekar, A. U.; Alayoglu, S.; Eichhorn, B.; Mavrikakis, M., Preferential CO Oxidation in Hydrogen: Reactivity of Core−Shell Nanoparticles. *Journal of the American Chemical Society* **2010,** *132* (21), 7418-7428.

166. Yudanov, I. V.; Sahnoun, R.; Neyman, K. M.; Rosch, N.; Hoffmann, J.; Schauermann, S.; Johanek, V.; Unterhalt, H.; Rupprechter, G.; Libuda, J.; Freund, H.-J., CO Adsorption on Pd Nanoparticles: Density Functional and Vibrational Spectroscopy Studies. *The Journal of Physical Chemistry B* **2003,** *107* (1), 255-264.

167. Song, C.; Ge, Q.; Wang, L., DFT Studies of Pt/Au Bimetallic Clusters and Their Interactions with the CO Molecule. *J. Phys. Chem. B* **2005,** *109* (47), 22341-22350.

168. Pedersen, M. Ø.; Helveg, S.; Ruban, A.; Stensgaard, I.; Lægsgaard, E.; Nørskov, J. K.; Besenbacher, F., How a gold substrate can increase the reactivity of a Pt overlayer. *Surface Science* **1999,** *426* (3), 395-409.

169. Habrioux, A.; Vogel, W.; Guinel, M.; Guetaz, L.; Servat, K.; Kokoh, B.; Alonso-Vante, N., Structural and electrochemical studies of Au-Pt nanoalloys. *Physical Chemistry Chemical Physics* **2009,** *11* (18), 3573-3579.

170. Irissou, E.; Laplante, F.; Garbarino, S.; Chaker, M.; Guay, D., Structural and Electrochemical Characterization of Metastable PtAu Bulk and Surface Alloys Prepared by Crossed-Beam Pulsed Laser Deposition. *The Journal of Physical Chemistry C* **2010,** *114* (5), 2192-2199.

171. Vajda, S.; Pellin, M. J.; Greeley, J. P.; Marshall, C. L.; Curtiss, L. A.; Ballentine, G. A.; Elam, J. W.; Catillon-Mucherie, S.; Redfern, P. C.; Mehmood, F.; Zapol, P., Subnanometre platinum clusters as highly active and selective catalysts for the oxidative dehydrogenation of propane. *Nature Materials* **2009,** *8* (3), 213-216.

172. Frisch, M. J.; Trucks, G. W.; Schlegel, H. B.; Scuseria, G. E.; Robb, M. A.; Cheeseman, J. R.; J. A. Montgomery, J.; Vreven, T.; Kudin, K. N.; Burant, J. C.; Millam, J. M.; Iyengar, S. S.; Tomasi, J.; Barone, V.; Mennucci, B.; Cossi, M.; Scalmani, G.; Rega, N.; Petersson, G. A.; Nakatsuji, H.; Hada, M.; Ehara, M.; Toyota, K.; Fukuda, R.; Hasegawa, J.; Ishida, M.; Nakajima, T.; Honda, Y.; Kitao, O.; Nakai, H.; Klene, M.; Li, X.; Knox, J. E.; Hratchian, H. P.; Cross, J. B.; Bakken, V.; Adamo, C.; Jaramillo, J.; Gomperts, R.; Stratmann, R. E.; Yazyev, O.; Austin, A. J.; Cammi, R.; Pomelli, C.; Ochterski, J. W.; Ayala, P. Y.; Morokuma, K.; Voth, G. A.; Salvador, P.; Dannenberg, J. J.; Zakrzewski, V. G.; Dapprich, S.; Daniels, A. D.; Strain, M. C.; Farkas, O.; Malick, D. K.; Rabuck, A. D.; Raghavachari, K.; Foresman, J. B.; Ortiz, J. V.; Cui, Q.; Baboul, A. G.; Clifford, S.; Cioslowski, J.; Stefanov, B. B.; Liu, G.; Liashenko, A.; Piskorz, P.; Komaromi, I.; Martin, R. L.; Fox, D. J.; Keith, T.; Al-Laham, M. A.; Peng, C. Y.; Nanayakkara, A.; Challacombe, M.; Gill, P. M. W.; Johnson, B.; Chen, W.; Wong, M. W.; Gonzalez, C.; Pople, J. A. *Gaussian 03, Revision E.01*, Wallingford, CT, 2004.

173. Becke, A. D., Density-functional thermochemistry. III. The role of exact exchange. *The Journal of Chemical Physics* **1993,** *98* (7), 5648-5652.

174. Lee, C.; Yang, W.; Parr, R. G., Development of the Colle-Salvetti correlation-energy formula into a functional of the electron density. *Physical Review B* **1988,** *37*, 785.

175. Vosko, S. H.; Wilk, L.; Nusair, M., Accurate spin-dependent electron liquid correlation energies for local spin density calculations: a critical analysis. *Canadian Journal of Physics* **1980,** *58* (8), 1200-1211.

176. Stephens, P. J.; Devlin, F. J.; Chabalowski, C. F.; Frisch, M. J., Ab Initio Calculation of Vibrational Absorption and Circular Dichroism Spectra Using Density Functional Force Fields. *The Journal of Physical Chemistry* **1994,** *98* (45), 11623-11627.

177. Perdew, J. P., Density-functional approximation for the correlation energy of the inhomogeneous electron gas. *Physical Review B* **1986,** *33* (12), 8822.

178. Becke, A. D., Density-functional exchange-energy approximation with correct asymptotic behavior. *Physical Review A* **1988,** *38* (6), 3098.

179. Perdew, J. P., Electronic Structure of Solids '91. In *Electronic Structure of Solids '91*, Ziesche, P.; Eschrig, H., Eds. Akademie Verlag: Berlin, 1991; p 11.

180. Perdew, J. P.; Chevary, J. A.; Vosko, S. H.; Jackson, K. A.; Pederson, M. R.; Singh, D. J.; Fiolhais, C., Atoms, molecules, solids, and surfaces: Applications of the generalized gradient approximation for exchange and correlation. *Physical Review B* **1992,** *46* (11), 6671.

181. Perdew, J. P.; Burke, K.; Ernzerhof, M., Generalized Gradient Approximation Made Simple. *Physical Review Letters* **1996,** *77* (18), 3865.

182. Adamo, C.; Barone, V., Toward reliable density functional methods without adjustable parameters: The PBE0 model. *The Journal of Chemical Physics* **1999,** *110* (13), 6158-6170.

183. Giuffrida, S.; Barone, G.; Duca, D., Adsorbed CO on Group 10 Metal Fragments: A DFT Study. *Journal of Chemical Information and Modeling* **2009,** *49* (5), 1223-1233.

184. de Souza Monteiro, R.; Paes, L.; de M. Carneiro, J.; Aranda, D., Modeling the Adsorption of CO on Small Pt, Fe and Co Clusters for the Fischer–Tropsch Synthesis. *Journal of Cluster Science* **2008,** *19* (4), 601-614.

185. Zeinalipour-Yazdi, C. D.; Cooksy, A. L.; Efstathiou, A. M., CO adsorption on transition metal clusters: Trends from density functional theory. *Surface Science* **2008,** *602* (10), 1858-1862.

186. Shimodaira, Y.; Tanaka, T.; Miura, T.; Kudo, A.; Kobayashi, H., Density Functional Theory Study of Anode Reactions on Pt-Based Alloy Electrodes. *J. Phys. Chem. C* **2007,** *111* (1), 272-279.

187. Hay, P. J.; Wadt, W. R., Ab initio effective core potentials for molecular calculations. Potentials for K to Au including the outermost core orbitals. *The Journal of Chemical Physics* **1985,** *82* (1), 299-310.

188. *CRC Handbook of Chemistry and Physics*, 81st ed.; CRC Press: Boca Raton, 2000.

189. O'Boyle, N. M.; Tenderholt, A. L.; Langner, K. M., cclib: A library for package-independent computational chemistry algorithms. *Journal of Computational Chemistry* **2008,** *29* (5), 839-845.

190. Carpenter, J. E.; Weinhold, F., Analysis of the geometry of the hydroxymethyl radical by the "different hybrids for different spins" natural bond orbital procedure. *Journal of Molecular Structure: THEOCHEM* **1988,** *169*, 41-62.

191. Foster, J. P.; Weinhold, F., Natural hybrid orbitals. *Journal of the American Chemical Society* **1980,** *102* (24), 7211-7218.

192. Bourane, A.; Dulaurent, O.; Bianchi, D., Heats of Adsorption of Linear and Multibound Adsorbed CO Species on a Pt/Al2O3 Catalyst Using in Situ Infrared Spectroscopy under Adsorption Equilibrium. *Journal of Catalysis* **2000,** *196* (1), 115-125.

193. Meier, D. C.; Goodman, D. W., The Influence of Metal Cluster Size on Adsorption Energies: CO Adsorbed on Au Clusters Supported on TiO2. *Journal of the American Chemical Society* **2004,** *126* (6), 1892-1899.

194. Chen, L.; Chen, B.; Zhou, C.; Wu, J.; Forrey, R. C.; Cheng, H., Influence of CO Poisoning on Hydrogen Chemisorption onto a Pt6 Cluster. *J. Phys. Chem. C* **2008,** *112*, 13937-13942.

195. Gruene, P.; Fielicke, A.; Meijer, G.; Rayner, D. M., The adsorption of CO on group 10 (Ni, Pd, Pt) transition-metal clusters. *Physical Chemistry Chemical Physics* **2008,** *10* (40), 6144-6149.

196. Blyholder, G., Molecular Orbital View of Chemisorbed Carbon Monoxide. *The Journal of Physical Chemistry* **1964,** *68* (10), 2772-2777.

197. Babarao, R.; Jiang, J.; Sandler, S. I., Molecular Simulations for Adsorptive Separation of CO2/CH4 Mixture in Metal-Exposed, Catenated, and Charged Metal−Organic Frameworks. *Langmuir* **2008,** *25* (9), 5239-5247.

198. Mulliken, R. S., Electronic Population Analysis on LCAO[Single Bond]MO Molecular Wave Functions. I. *The Journal of Chemical Physics* **1955,** *23* (10), 1833-1840.

199. Besler, B. H.; Jr., K. M. M.; Kollman, P. A., Atomic charges derived from semiempirical methods. *Journal of Computational Chemistry* **1990,** *11* (4), 431-439.

200. Reed, A. E.; Curtiss, L. A.; Weinhold, F., Intermolecular interactions from a natural bond orbital, donor-acceptor viewpoint. *Chemical Reviews* **1988,** *88* (6), 899-926.

201. Zhou, Z.; Parr, R. G., Activation hardness: new index for describing the orientation of electrophilic aromatic substitution. *Journal of the American Chemical Society* **1990,** *112* (15), 5720-5724.

202. Aihara, J.-i., Correlation found between the HOMO-LUMO energy separation and the chemical reactivity at the most reactive site for isolated-pentagon isomers of fullerenes. *Physical Chemistry Chemical Physics* **2000,** *2* (14), 3121-3125.

203. Ruban, A.; Hammer, B.; Stoltze, P.; Skriver, H. L.; Nørskov, J. K., Surface electronic structure and reactivity of transition and noble metals. *Journal of Molecular Catalysis A: Chemical* **1997,** *115* (3), 421-429.

204. Kitchin, J. R.; Norskov, J. K.; Barteau, M. A.; Chen, J. G., Modification of the surface electronic and chemical properties of Pt(111) by subsurface 3d transition metals. *The Journal of Chemical Physics* **2004,** *120* (21), 10240-10246.

205. Mavrikakis, M.; Hammer, B.; Norskov, J. K., Effect of Strain on the Reactivity of Metal Surfaces. *Physical Review Letters* **1998,** *81* (13), 2819.

206. Hammer, B.; Nielsen, O. H.; Norskov, J. K., Structure sensitivity in adsorption: CO interaction with stepped and reconstructed Pt surfaces. *Catalysis Letters* **1997,** *46* (1), 31-35.

207. Hammer, B.; Norskov, J. K., Adsorbate Reorganization at Steps: NO on Pd(211). *Physical Review Letters* **1997,** *79* (22), 4441.